2016

Nanoengineered Energy Harvesting and Storage Devices

Chao Li
University of Central Florida

NANOENGINEERED ENERGY HARVESTING AND STORAGE DEVICES

by

CHAO LI
M.S. New Jersey Institute of Technology, 2010

A dissertation submitted in partial fulfillment of requirements
for the degree of Doctor of Philosophy
in the Department of Materials Science and Engineering
in the College of Engineering & Computer Science
at the University of Central Florida
Orlando, Florida

Summer Term
2016

Major Professor: Jayan Thomas

ABSTRACT

Organic and perovskite solar cells have recently attracted significant attention due to its flexibility, ease of fabrication and excellent performance. In order to realize even better performance for organic and perovskite solar cells, rejuvenated effort towards developing nanostructured electrodes and high quality active layer is necessary.

In this dissertation, several strategic directions of enhancing the performance of organic and perovskite solar cells are investigated. An introduction and background of organic and perovskite solar cells, which includes motivation, classification and working principles, nanostructured electrode materials and solvent effect on active materials, and devices fabrication, are presented. A facile method, called Spin-on Nanoprinting (SNAP), to fabricate highly ordered ZnO-AgNW-ZnO electrode is introduced to enhance the performance of organic solar cell. Subsequently, a ternary solvent method is developed to fabricate high Voc thieno[3,4-*b*]thiophene/benzodithiophene (PTB7) and indene-C_{60} bisadduct (ICBA)solar cells. The performance of the devices improved about 20% compared to those made by binary solvent method. In order to understand the fundamental properties of the materials ruling the performance of the PSCs tested, AFM-based nanoscale characterization techniques including Pulsed-Force-Mode AFM (PFM-AFM) and Mode-Synthesizing AFM (MSAFM) are introduced. These methods are used to study the morphology and physical properties of the structures constitutive of the active layers of the PSCs. Conductive-AFM (cAFM) studies reveal local variations in conductivity in the donor and acceptor phases as well as an increase in photocurrent measured in the PTB7:ICBA sample obtained with the ternary solvent processing technique. Moreover, efficient perovskite solar cells with good transparency in the visible wavelength range have been developed by a facile and low-temperature PCBM-assisted perovskite growth method.

This method results in the formation of perovskite-PCBM hybrid material at the grain boundaries which is observed by EELS mapping and confirmed by steady-state photoluminescence (PL) spectra and transient photocurrent (TP) measurements. This method involves fewer steps and therefore is less expensive and time consuming than other reported methods. In addition, we report an all solid state, energy harvesting and storing (ENHANS) filament which integrates perovskite solar cell (PSC) on top of a symmetric supercapacitor (SSC) via a copper filament which works as a shared electrode for direct charge transfer. Developing ENHANS on a copper filament provides a low-cost solution for flexible self-sufficient energy systems for wearables and other portable devices. Finally, a summary of this dissertation as well as some potential future directions are presented.

To my wife and parents

ACKNOWLEDGMENT

It is with immense gratitude that I acknowledge the support and help of my family, friends and committee members who contributed to the completion of this degree.

I wish to thank, first and foremost, my advisor, Dr. Jayan Thomas, for being a tremendous mentor throughout my graduate study. He has the attitude and the essence of a great scientist: he constantly and convincingly instilled a spirit of adventure with respect to research and scholarship. His support, wisdom and commitment to the highest standards motivated me all the time. He acts as a role model of being a good scientist whom I can learn from.

I am also grateful to the committee members. Dr. Lei Zhai, Dr. Andre J. Gesquiere, Dr. Yajie Dong, Dr. Wei Sun and Dr. Yang Yang, thanks for the encouragement, time, and attention provided. I also thank Dr. Laurene Tetard, Dr. Linan An and Dr. Ming Su for their kind suggestions in both research and life.

I would like to thank my wife whose love and support kept me strong for all the days we spent to pursue this degree. I am most fortunate to have such a great friend and partner, who never failed to boost my ego during the hardest and frustrating times of my study. I could not have done this without her.

I am truly indebted to my parents whose love, patience and faith inspired me to begin this journey. Their prayers and teachings have been immeasurably valuable.

I thank my colleagues who share their enthusiasm and comments on my work: Dr. Binh Duong, Dr. Reji Philip, Dr. Zenan Yu, Dr. Panit Chantharasupawong, Nitesh Dhasmana, Julian Moore, Joe Sleppy, Yi Ding, Mikhael Soliman, Katherine Layne, Brandon Carpenter, Caleb Morrison, Josie Lorenzo, Yanan Wang, Dr. Chaoming Wang and Dr. Guangming Tao.

I like to thank my friends, especially Dr. Wenlang Liang, Mingjie Liu, Yu Bi, Yunshu

Wang, Chi Chen, Hank Wang, Jinyin Jiang, Jiawei Wu and Jiang Wen for their friendship, encouragement, and advices.

TABLE OF CONTENTS

LIST OF FIGURES

LIST OF TABLES

1 INTRODUCTION

1.1 Development and motivation of Solar Energy

Currently, fossil fuel and other nonrenewable sources are used to supply the energy for our daily life from automobile to airplane. However, the price of some nonrenewable sources increases and their source is limited in our earth. Moreover fossil fuels when burn release carbon dioxide into the atmosphere where it adds to the greenhouse gases causing global warming, which is harmful to our living environment. In order to avoid the high expense for fossil oil and environmental pollution, renewable energy is necessary to be widely used. Therefore, one of the promising devices for harvesting renewable energy, solar cell, developed with new design strategies is introduced in this report. Solar cell is the device that converts the solar radiation to electricity. Green leaf of a green plant does similar things: they convert sunlight to chemical energy. The sun supplies us a clean and unlimited source of energy, helping us relieve the energy crises and world pollution. The source is plenty while the approach to efficiently tap it remains a challenge. After the first modern Si p-n junction solar cell was invented at bell lab in 1954,[1] many attempts have been done looking for a high-efficiency low-cost solar cells, like GaAs solar cell, Cu2S/CdS solar cell and dye-sensitized solar cell.[2,3,4] In order to increase the power conversion efficiency of the solar cell, much has been done for increasing sunlight concentration, carrier collection and cell stability besides materials research.[5]

Due to the high cost and complex fabrication for these inorganic solar cells, researches have gone beyond the inorganic world. Despite their low efficiency, the organic polymers and organic-inorganic hybrid perovskite have attracted much interest. Organic materials have

attracted a high degree of attention, as they offer large area production in high-volume by printing or other low-cost manufacturing techniques. Organic photovoltaic (OPV) devices in this mode are perhaps the most studied device in addition to the organic thin film transistors (OFET) and organic light emitting diodes (OLED). The poly(3-hexylthiophene) (P3HT) and [6, 6]-phenyl C61-butyric acid methylester (PCBM) blends is one of the promising organic solar cell materials. So far, it is the most widely used fullerene derivate based donor-acceptor copolymer.[6,7] P3HT is in the Polythiophene family, which is a conducting polymer. It is the excitation of the π-orbital electron in P3HT that gives the photovoltaic effect in the blend.[8] PCBM is a fullerene derivative. Due to its high electron mobility, it plays the role of electron acceptor in many organic cells. Since organic polymers have wider bandgap than inorganic semiconductors, they give an efficient absorption at near UV range. So is P3HT:PCBM blends; the bandgap of this blend is approximately 1.8eV. So the longest absorption wavelength should be around 650 nm.[9]

Perovskite materials such as methylammonium lead halides are cheap to produce and simple to manufacture. Cell efficiencies of devices using these materials have increased from 3.8% in 2009 to 21.0% in 2015,[10] making this the fastest-advancing solar technology to date.[1] With the potential of achieving even higher efficiencies and very low production costs, perovskite solar cells have become commercially attractive, with start-up companies already promising modules on the market by 2017.[11]

1.2 Chapter Outline

Chapter 2 starts with background discussion which includes introduction of organic solar cells and perovskite solar cells, working principles, and classification. This section gives a comprehensive review of organic solar cells and perovskite solar cells.

After the background information, a nanostructured transparent electrode (ZnO-AgNW-ZnO) is presented in Chapter 3. This chapter includes an approach to easily obtain highly ordered ZnO nanorods and their performance as organic solar cell electrodes.

In Chapter 4, solvent effect for active materials is presented. Ternary solvent has been introduced for obtaining high Voc and performance devices in this chapter. In addition, two new AFM-based nanoscale characterization techniques to study the surface morphology and physical properties of the structured active layer are introduced.

Chapter 5 presents semitransparent perovskite solar cell with PCBM assisted method. In this Chapter, a facile and low-temperature PCBM-assisted perovskite growth method is introduced. This method results in the formation of perovskite-PCBM hybrid material at the grain boundaries. This method involves fewer steps and therefore is less expensive and time consuming than other reported methods.

Chapter 6 details the development of a filament which integrates a solar cell and a supercapacitor into a single ribbon capable of harvesting and storing energy in itself. When the flexible solar filament (with a conversion efficiency10.5%) of the integrated device is illuminated with simulated solar light, the supercapacitor held an energy density of 1.15 mWh cm^{-3} (at 4 mA cm^{-2}) and a power density of 243.46 mW cm^{-3} (at 8 mA cm^{-2}) generated by the solar cell. Moreover, these filaments were successfully woven into a fabric form. Our all-solid filament unveils a highly flexible and portable self-sufficient energy system with potential applications in wearables, drones and electric vehicles.

Chapter 7 concludes this dissertation and possible future directions.

1.3 References

1. Chapin, D.M.; Fuller, C.S.; Pearson,G. L., *J. Appl. Phys.*, 1954, **25**, 676.

2. Keisuke Nakayama, Katsuaki Tanabe and Harry A. Atwater, *Appl. Phys. Lett.,* 2008, **93**, 121904.

3. L. L. Kazmerski, F. R. White and G. K. Morgan, *Appl. Phys. Lett.*, 1976, **29**, 268.

4. Wang, Peng, Shaik M. Zakeeruddin, Jacques E. Moser, Mohammad K. Nazeeruddin, Takashi Sekiguchi, and Michael Grätzel, *Nature materials*, 2003, **2**, 402-407.

5. Frederik C. Krebs and Holger Spanggaard, *Chem. Mater.*, 2005, **17**, 5235–5237.

6. E. Perzon, X. Wang, F. Zhang, W. Mammo, J.L. Delgado, P. Cruz, O. Inganäs, F. Langa, M.R. Andersson, *Synthetic Metals*, 2005, **154**, 53-56.

7. Al-lbrahim, M.; Ambacher, O., *Appl. Phys. Lett.*, 2005, 86201120.

8. Nalwa, H.S., ISBN: 0-471-96595-2

9. Cook, S.; Katoh, R.; Furube, A., *J. Phys. Chem. C.*, 2009, **113**, 2547-2552.

10. Kojima, Akihiro; Teshima, Kenjiro; Shirai, Yasuo; Miyasaka, Tsutomu., *J. Am. Chem. Soc.*, **131**, 6050–6051.

11. Wang, Ucilia, *The Wall Street Journal*, 2015.

2 BACKGROUND

2.1 Introduction of Organic Solar Cells

2.1.1 Working principles

To better understand the limits on the efficiency of BHJ organic solar cell and figure out paths to improve them, it is necessary to consider all the processes required to convert photon energy into electrical energy. For organic solar cell, the photovoltaic process of converting light to electricity is determined by four important components.[1]

$$\eta_{\text{eff}} = \eta_{\text{abs}} * \eta_{\text{diss}} * \eta_{\text{tans}} * \eta_{\text{col}}$$

η_{abs} : light absorption efficiency

$\eta_{\text{diss.}}$: exciton dissociation efficiency

η_{tans} : charge transport efficiency

η_{col} : charge collection efficiency

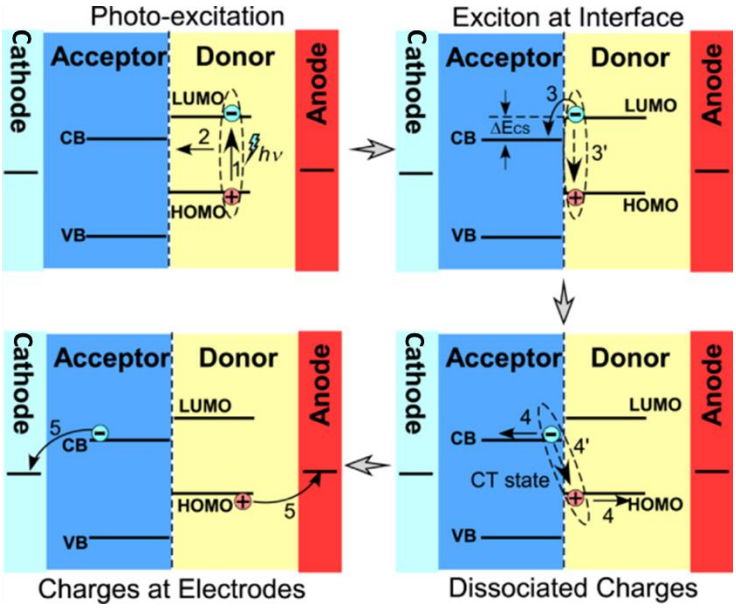

Figure 2.1 Working principles of solar cell from light absorption to charge collection.[2]

The device working principle from light absorption to charge collection is shown in Figure 2.1. The first figure is the light absorption process. When photons are absorbed by the semiconducting materials, excitons are generated. The excitons generated are strongly bound electron-hole pairs, and can be diffused inside the organic semiconductor. Electrons and holes can be separated at a donor-acceptor interface with tuned highest occupied molecular orbital (HOMO) and lowest unoccupied molecular orbital (LUMO). Generally, the typical exciton diffusion length in an organic semiconductor is around 8-12nm. The exciton dissociation occurs only at the interface between the donor and the acceptor.[3] If exciton do not reach the interface, they recombine and the absorbed energy is dissipated without generating photocurrent. Therefore, to efficiently generate power, the excitons need to be dissociated and collected at electrodes before recombination. The performance of an OPV cell is characterized by a J-V curve, as seen in Figure 2.2a, below.

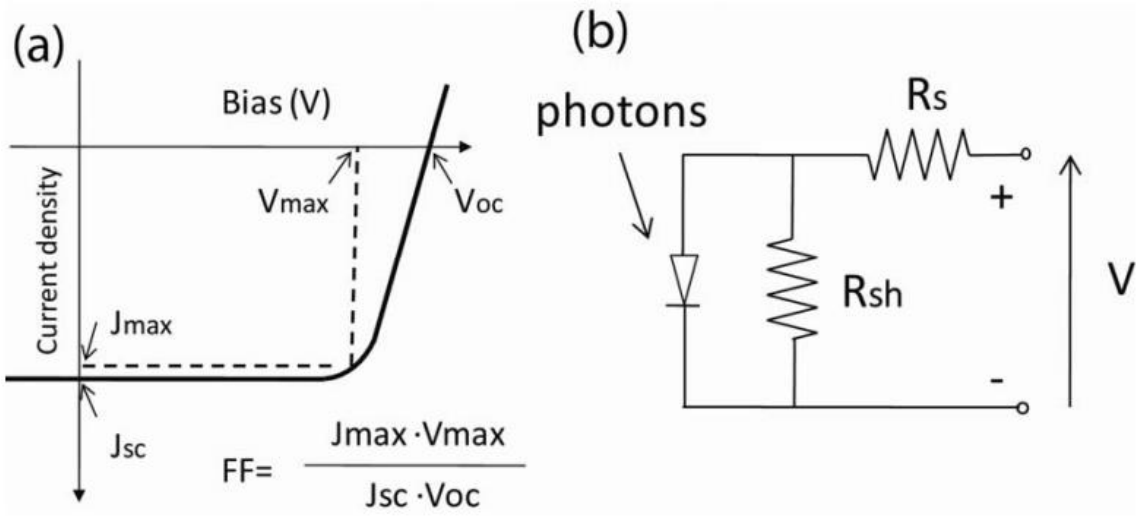

Figure 2.2 (a) The definition of fill factor (FF), J_{max}: current density at the maximum of J × V in 4th. quadrant, Vmax: bias at the maximum of J * V in 4th. Quadrant; (b) Circuit of photovoltaic device, R_s: series resistance, R_{sh}: shunt resistance.

Figure 2.2a shows the current density and voltage curve of photovoltaic device (PV) under the light and an electrical circuit of PV is shown in Figure 2.2b. Without light, there is no current at the short circuit condition. Under the light, the incident photons generate current by exciton generation and separation. The current-voltage product is negative and the cell generates power when the voltage is between 0 and open circuit voltage (V_{oc}). At V< 0, the illuminated device acts as a photodetector, consuming power to generate a photocurrent that is light dependent but bias independent. At V > V_{oc}, the device again consumes power. This is the region where light emitting diodes operate. Important parameter for evaluating the performance of the solar cell includes: short circuit current density (J_{sc}), V_{oc}, input power (P_{in}) and fill factor (FF).

The fill factor is calculated as

$$FF = \frac{J_m V_m}{J_{sc} V_{oc}}$$

to denote the part of the product of V_{OC} and J_{SC} that can be used. With this, the power conversion efficiency can be written as

$$Power = \frac{P_{OUT}}{P_{IN}} = \frac{J_{MAX} V_{MAX}}{P_{IN}} = \frac{FF J_{SC} V_{OC}}{P_{IN}}$$

2.1.2 Active Materials Selection

A new structure based on the mixture of the electron donor and acceptor material is prepared to increase the interfacial area and thus to improve exciton dissociation efficiency. This mixture of materials is spin coated on the surface of an electrode to form a heterojunction layer, also called a bulk heterojunction layer(Figure 2.3-2.4). Figure 2.3-2.4 shows different heterojunction solar cell structures and corresponding band diagrams.[4] In the literature, different types of heterojunction cells are considered by using different polymer blends and molecules.. Table 2.1 Summaries the device characteristics for various solar cell devices fabricated with different organic materials with System Year Fill Factor [%] Efficiency white light [%] Reference POPT/CN-PPV 1998 1.9%,[5] MDMO-PPV/PCBM 2001 3.0%,[6,7] P3HT/ PCBM 2002 4.9%,[8,9] PTB7/PC71BM 2010 7.4%.[10] Among different polymers, the buckminster fullerene C60 drew a lot of attention because of its strong electron acceptor properties. It's based on experiments in bulk heterojunction cells that when C_{60} is mixed with hole conducting materials, photoconductivity increases under illumination.[10] But, C_{60} shows a tendency to crystallize in the polymer mixture. This leads to the development of PCBM, a derivative of C_{60}. By forming smaller crystal structures in the blend, the solubility of PCBM increases. Figure 2.4 shows the chemical structure of PCBM. For the electron donor material, PPV derivatives were widely used until the development of P3HT (poly-3- hexylthiophene) (Figure 2.5). Being able to absorb photons at higher wavelengths than the PPV derivatives, P3HT makes a more suitable partner for PCBM in organic solar cells. Studies on this pair show that charge mobilities can be increased by slow drying of this layer during the fabrication. Therefore, charges can be collected more effectively forming the space charge region smaller. Some commonly used conjugated polymers are shown in Figure 2.5.Two important representatives of hole-conducting donor type polymers

are MDMO-PPV (poly[2-methoxy-5- (3,7- dimethyloctyloxy)]-1,4-phenylenevinylene) and P3HT.[11]

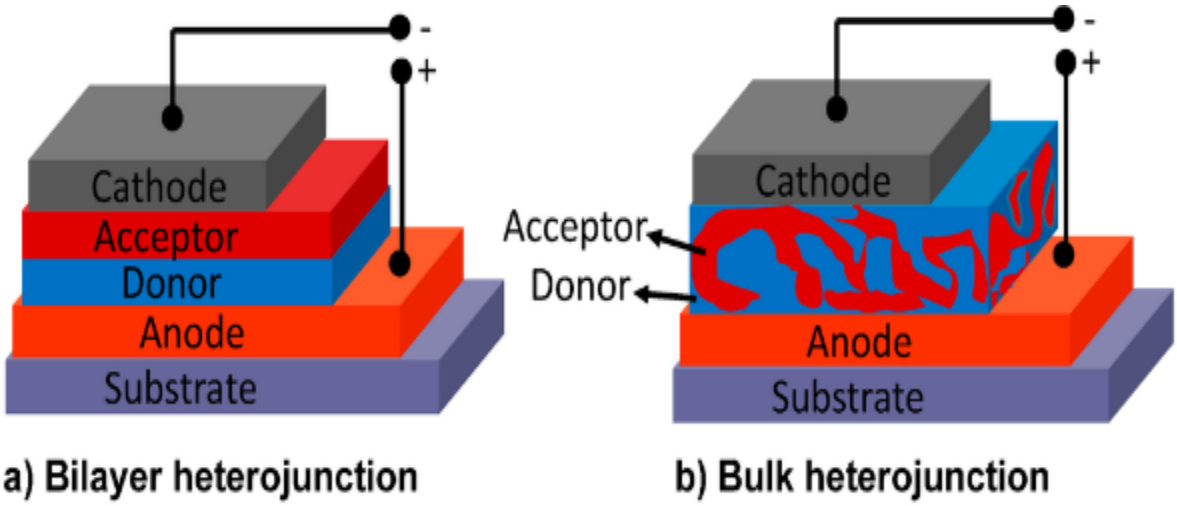

Figure 2.3 Different heterojunction solar cell structures and corresponding band diagrams.

Table 2.1 Summary of device characteristics for various solar cell devices fabricated with different organic materials.

System	Year	Fill Factor [%]	Efficiency [%]	Reference
POPT/CN-PPV	1998	35	1.9	[5]
MDMO-PPV/[60]PCBM	2001	51	3.0	[6]
P3HT/PCBM	2002	55	4.9	[8]
PTB7/PC71BM	2010	69	7.4	[10]

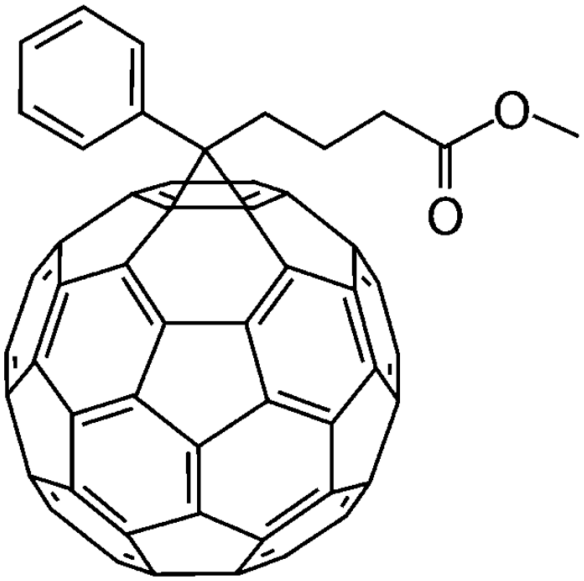

Figure 2.4 Electron-conducting acceptor molecule, a soluble derivative of C60, namely PCBM (1-(3-methoxycarbonyl) propyl-1-phenyl[6,6]C61)

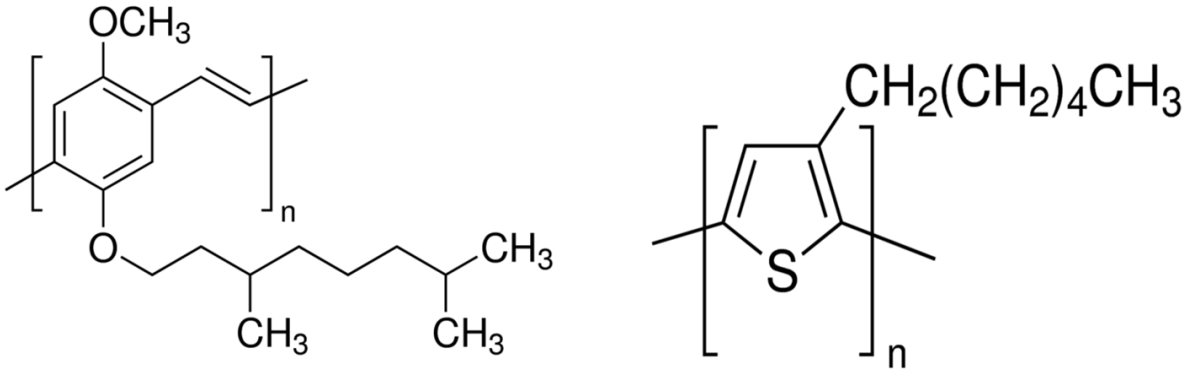

MDMO-PPV **P3HT**

Figure 2.5 Some commonly used conjugated polymers are shown. Two important representatives of hole-conducting donor type polymers are MDMO-PPV (poly[2-methoxy-5-(3,7-dimethyloctyloxy)]-1,4-phenylenevinylene), P3HT (poly(3-hexylthiophene-2,5-diyl).

2.2 Introduction of Perovskite Solar Cells

2.2.1 Classification

Perovskite solar cell was first developed in a dye sensitized solar cell (DSSC) configuration using a mesoporous TiO_2 structure.[12] In 2009, Miyasaka and co-workers were the first to utilize the perovskite ($CH_3NH_3PbI_3$ and $CH_3NH_3PbBr_3$) nanocrystal as absorbers in DSSC structure. It achieved an efficiency of 3.8%.[12] Park and Gratzel et al. reported a solid state perovskite solar cell by using the solid hole transport layer to improve stability in 2012.[13] After that, several important breakthroughs in device performance have been reached by using mesoporous structure.[12-21] However, these mesoporous devices need a high temperature sintering of TiO_2 layer that could increase the processing time and cost of cell production. Sum et al. and Snaith et al. independently reported that the methylammonium-based perovskites provides long charge carrier diffusion lengths (~100 nm for $CH_3NH_3PbI_3$ and ~1000 nm for $CH_3NH_3PbI_{3-x}Cl_x$, Figure 2.6).[22,23] Recently, single crystals of $CH_3NH_3PbI_3$ were found to reach exciton diffusion lengths larger than 175 um.[24] Further studies demonstrated that perovskites exhibit ambipolar behavior, indicating that the perovskite materials themselves can transport both electrons and holes between the cell terminals.[22] All of these results indicated that a planar structure was feasible. The first successful demonstration of the planar structure can be traced back to the perovskite/fullerene structure reported by Guo et al.,[25] showing a 4% efficiency. The low efficiency reported at that time was due to the inferior film quality and inadequate absorption of the perovskite film.[25] The breakthrough of the planar perovskite structure was obtained by using a dual source vapor deposition, providing dense and high quality perovskite films that achieved 15.4% efficiency.[26] Recently, the efficiency of the planar structure was pushed to over 19% through interface engineering.[18] These results showed

that the planar structure could achieve similar device performance as the mesoporous structure. The evolution of the structure of perovskite is shown in Figure 2.7.

The planar structure can be divided into two categories depending on which selective contact is used on the bottom, that is, regular (n-i-p) and inverted (p-i-n); the device structures are shown in Figure 2.7 b and c, respectively. The regular n-i-p structure has been extensively studied and could be traced back to dye sensitized solar cells. The p-i-n structure is derived from the organic solar cell, and usually, several charge transport layers used in organic solar cells were successfully transferred into perovskite solar cells.[17]

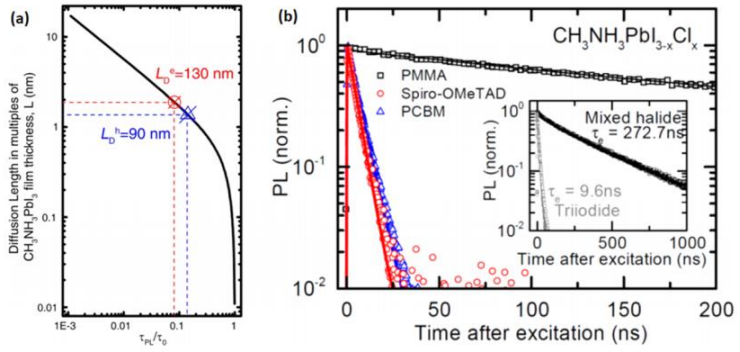

Figure 2.6 (a) Plot of exciton diffusion length versus PL lifetime quenching ratios for $CH_3NH_3PbI_3$. Reprinted with permission from ref 16. Copyright 2013American Association for Advancement of Science. (b) Time-resolved PL of the mixed halide perovskite (CH3NH3PbI3-XClx) with quenching. Reprinted with permission from ref.17. Copyright 2013 American Association for Advancement of Science.

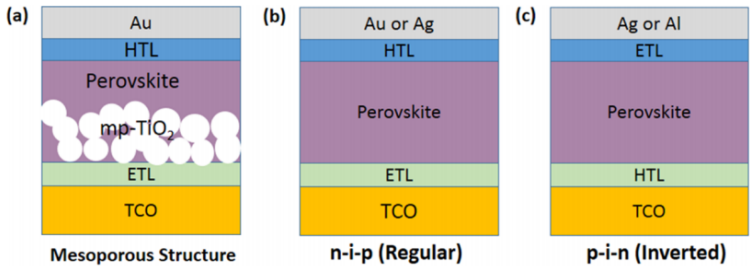

Figure 2.7 Three typical device structures of perovskite solar cells: (a) mesoporous, (b) regular planar structure, and (c) inverted planar structure.

2.2.2 Active Materials Selection

To deposit $CH_3NH_3PbI_3$ perovksite on a substrate, two methods are typically used, that is, one-step and two-step coating methods. Perovskite are formed either by spin-coating a mixed CH3NH3I and PbI2 solution (one-step coating) or spincoating PbI2 followed by depositing CH3NH3I (two-step coating). For the one-step coating method, CH_3NH_3I and PbI_2 are dissolved in as a polar aprotic solvent like *N*,*N*-dimethylformamide (DMF), gammabutyrolactone (GBL), or dimethyl sulfoxide (DMSO), and is used as a coating solution. Drying and annealing processes follow spin coating. For the two-step coating method, PbI2 solution is first coated on the substrate to form a PbI_2 film and then a 2-propanol solution of CH_3NH_3I is spun on the PbI_2 film. In order to prepare high-quality perovskite films, it is important to adjust coating parameters such as spinning rate and time, temperature, solution wettability and viscosity, etc. Compared to one-step spin-coating, two-step spin-coating was found to exhibit better photovoltaic performance due to better morphology and interfaces,[27] which indicates that morphology control of perovskite film is crucial in achieving high-efficiency perovskite solar cells.

2.3 References

1. Stephen R. Forrest, *MRS bulletin*, 2005, **30**, 28.

2. Liu, Ruchuan., *Materials,* 2014, **7**, 2747-2771.

3. P. Heremans V. I. Arkhipov, and H. Bassler, *Appl. Phys. Lett.*, 2003, **82**, 4605.

4. McGhee MD, Topinka MA. *Nat Mater.*, 2006; **5**, 675-6.

5. Granstrom M, Petritsch K, Arias AC, Lux A, Andersson MR, Friend RH. *Nature,* 1998, **395**, 257-60.

6. Shaheen SE, Brabec CJ, Sariciftci NS, Padinger F, Fromherz T, Hummelen JC. *Appl. Phys. Lett.*, 2001, **78**, 841-3.

7. Schilinsky P, Waldauf C, Brabec CJ. *Appl. Phys. Lett.*, 2002, **81**, 3885-7.

8. Padinger F, Rittberger RS, Sariciftci NS. *Adv Funct Mater.*, 2003, **13,** 85-8.

9. Liang YY, Xu Z, Xia JB, Tsai ST, Wu Y, Li G, et al. Adv. Mater., 2010, **22**, 135.

10. Steckl AJ. *Nature Photon.*, 2007;1(1):3-5.

11. Dennler G, Lungenschmied C, Neugebauer H, Sariciftci NS, Labouret A. *J Mater Res.*, 2005, **20**, 3224-33.

12. A. Kojima, K. Teshima, Y. Shirai, T. Miyasaka, *J. Am. Chem. Soc.*, 2009, **131**, 6050−6051.

13. J.-H. Im, C. R. Lee, J. W. Lee, S. W. Park, N. G. Park, *Nanoscale* 2011, **3**, 4088−4093.

14. H. S. Kim, C. R. Lee, J. H. Im, K. B. Lee, T. Moehl, A. Marchioro, S. Moon, R. Humphry-Baker, J. H. Yum, J. E. Moser, M. Gratzel, N. G. Park, *Sci. Rep.*, 2012, **2**, 591.

15. M. M. Lee, J. Teuscher, T. Miyasaka, T. N. Murakami, H. J. Snaith, *Science*, 2012, **338**, 643−647.

16. J. Burschka, N. Pellet, S. J. Moon, R. Humphry-Baker, P. Gao, M. K. Nazeeruddin, M. Gratzel, *Nature*, 2013, **499**, 316−319.

17. J. H. Im, I. H. Jang, N. Pellet, M. Gratzel, N. G. Park, *Nat. Nanotechnol*., 2014, **9**, 927−932.

18. J. You, Y. Yang, Z. Hong, T. B. Song, L. Meng, Y. Liu, C. Jiang, H. Zhou, W. H. Chang, G. Li, Y. Yang, *Appl. Phys. Lett.*, 2014, **105**, 183902.

19. H. Zhou, Q. Chen, G. Li, S. Luo, T. B. Song, H. Duan, Z. Hong, J. You, Y. Liu, Y. Yang, *Science*, 2014, **345**, 542−546.

19. N. J. Jeon, J. H. Noh, Y. C. Kim, W. K. Yang, S. Ryu, S. I. Seok, *Nat. Mater.*, 2014, **13**, 897−903.

20. N. J. Jeon, J. H. Noh, W. S. Yang, Y. C. Kim, S. C. Ryu, J.Seo, S. I. Seok, *Nature* 2015, **517**, 476−480.

21. W. S. Yang, J. H. Noh, N. J. Jeon, Y. C. Kim, S. C. Ryu, J. Seo, S. I. Seok, *Science*, 2015, **348**, 1234−1237.

22. G. C. Xing, N. Mathews, S. Y. Sun, S. S. Lim, Y. M. Lam, M. Gratzel, S. Mhaisalkar, T. C. Sum, *Science*, 2013, **342**, 344−347.

23. S. D. Stranks, G. E. Eperon, G. Grancini, C. Menelaou, M. J. P. Alcocer, T. Leijtens, L. M. Herz, A. Petrozza, H. J. Snaith, *Science*, 2013, **342**, 341−344.

24. Q. Dong, Y. Fang, Y. Shao, P. Mulligan, J. Qiu, L. Cao, J. Huang, *Science*, 2015, **347**, 967−970.

25. J. Y. Jeng, Y. F. Chiang, M. H. Lee, S. R. Peng, T. F. Guo, P. Chen, T. C. Wen, *Adv. Mater.*, 2013, **25**, 3727−3732.

26. M. Liu, M. B. Johnston, H. J. Snaith, *Nature*, 2013, **501**, 395−398.

27. J.-H. Im, H.-S. Kim, N.-G. Park, *APL Mater.* 2014, **2**, 081510.

3 TRANSPARENT AND FLEXIBLE COMPOSITE ELECTRODE

3.1 Introduction

Recently, research and development of innovative transparent and highly conductive electrodes have gained significant attention due to their high demand in many optoelectronic applications including organic solar cells (OSC), organic light emitting diodes (OLEDs) and liquid crystal displays.[1-5] As of today, indium tin oxide (ITO) is the state-of-the-art material for transparent electrodes due to its excellent electrical sheet resistance (Rs) and optical transparency. In the case of OSC, highly conducting metals with suitable work functions are used as a counter electrode to the ITO. However, with the increasing interest in building-integrated photovoltaics (BIPV), the concept of transparent solar harvesting panels which can be used to replace conventional glass windows has gained considerable popularity in building energy friendly establishments. Conventional metal counter electrodes are not suitable for this application due to their opaqueness. AgNWs electrodes, which can be used to fabricate highly transparent electrodes have proven to be a solution for this problem.[6] Vacuum free, low temperature, cost effective fabrication techniques such as, spin coating, spray coating and dry transfer can be used to cast these electrodes.[7, 8] One of the main challenges is the high surface roughness of the electrodes, due to the protruding AgNWs.[9] This high roughness is detrimental in the case of OSC as it can result in electrical breakdown across the active layer, which makes the device inoperative. To address this problem, a TiO_x or ZnO capping layer has been used to create robust, efficient AgNW-based transparent electrodes for OSC.[10] Among various fabrication methods that have been developed to fabricate ZnO films, sol-gel-derived ZnO films are widely used in inverted organic solar cells as a hole blocking layer because it can be easily developed by solution processing.[11] However, if the capping layer is deposited onto the AgNW

directly by spin coating, the roughness of the modified electrode is still relatively high (~100nm). The possibility of having electrical breakdown thus has not yet completely eliminated.

It is therefore necessary to develop a new method to fabricate this composite electrode without electrical breakdown. ZnO nanostructures such as nanowires, nanorods and nanogratings, have attracted considerable attention over the past few years due to their unique electrical and optical properties at the nanoscale.[12-14] Highly oriented, periodic ZnO nanostructure arrays have been shown to improve the performance of optoelectronic devices.[15] There are several ways to fabricate ZnO nanostructures. For example, highly ordered ZnO nanostructures can be obtained via vapor-liquid-solid (VLS) growth on patterned catalyst or seed sites generated by electron-beam lithography (EBL).[16] However, one of the problems with the VLS techniques is that catalyst residual atoms may be left in the resulting film. These residues act as impurities which can degrade the device performance. Furthermore, high temperatures (~800^{o}C) associated with the VLS method also pose limitations on the type of substrates that can be used to grow the nanostructured films. Hydrothermal growth and vapor deposition can be used to avoid these problems since these processes are catalyst-free and can be conducted at a lower temperature. However, it is difficult to grow highly ordered ZnO nanostructures on a rough metal nanowire surface using these techniques.

Here, with the goal of achieving highly conductive and transparent electrodes for solar harvesting application, an efficient method is developed to fabricate highly ordered ZnO NRs on top of AgNW by the Spin-on Nanoprinting (SNAP) technique.[17, 18] ZnO NRs so developed yield excellent optical and electrical properties. The composite films that were fabricated show a 30 Ω/□ sheet resistance and a 77% optical transmission at 550nm. In addition, the SNAP technique generates a smooth surface since AgNW are not allowed to protrude through the ZnO film

during the SNAP process. The composite electrodes are very stable under tensile bending stresses and ultimately eliminated the short circuit problem for AgNW electrode based devices. This all-solution process provides an efficient method to prepare well-ordered ZnO NRs on top of AgNWs, which will be highly beneficial for organic solar cells as a multifunctional layer. With this ZnO capping layer, AgNW films show better electrical properties and mechanical flexibility. Moreover, the ZnO film solves the electrical breakdown problem, provides protection against oxidation, damp-heat conditions, and even resists extreme chemical environments. To the best of our knowledge, ZnO NRs on a flexible transparent AgNW electrode for OSC applications has not been reported. With the use of this NR ZnO-AgNW-ZnO electrode, the power conversion efficiency (PCE) of an organic solar cell is improved from 2.5% to 2.8%.

3.2 Nanorod ZnO-AgNW-ZnO electrode fabrication

The schematic of the NR ZnO-AgNW-ZnO electrode fabrication is shown in Figure 3.1. Step a & b: A PVA solution was spun on a pre-fabricated silicon (Si) mold with nanorods, followed by curing at 100^{o}C for 2mins and demolding. Step c: This film was then directly transferred onto another substrate which was already coated with a layer of PVA film to assure good adhesion of the patterned film with this substrate. Step d: After heating two layers of PVA films together at 100^{o}C, a sol-gel ZnO film was prepared on the PVA nanostructure according to a previous report.[11] The ZnO solution was spun on top of PVA nanohole structure at a spin speed of 6000rpm for 1 min and heated at 150^{o}C for 1hr to form ZnO gel. This is followed by the application of AgNW solution on top of ZnO layer by spin-coating. We made three sets of samples with different thicknesses of the AgNW layer by adjusting the spin speed. The spin

speed used for sample 1, 2 and 3 are 700, 1500, and 3000 rpm, resulting in AgNW film sheet resistance of 30, 136, and 224 Ω/□ respectively. Step e: Another ZnO layer spin-coated onto the ZnO-AgNW layer prevents the AgNWs from local melting-induced disconnection at the cross junctions. This results in enhanced thermal stability of the AgNWs.[19] A PAN solution was spin-coated on top and served as a tape to peel off the ZnO-AgNW-ZnO composite and PVA together. The PAN solution was prepared by dissolving 8wt% of high molecular weight (Mw 150,000) PAN in N, N-dimethylformamide (DMF). Step f: Finally, the top sacrificial layer, PVA, was removed by hot water, revealing the ZnO NR.

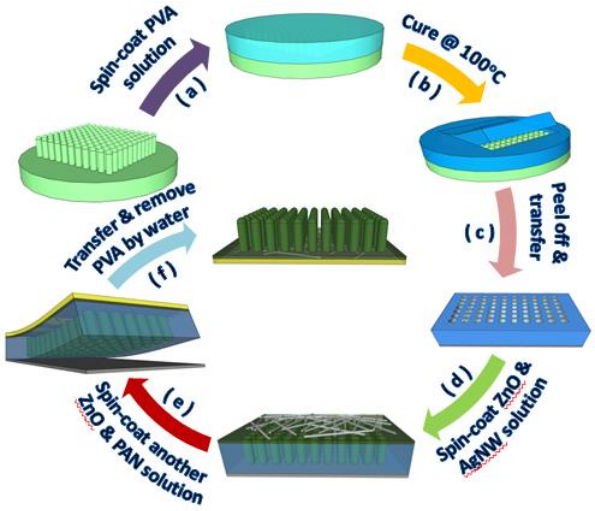

Figure 3.1 schematic of the process flow to create nanostructure ZnO-AgNW electrode.

3.3 Device fabrication

Semitransparent organic solar cells were fabricated with patterned ITO-coated glass substrates (sheet resistance: 15Ω/□). A very thin layer of polyethylenimine ethoxylated (PEIE), spin-coated from solution, is used to reduce the ITO electrode work function as described by Zhou et, al[20]. The P3HT:PCBM blend with a weight ratio of 1:1 in dichlorobenzene solution (20 mgmL^{-1}) was spin cast at 700 rpm for 60 s on top of the PEIE layer to form a ~200 nm-thick active layer. A D-sorbitol doped PEDOT:PSS solution was then spin-coated on top of NR ZnO-AgNW-ZnO

electrode at 3000 rpm for 40 s and annealed at 140^{o}C for 15 mins to form an adhesive layer. After drying both P3HT:PCBM and PEDOT:PSS layer, they are laminated together under the heat to make the two substrates tightly glued together. To study the role of NR ZnO on solar cell efficiency, a planar ZnO-AgNW-ZnO electrode was fabricated following the same procedure except using a planar mold.

3.4 Characterization Methods

An X-ray photoelectron spectroscopy measurement was conducted to examine the presence of ZnO in the nanorod structure. Mg Ka photons with energy of 1253.6 eV were used as a monoenergetic X-ray source and the binding energies of the spectrum were calibrated by taking the carbon C1s peak (285 eV) as a reference. Figure 3.2 shows the XPS spectrum of the ZnO containing the NR structure. As shown in Figure 4, C1s, Ag3d3, O1s and Zn2p3/2 peaks appear at 285 eV, 374eV, 531 eV and 1021 eV, respectively. This proves that the NRs are made up of ZnO. Here, the appearance of Ag3d3 is because ZnO film between AgNW and atmosphere is very thin. The signals of Ag can be still detected from analytes below the ZnO surface.

For evaluating the solar cell performance, a solar simulator with a 300 W Xenon lamp and AM1.5G global filter were used. The light intensity was calibrated using a silicon photovoltaic reference cell (Newport, 91150V). Current-voltage characteristic curves were measured with a Keithley 2635A source measurement unit. The surface morphologies and nanostructure of the samples were characterized by atomic force microscopy (AFM, Dimension 3100) with a SPM probe model and field-emission scanning electron microscopy (SEM, Zeiss ULTRA-55). Diffuse transmission and reflection were measured by a goniometer combined with a integrating sphere and CCD spectrometer.

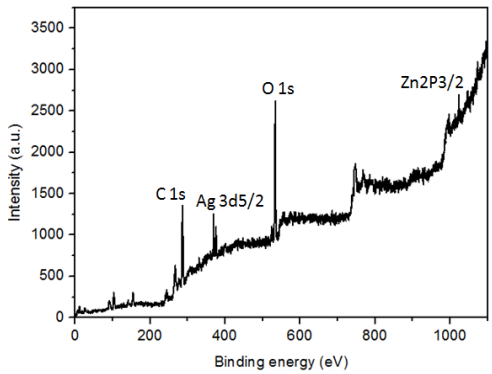

Figure 3.2 XPS spectrum of ZnO containing a nanoscale rod structure.

3.5 Characterization of nanostructured electrodes

With the current fabrication scheme, ZnO NRs were developed with underlying AgNW film. As a result of the overlying ZnO film, electrical shorts are avoided. The ZnO nanostructured film produced using SNAP is the positive replica of the mold. This all-solution processing technique provides a new and efficient method to prepare highly ordered ZnO NRs on top of AgNW, which also provides protection against oxidation of the AgNW layer. The Scanning Electron Microscopy (SEM) image shown in Figure 3.3a clearly shows the AgNW layer, with AgNWs having an average diameter of ~35 nm and length of ~15 μm. SEM data on highly ordered ZnO NRs without AgNW are presented in Figure 3.3b. ZnO NRs with a bottom layer of AgNW are shown in Figure 3.3c, demonstrating the networked structure of the AgNW layer underneath the ZnO nanostructured layer. A regular pattern with dimension of 400nm in diameter, 600nm in center-to-center distance and 200nm in height is shown in Figure 3.3d. Moreover, the fact that AgNW cannot be found on top of the NRs in Figure 3.3d, implies that the AgNW layer is completely covered by the overlying ZnO layer. From the SEM cross-section and AFM top view given in the SI, it is clear that NR ZnO can be successfully printed using SNAP technique.

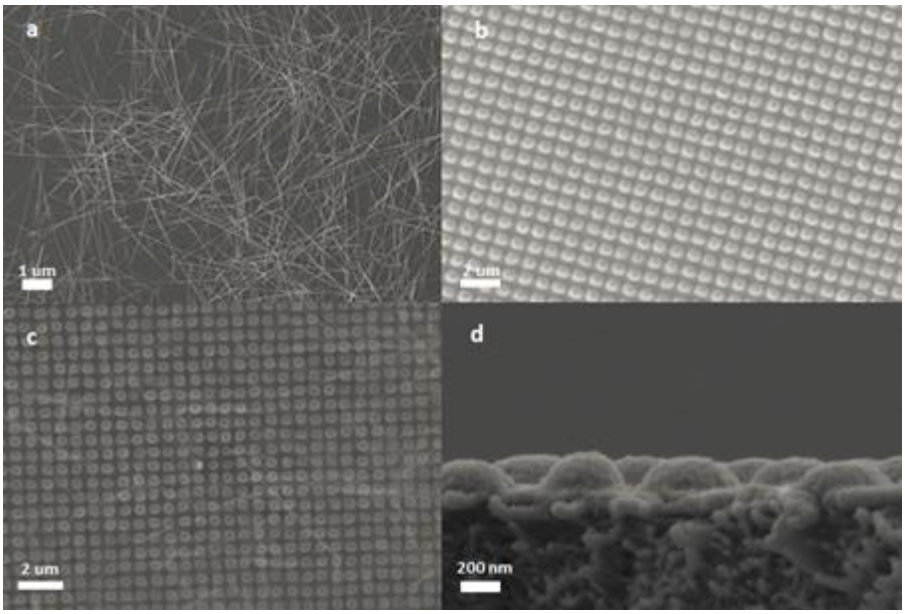

Figure 3.3 SEM top view image of (a) pure AgNW layer, (b) pure ZnO nanostructured layer, (c) Ag-NW layer beneath ZnO nanostructured layer, and (d) cross-sectional view of (c).

In order to evaluate the potential of ZnO-AgNW-ZnO film for use as a transparent electrode for organic solar cells, optical transparency and sheet resistance of planar (control electrode) as well as NR ZnO-AgNW-ZnO electrodes were studied. The transmittance spectra of the ZnO-AgNW-ZnO film at different thicknesses of AgNWs are presented for sample 1-3 in Figure 3.4a. An ITO-glass electrode was used as a frame of reference. The sheet resistance of ZnO-AgNW-ZnO film for sample 3 measured (on the top of the ZnO film) using four probe technique was 30 Ω/□ with 77% transmission at 550 nm, while the ITO coated substrate showed 15 Ω/□ sheet resistance and 90% transmission at 550 nm. Although the transmittance of the ITO film was higher than that of the composite film at 550 nm, the average transmittance values of the composite and ITO films were not significantly different in the range of 350 – 800 nm. This is due to the significant reduction in transmittance near the UV region and dramatic fluctuations over the visible region of the ITO film.[21] The transmittance vs sheet resistance of the ZnO-

AgNW-ZnO and AgNW films prepared with various AgNW densities are further compared in Figure 3.4b. Interestingly, the sheet resistance of the composite is found to be lower than that of AgNW films. Therefore, another advantage of the coated ZnO is that it can play a significant role in increasing the conductivity of the AgNW through its unique electronic properties.

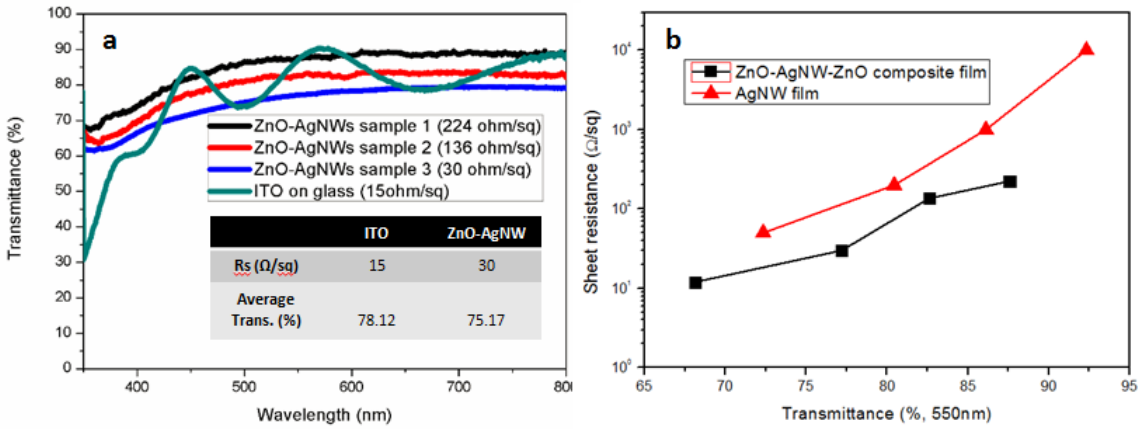

Figure 3.4 (a) Transmittance spectra of samples with different amounts of ZnO-AgNW-ZnO. The inset shows the respective sheet resistance values. All transmittances are inclusive of the glass substrate, (b) Sheet resistance vs. transmittance of AgNW and ZnO-AgNW-ZnO.

Another attractive advantage of conducting NR ZnO-AgNW-ZnO film is its flexibility. To test the mechanical resilience of NR ZnO-AgNW-ZnO film with bending, a bending test has been carried out to measure the sheet resistance as a function of bending cycles. The films were bent to a bending radius of 4 mm. When compared to ITO, this multi-layer electrode on PET substrate showed better flexibility and transparency[21] as shown in Figure 3.5. Here, the resistance variations of the flexible transparent conducting electrodes (TCEs) are expressed as Ω_n/Ω_0, where Ω_n is the sheet resistance after bending and Ω_0 is the initial resistance. As fabricated, ZnO-AgNW-ZnO/PET electrodes have a sheet resistance of about 30 Ω/□ with a linear transmission of 77% at 550nm. The ITO/PET electrodes have a sheet resistance of 70 Ω/□ with the transmission of 91.2% at 550nm. According to Figure 3.5, the resistance variation of ZnO-

AgNW-ZnO/PET maintained a nearly similar value after 500 bending, while that of ITO/PET dramatically increased.

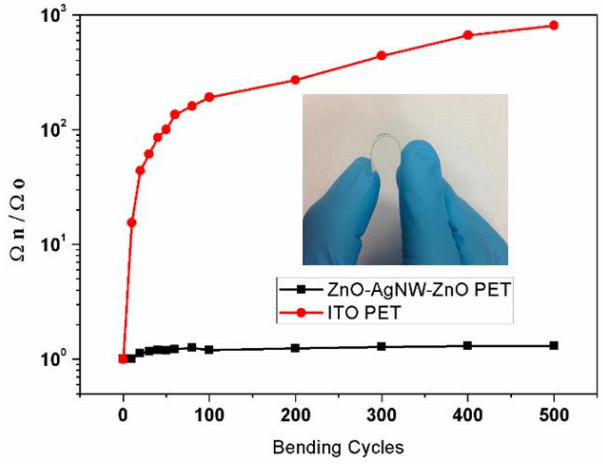

Figure 3.5 Resistance variation as a function of the number of bending cycles with a 4 mm bending radius.

3.6 Photovoltaic properties

In order to demonstrate the application of the ZnO-AgNW-ZnO nanostructured electrodes, OSC was fabricated using this electrode by a laminating technique with P3HT-PCBM as the active layer.[22] The NR ZnO-AgNW-ZnO composite electrode with a thin layer of D-sorbitol doped PEDOT:PSS was pressed onto the P3HT:PCBM layer. The scheme for the fabrication of nanopatterns on P3HT:PCBM layer is shown in the inset of Figure 3.6a. After reheating the whole device, the PEDOT:PSS and composite electrode can be separated from the P3HT:PCBM layer again. Then, the P3HT:PCBM layers shows nanohole structure, which can be seen from the top view AFM image in Figure 3.7. These nanostructures have a diameter of ~500 nm and height of ~130 nm, and center-to-center distance of ~600 nm. Based on the dimensions of nanopatterns from AFM images, the calculations reveal that the surface area of the

nanostructured regions is ~2.2 times higher than that of the planar region (SI). If denser nanopatterns are used, the enhanced interfacial area can further facilitate the collection of electrons in OSC.[23-25]

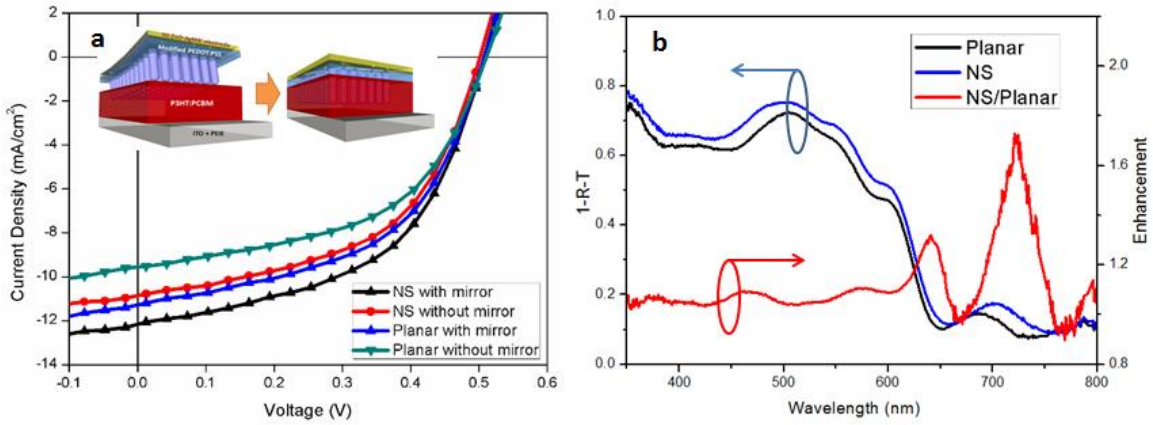

Figure 3.6 a). (Color online) The comparison of the I-V characteristics of the planar and NR ZnO-AgNW inverted solar cell with and without mirror. b) The extracted absorption of OSCs (1 – diffuse reflection (R) – diffuse transmission (T)) with and without NR and the absorption enhancement.

To compare the performance of the nanostructured OSC with that of the planar (control OSC) one, the device is illuminated from the ITO side for all the measurements. A PCE of 2.84%was achieved with V_{oc} = 0.50V, J_{sc} = 10.91 mAcm^{-2}, and FF = 51.7% for the nanostructured device. When the control device was tested, a PCE of 2.53% was obtained with V_{oc} = 0.51 V, J_{sc} = 9.56 mAcm^{-2}, FF = 51.9%. The experimental results show that an obvious change can be seen in the short circuit current density of the device after introducing ZnO NRs. In OSC, photocurrent generation depends on three main factors: 1) the number of absorbed photons; 2) the number of carriers generated by charge separation and 3) the charge-collection efficiency. In order to find the reason for the enhancement of J_{sc}, the absorption from diffuse transmission (T) and reflection (R) is extracted by using 1 – R– T plot as shown in Figure 3.6b. When compared to planar OSC, the extracted absorption of the nanostructured OSC is obviously enhanced. This means that more

light is absorbed in nanostructured OSC.[6, 23, 25] To further clarify the data, the enhancement factor of the extracted absorption of devices with and without nanostructure was calculated, as shown in the Figure 6b. Another reason for the improvement is that the enhanced interfacial area due to nanostructures augments the charge-collection efficiency. The highly ordered ZnO NRs provides a large ZnO/P3HT:PCBM interfacial area, which can accelerate electron transfer and reduce the possibility of charge recombination by building a shortcut for electron transport to the electrode. These shows that the performance of OSCs depends critically on the contact between the active polymer and metal oxide.[26] Figure 6a and Table 1 summarizes the J-V characteristics when a reflective mirror is placed at the back of the semitransparent OSCs. The J_{sc} of the nanostructured device increased from 10.91 mA cm^{-2} to 12.34 mA cm^{-2}, while that of the planar device improved from 9.56 mA cm^{-2} to 11.31 mA cm^{-2}. These results show that, based on the application, the photons transmitted through the semitransparent OSC can still be utilized by the device if a reflective mirror is used.

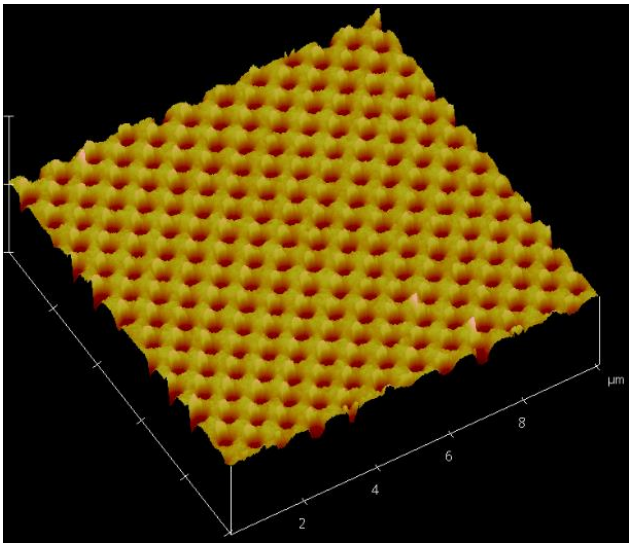

Figure 3.7 Printed nanoholes structures on P3HT:PCBM by the composite electrode.

Table 3.1 Performance of the planar and nanostructure (NS) sandwich solar cell under different conditions

Test conditions (Illuminated from ITO side)	Voc (V)	Jsc (mA/cm2)	FF (%)	PCE (%)
A. Planar without Al mirror	0.51	9.56	51.9	2.53
B. NS without Al mirror	0.50	10.91	51.7	2.84
C. Planar with Al mirror	0.51	11.31	51.3	2.96
D. NS with Al mirror	0.50	12.34	51.8	3.21

Interfacial area calculation: As shown in Figure S3.8, surface area (A cm^2) of nanostructured electrode in a 1 cm^2 footprint can be calculated using the following equation:

$$A = \frac{\pi D \cdot H}{S} + 1$$

where S is the area in a unit cell, D and H are the diameter and height of each pillar, respectively;

$$S = \frac{\sqrt{3}}{2} L^2$$

Where L is the distance between the centers of two pillars.

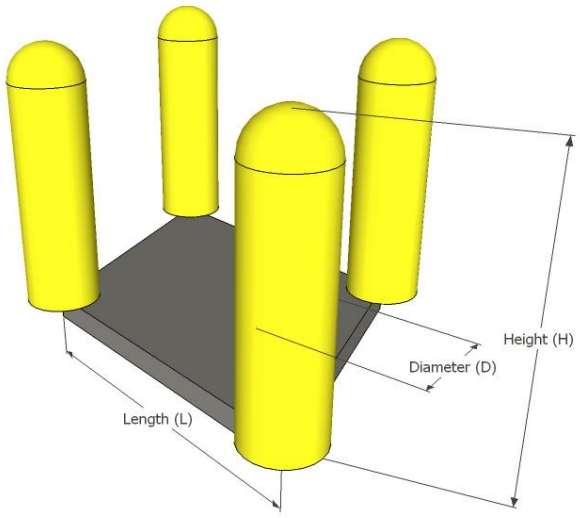

Figure 3.8 Surface area calculation modeling.

The flexibility of this fabricated electrode is demonstrated by adhering the film on a curved surface and using it to complete an electrical circuit as shown in Figure 3.9.

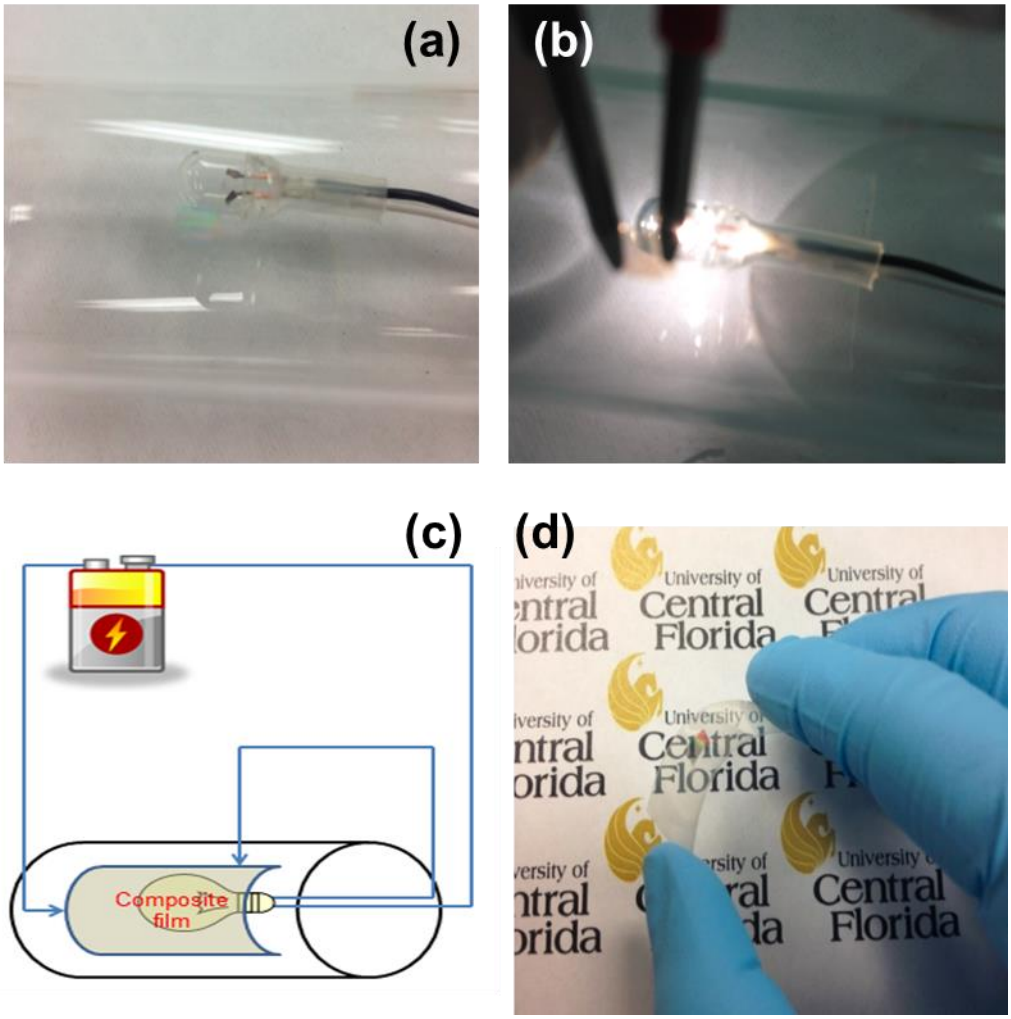

Figure 3.9 NS ZnO-AgNW film stuck on top of a curved glass: a) circuit incomplete; bulb is off, b) circuit complete through the NS ZnO-AgNW region; bulb is on, c) the circuit for the S2a and S2b; d) NS ZnO-AgNW film on flexible PET substrate.

3.7 Conclusion

In summary, we have developed an effective approach to fabricate highly ordered and vertically aligned ZnO NRs on the rough AgNW film. A NR ZnO-AgNW-ZnO multilayer as a composite electrode is prepared with this approach. According to the sheet resistance and transmittance measurements, the composite film is a potential candidate to be used as electrode for semitransparent OSC. In the device design, ZnO-AgNW-ZnO film not only provides good electrical conductivity, but also exhibits excellent mechanical stability. NR ZnO offers protection of the AgNW against oxidation and moisture and larger interfacial area with P3HT:PCBM active layer. Compared to the device with planar ZnO-AgNW-ZnO electrode, the nanostructured electrode design delivers a 14% enhancement in PCE. All solution processing method of fabrication and high flexibility and bendability along with enhanced performance are some of the promising features of this semitransparent OSC.

3.8 References

1. L.-M. Chen, Z. Hong, G. Li and Y. Yang, *Adv. Mater.*, 2009, **21**, 1434-1449.

2. H.-Y. Chen, Michael K. F. Lo, G. Yang, H. G. Monbouquette and Y. Yang, *Nat. Nanotechnol.*, 2008, **3**, 543-547.

3. S.-J. Su, H. Sasabe, T. Takeda and J. Kido, *Chem. Mater.*, 2008, **20**, 1691-1693.

4. J.-Y. Lee, S. T. Connor, Y. Cui and P. Peumans, *Nano Lett.*, 2008, **8**, 689-692.

5. N. Yamamoto, H. Makino, S. Osone, A. Ujihara, T. Ito, H. Hokari, T. Maruyama and T. Yamamoto, *Thin Solid Films*, 2012, **520**, 4131-4138.

6. J. Krantz, T. Stubhan, M. Richter, S. Spallek, I. Litzov, G. J. Matt, E. Spiecker and C. J. Brabec, *Adv. Funct. Mater.*, 2013, **23**, 1711-1717.

7. D. Zhang, K. Ryu, X. Liu, E. Polikarpov, J. Ly, M. E. Tompson and C. Zhou, *Nano Lett.*, 2006, **6**, 1880-1886.

8. A. Madaria, A. Kumar, F. Ishikawa and C. Zhou, *Nano Res.*, 2010, **3**, 564-573.

9. L. Hu, H. S. Kim, J.-Y. Lee, P. Peumans and Y. Cui, *ACS Nano*, 2010, **4**, 2955-2963.

10. D. S. Ghosh, T. L. Chen, V. Mkhitaryan, N. Formica and V. Pruneri, *Appl. Phys. Lett.*, 2013, **102**, 221111.

11. M. N. Kamalasanan and S. Chandra, *Thin Solid Films*, 1996, 288, 112-115.

12. J. J. Dong, X. W. Zhang, Z. G. Yin, J. X. Wang, S. G. Zhang, F. T. Si, H. L. Gao and X. Liu, *Appl. Phys. Lett.*, 2012, **100**, 171109.

13. O. Lupan, T. Pauporté and B. Viana, *Adv. Mater.*, 2010, **22**, 3298-3302.

14. J. J. Cole, X. Wang, R. J. Knuesel and H. O. Jacobs, *Nano Lett.*, 2008, **8**, 1477-1481.

15. S. Kim, C.-H. Kim, S. K. Lee, J.-H. Jeong, J. Lee, S.-H. Jin, W. S. Shin, C. E. Song, J.-H. Choi and J.-R. Jeong, *Chem. Commun.*, 2013, **49**, 6033-6035.

16. H. T. Ng, J. Han, T. Yamada, P. Nguyen, Y. P. Chen and M. Meyyappan, *Nano Lett.*, 2004, **4**, 1247-1252.

17. Z. Yu, B. Duong, D. Abbitt and J. Thomas, *Adv. Mater.*, 2013, **25**, 3302-3306.

18. B. Duong, P. Gangopadhyay, J. Brent, S. Seraphin, R. O. Loutfy, N. Peyghambarian and J. Thomas, *Acs Appl. Mater. Interfaces*, 2013, **5**, 3894-3899.

19. A. Kim, Y. Won, K. Woo, C.-H. Kim and J. Moon, *ACS Nano*, 2013, **7**, 1081-1091.

20. Y. Zhou, C. Fuentes-Hernandez, J. Shim, J. Meyer, A. J. Giordano, H. Li, P. Winget, T. Papadopoulos, H. Cheun, J. Kim, M. Fenoll, A. Dindar, W. Haske, E. Najafabadi, T. M. Khan, H. Sojoudi, S. Barlow, S. Graham, J.-L. Brédas, S. R. Marder, A. Kahn and B. Kippelen, *Science*, 2012, **336**, 327-332.

21. D. Y. Choi, H. W. Kang, H. J. Sung and S. S. Kim, *Nanoscale*, 2013, **5**, 977-983.

22. J. Huang, G. Li and Y. Yang, *Adv. Mater.*, 2008, **20**, 415-419.

23. J. H. Lee, D. W. Kim, H. Jang, J. K. Choi, J. Geng, J. W. Jung, S. C. Yoon and H.-T. Jung, *Small*, 2009, **5**, 2139-2143.

24. S.-I. Na, S.-S. Kim, J. Jo, S.-H. Oh, J. Kim and D.-Y. Kim, *Adv. Funct. Mater.*, 2008, **18**, 3956-3963.

25. X. Li, W. C. H. Choy, L. Huo, F. Xie, W. E. I. Sha, B. Ding, X. Guo, Y. Li, J. Hou, J. You and Y. Yang, *Adv. Mater.*, 2012, **24**, 3046-3052.

26. D. C. Olson, Y.-J. Lee, M. S. White, N. Kopidakis, S. E. Shaheen, D. S. Ginley, J. A. Voigt and J. W. P. Hsu, *J. Phys. Chem. C*, 2007, **111**, 16640-16645.

4 PROBING SOLVENT EFFECTS IN ORGANIC SOLAR CELLS USING ADVANCED AFM TECHNIQUES*

4.1 Introduction

Due to energy depletion and environmental pollution by fossil fuels, bulk heterojunction polymer solar cells (PSC) based on blends of conjugated polymers and fullerene derivatives offer a promising alternative for the next generation of energy sources.[1-4] PSCs have attracted considerable attention due to their simple fabrication procedures and their low production cost compared to inorganic solar cells. However, despite the considerable improvements reported in the field of PSCs, device performance is still inferior to that of inorganic solar cells.[5-7] Thus, intensive research efforts are focused on increasing the power conversion efficiency (PCE) of PSCs. Such efforts include developing new p-type low bandgap polymers with wider wavelength absorption,[8-10] optimizing the morphology of active materials,[11-13] surface engineering,[14] introducing tandem cells,[15-17] and using ternary blend PSCs.[18-20] One such example is to design active layers of PSCs with three components (so called ternary, made of one more acceptors/donors) instead of two components (so called binary, made of one acceptor and one donor) blends to facilitate charge transport by introducing a cascade energy levels by careful selection of the components according to their band gaps.[21-23]

To further improve the performance and repeatability, optimization and design of the devices are critical, especially the optical and carrier transport properties of the active layers. It is increasingly clear that the morphology of the polymer blend phases, as well as their evolution in time, greatly impact the properties and performances of the devices.[24] However, a detailed fundamental understanding of the morphology-functionality relationship is still lacking.

Furthermore, due to the low contrast in the mechanical properties between organic compounds in the blends, characterization of their morphology at the nanoscale has been difficult.

Despite this drawback, it is well understood that in order to obtain devices with higher open circuit voltage (V_{oc}), high electron mobility and strong electron affinity, the ideal acceptor material should offer a higher lowest unoccupied molecular orbital (LUMO) energy level with respect to the highest occupied molecular orbital (HOMO) energy level of the donor. Furthermore, to overcome the absorption limitation and enhance the current density, ternary blends PSCs were developed by adding another donor/acceptor material in the active layer, which extended the absorption of the solar spectrum.[25-27] Meanwhile the value of V_{oc} is related to the HOMO energy level of the donor and the LUMO energy level of the acceptor. V_{oc} of the ternary blend solar cell is sacrificed due to the higher loading of lower LUMO energy level acceptor material.[28-30] Due to the motivation to power consumer devices using solar cells require high V_{oc} to operate, the high performance of the PSC without sacrificing V_{oc} is favored for this study.

In this work, the effect of using a mixture of two (binary) and three (ternary) solvents to synthesize a PTB7:ICBA active layer for PSC have been studied. Binary (chlorobenzene (CB)/ 1, 8-diiodooctane (DIO)) and ternary (chlorobenzene (CB)/chloroform (CF)/1, 8-diiodooctane (DIO)) solvents are used to prepare a blend of the fullerene derivative indene-C_{60} bisadduct (ICBA) and the low-bandgap semiconducting polymer thieno[3,4-*b*]thiophene/benzodithiophene (PTB7). Evaluation of the performance of the PSCs obtained with these active layers show that the active layer prepared with a mixture of three solvents exhibit high V_{oc}. Moreover, it is possible to use an additional electron transporting layer of C_{60} in between the active layer and the LiF layer to obtain a high V_{oc} and PCE for the device. The configuration of the device using the

C_{60} layer in between the active layer and LiF is illustrated in Figure 1a. The chemical structures and energy levels of the components are shown in Figure 1b and 1c, respectively. In this configuration, the C_{60} layer not only works as an effective electron transport layer but also generates a ternary blend effect at the interface between the active material and C_{60} due to its respective work functions. Hence, with solvent manipulation and efficient charge transport through C_{60}, the PCE of the bulk heterojunction PTB7:ICBA PSCs is enhanced from 5.48% to 7.50%. Using advanced AFM techniques some links have been established between the morphology of the nanoscale structures of the active layer, the charge pathways, the purity of the acceptor and donor phases and the performance of the devices.

4.2 Device reparation

All devices are fabricated on indium tin oxide (ITO) patterned glass, which are cleaned by detergent, deionized water, acetone and iso-propanol under sonication for 15mins, respectively. The ITO substrates are exposed to UV-Ozone for 15 min before spin-coating a thin layer (40nm) of poly(ethylenedioxythiophene): poly(styrenesulfonic acid) (PEDOT:PSS). The PEDOT:PSS-coated substrates are then baked at 120 ^{o}C for 20 min and transferred into a nitrogen-filled glove box. Next, blends of PTB7:ICBA (12.5 mg/ml for PTB7, 12.5 mg/ml for ICBA) prepared in so-called binary (CB/DIO) and ternary solvents (chlorobenzene (CB)/chloroform (CF)/1, 8-diiodooctane (DIO)) are spin-coated on the PEDOT:PSS layer to form the active layer. For the devices with C_{60}, a 10 nm insertion layer (C_{60}) is thermally evaporated on top of the active layer. The electrodes are obtained by depositing LiF (1 nm) and

Al (100 nm) by thermal evaporation at a base pressure of 6×10^{-7} Torr through a shadow mask for localized electrodes as depicted in Figure 4.1. The final active area of the device is 7.4 mm^2.

4.3 Photovoltaic and AFM characterization methods

For the evaluation of the PSCs performance, a solar simulator with a 300 W Xenon lamp and AM1.5G global filter are used. The light intensity 100 mW cm^{-2} is calibrated using a silicon photovoltaic reference cell (Newport, 91150V). Current-voltage characteristic curves are measured with a Keithley 2635A source measurement unit. The EQE spectra are measured by Newport model QE-PV-SI coupled with a lock-in amplifier and a calibrated silicon photodetector. PL measurements are performed on a Witec alpha 300 RA confocal Raman system equipped with a Zeiss 20X objective and a 600 lines/mm grating. The samples are excited with 532 nm laser light (~ 200 μW) in ambient air at room temperature. The spectra are collected for an integration time of 0.5 s. Measurements are acquired at different regions of the sample for repeatability. For transient photocurrent measurement, a 532 nm Q-switched, frequency doubled Nd:YAG laser (Minilite I, Continuum) is used to generate a 5 ns pulse. Light pulses with energy less than 1 uJ are used. Photocurrent is measured using a Tektronix MDO3012 Oscilloscope via a Keithley Model SC-9 low noise coaxial cable connected to the two electrodes.

The surface morphology of the samples is characterized by atomic force microscopy (AFM, Dimension 3100, Veeco). Conductive-AFM (c-AFM) measurements are performed on a Multimode AFM from Veeco. The AFM is placed inside a nitrogen-filled glove bag. Conductive platinum-coated probes (Mikromash XSC11/Pt) are used for c-AFM measurement. The tip is grounded and the voltage is applied to the sample. A 100 mW cm^{-2} intensity white light source is used to illuminate the samples. All the samples for c-AFM measurements are fabricated by

depositing a PEDOT: PSS film on ITO-coated glass followed by the active materials on top. The contours presented for c-AFM are obtained by post-processing the conductivity measurements performed in the region represented on the topography images. The contour representation is obtained in Origin using standard plot function of 2D matrices and the levels are selected to allow direct comparison of the data.

4.4 Photovoltaic properties

Recently, high performing PSCs were fabricated from PTB7 and [6,6]-phenyl-C71-butyric-acid-methyl-ester ($PC_{71}BM$) blends, which showed an efficiency of more than 7% with a high current density of about 15 mA cm^{-2}.[9, 31-33] However, the V_{oc} of these devices was limited to less than 0.76 V due to the limitation imposed by the $PC_{71}BM$ LUMO energy levels. To realize a device with a high V_{oc}, $PC_{71}BM$ is replaced by ICBA in the active layer of the PSCs yielding the architecture ITO/PEDOT:PSS/PTB7:ICBA/LiF/Al. The weight ratio of PTB7:ICBA was 1:1. These PSCs demonstrated an impressive V_{oc} of 0.91V, which is considerably higher than that of the PTB7:$PC_{71}BM$ blend.[9] The higher V_{oc} can be explained by the high LUMO energy level of ICBA (-3.7 eV). A standard method is used to estimate the V_{oc} of a conjugated polymer-fullerene solar cell:

$$V_{oc} = (1/e)(\left| E^{Donor}HOMO \right| - \left| E^{Acceptor}LUMO \right|) - 0.3V \quad (1)$$

where e is the elementary charge, -3.7 eV and -5.15 eV were taken as the acceptor (ICBA) LUMO energy and donor (PTB7) HOMO energy, respectively.[34-35] This relationship is commonly used in most PSC system. Although energy levels of the active materials play a main role of determining V_{oc} of organic solar cells, other factors like the temperature and doping concentration also affect the value of V_{oc}.[36-37] Using this equation, a maximum V_{oc} of 1.15V was

predicted for a PTB7:ICBA device. The experimentally determined V_{oc} of 0.91V of the ITO/PEDOT:PSS/PTB7:ICBA/LiF/Al device reported here is one of the highest reported V_{oc} values for the binary blend PSCs using PTB7 polymer.

However, it has been observed that the introduction of ICBA results in a significantly lower short circuit current density (J_{sc}) compared to the PTB7:$PC_{71}BM$ PSC.[38] Lower J_{sc} can be explained by two aspects: (i) the driving force from low-bandgap polymer to ICBA is not being sufficiently strong enough to provide efficient charge separation[39] and (ii) the reduced charge carrier collection efficiency due to disrupted charge transport resulting from molecular disorder near the donor/acceptor interface.[39-40] In order to obtain high J_{sc}, binary and ternary solvent mixtures mixtures are prepared, and active layers of PTB7:ICBA-based PSCs using binary and ternary solvent mixtures covered with a C_{60} layer between the active material and the buffer layer. The performance of the devices has been tested. Table 4.1 summarizes the characteristics of the four types of devices to determine the effect of using ternary solvents and the effect of introducing C_{60} as an additional layer.[41-43] Values given are the averages of ten devices measured.

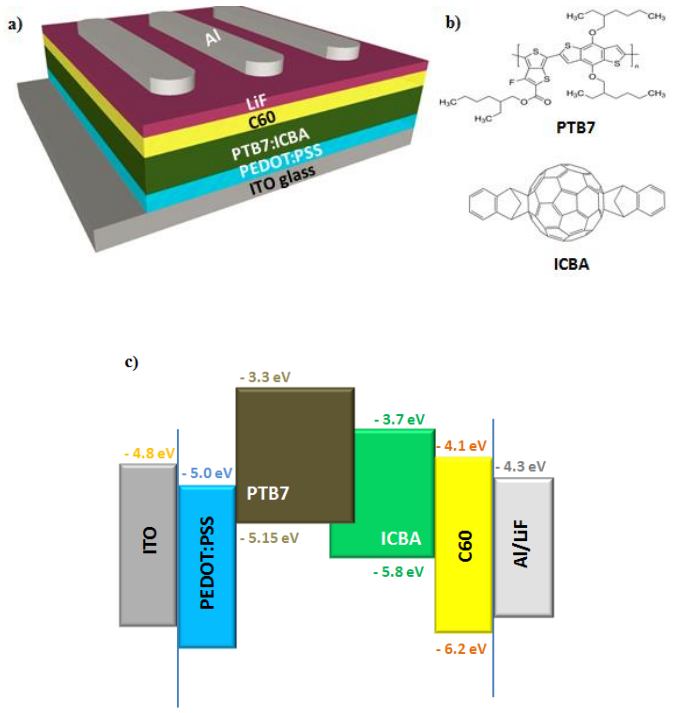

Figure 4.1 Device schematics, chemical structures and energy levels. (a) Schematic illustration of the polymer solar cell (PSC) in presence of the additional C60 layer. (b) Chemical structures of the photoactive materials. (c) Energy levels of all materials used in the device.

Figure 4.2a & 4.2b show the J-V and external quantum efficiency (EQE) plots of PTB7:ICBA devices with and without the C_{60} layer under different solvent combinations, namely binary and ternary solvents. When a ternary solvent mixture of chlorobenzene (CB)/chloroform (CF)/1, 8-diiodooctane (DIO) was used, the J_{sc} of the device was substantially improved from 12.93 to 14.23 mA cm^{-2} along with an enhancement of the fill factor (FF) and V_{oc}. In addition to the improved J_{sc} due to ternary solvent effect, the J_{sc} of the devices in which a 10nm C_{60} layer was inserted between the active layer and LiF layer showed a 9% enhancement of the J_{sc} (14.23 to 15.49 mA cm^{-2}), while maintaining a V_{oc} above 0.9V. It is inferred that the improvement is due to the effective enhancement of charge transport and the reduction of charge recombination at the interface of the active layer and LiF. Performances of devices with different

thickness of C_{60} layer inserted are shown in Figure 4.3. Figure 4.3 presents the curves of the Jsc, FF, and PCE with the inserted C60 layer thickness from 0 to 20 nm. The devices with a C_{60} layer performed better than the devices without C_{60} layer, providing higher FF and Jsc values. The devices with 10 nm C_{60} performed the best; Jsc=14.47 mA cm^{-2}, FF=50%, PCE=6.49%, which is better than the device without C_{60} layer (Jsc=12.93 mA cm^{-2}, FF=46%, PCE=5.48%). To coat PTB7:ICBA layer uniformly, a thick layer of C_{60} is necessary. A thick layer is also required to effectively block hole transport. Therefore, the performance is gradually improved as the C_{60} thickness increases from 0 to 10 nm. However, thicker C_{60} films may introduce more traps for the carriers, which would lead to more recombination and a decrease of Jsc and FF values. This explains the opposite trend observed when the thickness is increased from 10 to 20 nm. The EQE plots in Figure 2b reveal that the PSC devices exhibit a good response in the visible range from 300 to 800 nm, and the EQE is highly solvent dependent. In both cases of binary and ternary solvent mixtures, higher quantum yield was found in devices prepared with C_{60}. Devices with active layers obtained with a ternary solvent mixture showed higher EQE than those prepared with a binary solvent mixture. Hence, the high V_{oc} samples prepared with a ternary solvent system and a C_{60} layer exhibited the highest EQE over the range considered. Its current density value of 15.12 mA.cm^{-2} was calculated from the integration of the EQE spectra with the AM 1.5G reference spectrum, which constitutes an acceptable 3% difference between measured J_{sc} and the calculated current density value. These results are further supported by the steady-state photoluminescence (PL) spectra in Figure 4.4. Based on the PL spectra, measured as a function of wavelength, PTB7 PL is significantly quenched when doped with PC71BM or ICBA as shown. The PL intensity of PTB7:PC71BM is weaker than that of PTB7:ICBA, which indicates the relatively stronger PTB7 exciton

dissociation in PTB7:PC71BM film, which is in agreement with the enhancement of J_{sc} in PTB7:PC71BM (Table 4.2).[44] The PL spectra of PTB7:ICBA samples obtained with binary and ternary solvents do not present any major differences. In order to better understand the improvement of PTB7:ICBA sample obtained with ternary solvent over that of the binary, transient photocurrent measurement is performed to study the difference in charge transit time. From the transient photocurrent measurement given, the values of transit time constants are 1.3 ms and 2.1 ms for ternary solvent sample and binary solvent sample respectively. The shorter transit time for the ternary solvent processed sample suggest that they have better charge transfer/transport properties than the samples processed from binary solvents.

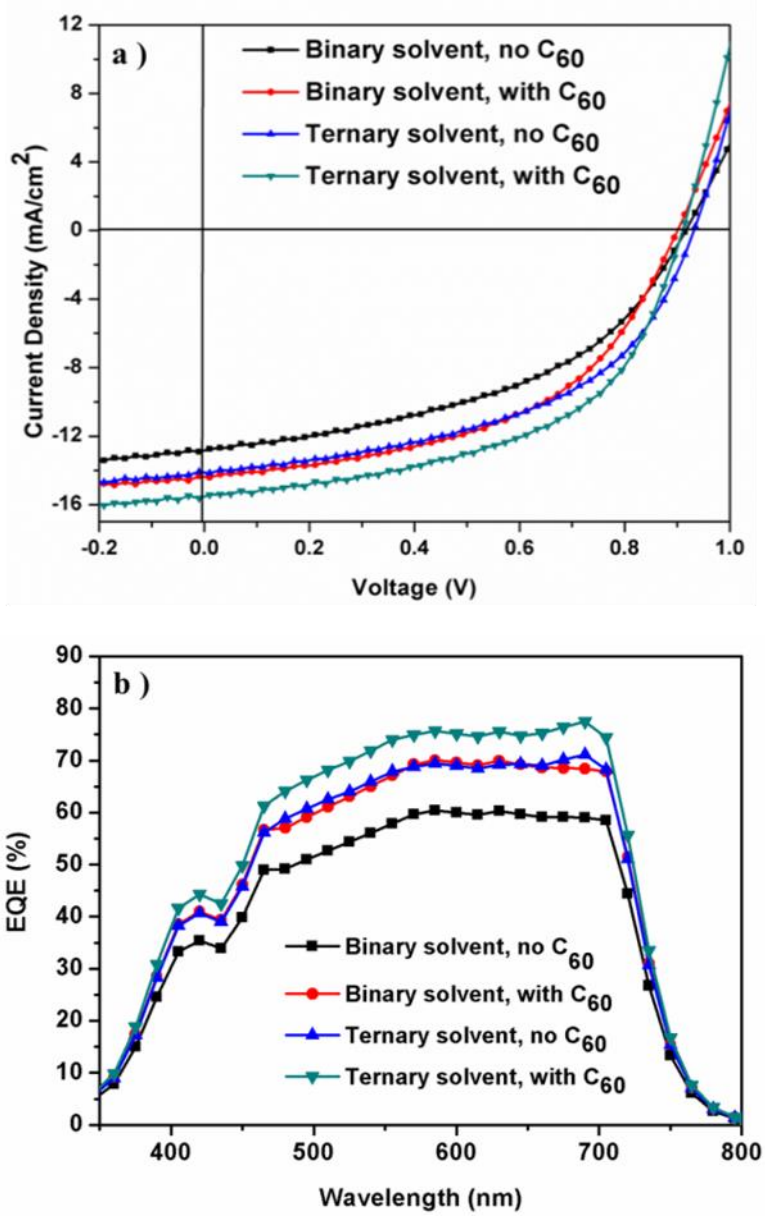

Figure 4.2 J-V and EQE. J-V (a) and EQE (b) curves of PTB7:ICBA solar cells with and without C60 processed from binary solvent-CB/DIO (97:3, v/v) and ternary solvent-CB/CF/DIO (78:19:3, v/v/v).

Champion devices are fabricated by ternary solvent processing, CB/CF/DIO - 78:19:3 (v/v/v) and a 10nm C_{60} layer between the active material and the buffer layer. A PCE of 7.50% is recorded for such devices, which is one of the highest values for ICBA-based bulk heterojunction PSCs, especially with V_{oc} above 0.9 V.

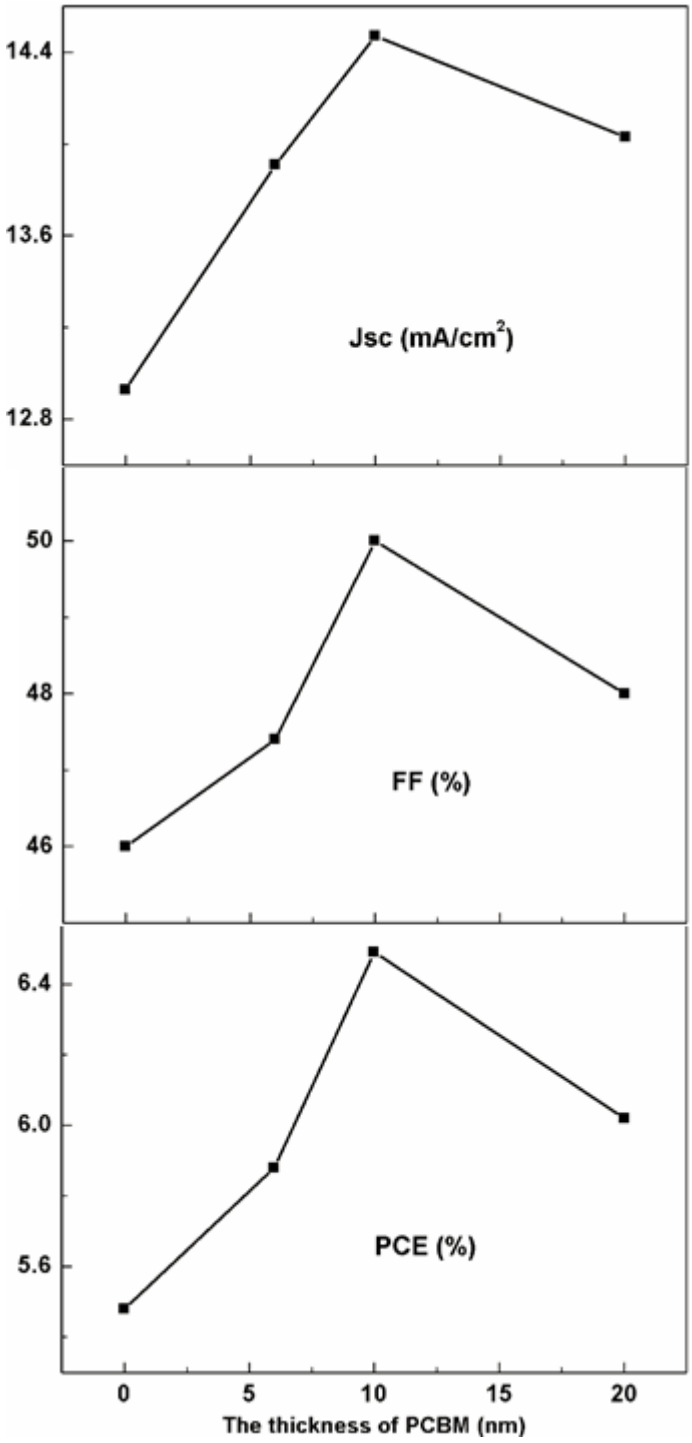

Figure 4.3 Jsc, FF and PCE vs. inserted C60 layer thickness (from 0 nm to 20 nm).

Table 4.1 Photovoltaic results of PSCs by different solvent processing and C_{60} insertion layer.

Processing Solvent	V_{oc} (V)	J_{sc} (mA cm-2)	Calculated J_{sc} (mA cm^{-2})	FF (%)	PCE (%)
CB/DIO (97:3, v/v)	0.91 (0.91)	12.79 (12.93)	12.71	45 (46)	5.24 (5.48)
CB/CF/DIO (78:19:3, v/v/v)	0.93 (0.93)	13.91 (14.23)	13.84	49 (50)	6.34 (6.61)
CB/DIO (97:3, v/v) with additional C_{60}	0.89 (0.89)	14.33 (14.47)	14.04	48 (50)	6.12 (6.49)
CB/CF/DIO (78:19:3, v/v/v) with additional C_{60}	0.91 (0.91)	15.49 (15.64)	15.12	51 (53)	7.26 (7.50)

[a] The calculated J_{sc} values are obtained from the external quantum efficiency (EQE) of the champion cell.

Each data represents the average from ten cells. Data for the champion cell is shown in brackets.

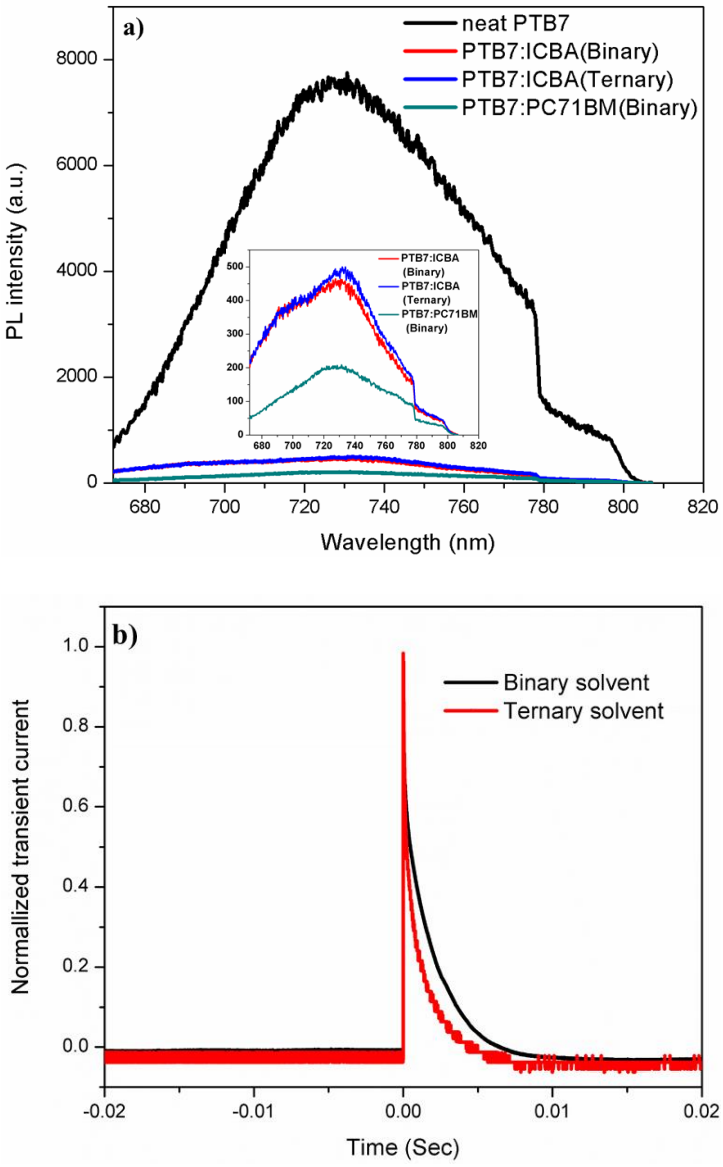

Figure 4.4: (a) PL spectra of neat PTB7, PTB7: ICBA (Binary solvent), PTB7: ICBA (Ternary solvent), PTB7: PC71BM (Binary solvent), the inset image is zoomed-in PL spectra of blend films. Note that the discontinuity at 780nm results from the limitation of the range of the detector of the system used. (b) Transient photocurrent as function of time for samples prepared by binary solvent and ternary solvent.

3.2. Cascade charge transfer effect. By inserting a C_{60} layer on top of the PTB7:ICBA layer, a cascade charge transfer effect occurs at the interface between the PTB7:ICBA active layer and C_{60}. The cascade of charge transfer across energy levels of the materials and electrons

(holes) transporting mechanisms are depicted in Figure 4.5. The LUMO (HOMO) energy levels of PTB7, ICBA and C_{60} are -3.3 eV (-5.15 eV), -3.7 eV (-5.8 eV) and -4.1 eV (-6.2 eV), respectively.[30] At the interface between the active material and the C_{60} layer, the charge transfer occurring in the blend PSCs can follow three different paths: PTB7 to ICBA, ICBA to C_{60} and PTB7 to C_{60}, which represents more pathways than that in the PTB7:ICBA system without a C_{60} layer, where charge transfer can take place only from PTB7 to ICBA. In addition, a driving force is provided by the electron transfer from ICBA to C_{60} due to the energy difference between their LUMO levels, which further promotes charge transfer between PTB7 and ICBA.

As LiF is a barrier layer which allows only the electron transport, the direct contact between the active materials and back metal electrode is prevented. Due to its insulating properties, the LiF layer should be extremely thin to allow the electron transport to the electrode. However, the very thin layer affects its role as a barrier layer. Due to the superior electron conducting properties of C_{60}, the electron transport to the metal electrode is effectively enhanced with the C_{60} layer even when an extremely thin LiF layer is used.[45-47] Thus, the C_{60} layer reduces the recombination of charges at the interface by readily transferring the electrons form the active layer to C_{60} due to favorable energetics. By prohibiting exciton recombination at the interface, the devices with a C_{60} layer show higher current density compared with the ones without a C_{60} layer as revealed in Figure 4.2(a).

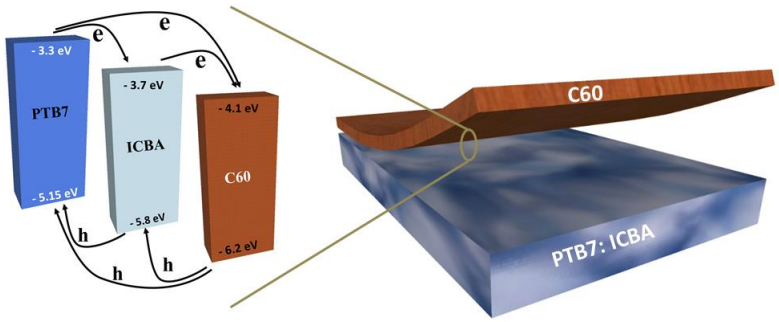

Figure 4.5 Schematic representation of the cascade charge transfer at the interface between active material and C60.

Table 4.2 Photovoltaic results of different blend materials

Processing Solvent	V_{oc} (V)	J_{sc} (mA cm-2)	Calculated J_{sc} (mA cm^{-2})	FF (%)	PCE (%)
PTB7:ICBA (Binary solvent)	0.91 (0.91)	12.79 (12.93)	12.71	45 (46)	5.24 (5.48)
PTB7:ICBA (Ternary solvent)	0.93 (0.93)	13.91 (14.23)	13.84	49 (50)	6.34 (6.61)
PTB7:$PC_{71}BM$ (Binary solvent)	0.76 (0.76)	16.32 (16.56)	16.28	55 (56)	6.86 (7.02)

4.5 Advanced AFM study

4.5.1 Surface morphology study using PFM and MSAFM

To understand the role of ternary solvents on the morphology of the active layer and get some insight into the active layer's nanoscale structures and properties contributing to the improvement in PCE and V_{oc} observed, an advance nanoscale analysis of the layers is carried out

with Pulsed-Force-Mode AFM (PFM-AFM)[48-51] and Mode-Synthesizing AFM (MSAFM).[52-56] PFM is emerging as a versatile tool to probe the stiffness and adhesive properties of materials at the nanoscale.[51] A PFM measurement consists of modulating the tip-sample distance periodically to apply a gradual force onto the sample, spanning from the attractive to the repulsive regime.[49] The stiffness measurements showed little variations, as expected given the similar properties of the two organic materials. However, in the respective adhesion AFM images (Figure 4.6a and 4.6d), changes in the adhesive properties of the materials could clearly be observed in the inset of Figure 4.6b and 4.6e. The maps presented in Figure 4.6b and 4.6e correspond to the k-means cluster analysis performed on the force curve dataset acquired at each pixel of the image, with a filter applied to carry out the comparison of the adhesive properties only (since stiffness changes could not be resolved). From the analysis of the force curves, it could be established that the blue regions correspond to the ICBA-rich regions, while the red regions correspond to PTB7-rich. The maps are obtained with identical parameters including identical cantilever, force applied and range of the displacement. By direct comparison of the maps presented in Figure 4.6, the active layer obtained with the ternary solvents mixture clearly exhibits different structure and surface adhesion properties.

To further confirm the domain sizes, another advanced AFM technique is employed, called MSAFM. MSAFM is a multi-frequency technique based on acoustic actuation of both the tip (f_p) and the sample (f_s), which has recently been used for nanoscale imaging of various material properties,[55] including detection of density variations in soft matter.[57] The multi-frequency actuation is performed by piezo-ceramic components placed at the basis of the cantilever and underneath the sample, at frequencies f_p and f_s, respectively.[53, 55] The nonlinear tip-sample interaction acts as a medium for wave mixing, in which sum and difference frequency generation

take place. The amplitude and phase of the difference mode synthesized in the system can then be used to differentiate the mechanical characteristics of the sample.[55] The MSAFM images obtained on the active layer prepared by binary and ternary solvent mixtures are presented in Figure 4.6c and 4.6f, respectively. Interestingly, a high contrast between PTB7 and ICBA regions could be resolved. This constitutes a significant advantage over other nanoscale characterization techniques used to date, for which low contrast between the polymers drastically hinders the direct identification of the phases forming the active layer. For reference, amplitude and phase images obtained by tapping mode imaging are presented in Figure 4.8. The sensitivity of MSAFM makes it possible to observe the change of polymer networks and fullerene domain of the active layer relative to the solvent mixture being used.

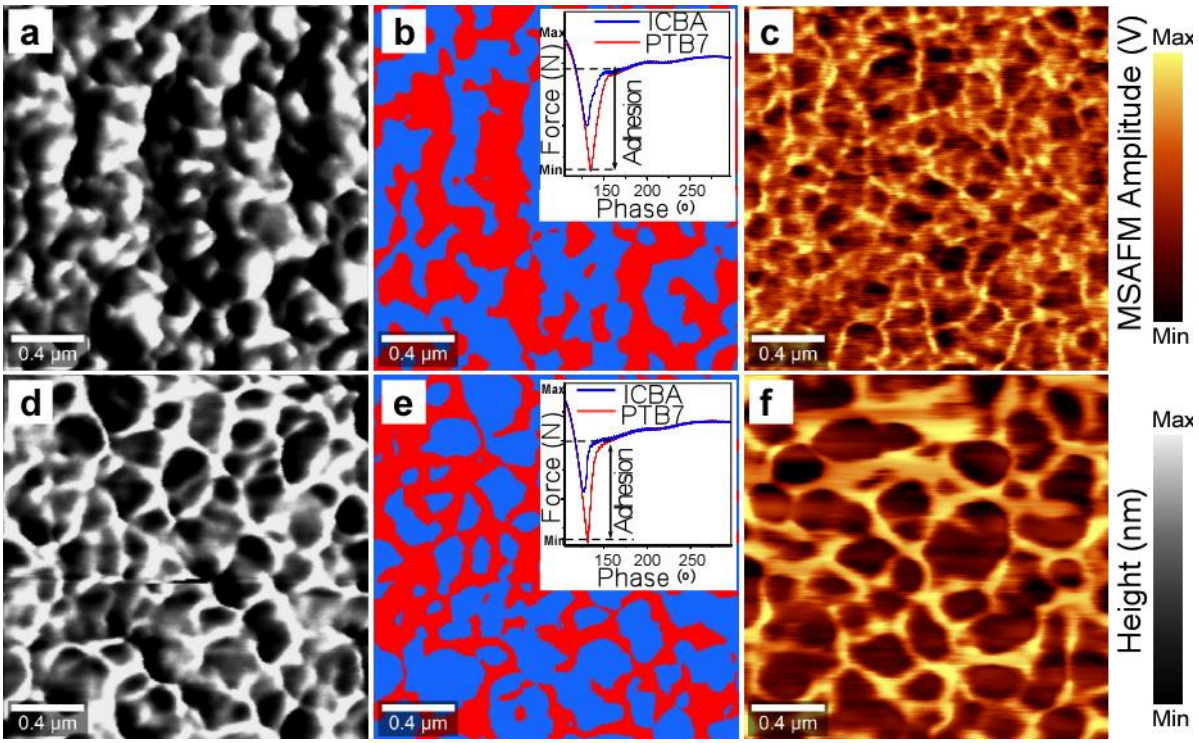

Figure 4.6 Nanoscale investigation of the physical properties of PTB7:ICBA blend films. The active layer is processed by binary mixture of solvents-CB/DIO (97:3, v/v) (a-c) and a ternary mixture of solvents-CB/CF/DIO (78:19:3, v/v/v) (d-f). (a,d) AFM adhesion image, (b,e)

cluster analysis images of the adhesion response of the sample and (c,f) multi-frequency MSAFM images. Image sizes are 2um ×2um.

Although the size of the ICBA regions obtained after binary solvent mixture preparation is smaller (Figure 4.6c), which could be increase the surface area for exciton processes that promote the performance of the device, the interstitial regions appear to be highly discontinuous and the lack of pathways for charges to reach the electrodes seem detrimental to the performance of the device. In addition, in the MSAFM images, the gradients of color with the ICBA-rich grains suggest a variation of concentration in the phase itself, which has been shown to play a significant role in PSC performance. According to Figure 4.6f the ternary solvent conditions lead to better defined ICBA regions with a distribution of grain sizes in the nanometer range and a more homogeneous contrast of the dark regions suggests a more even concentration of the ICBA phase. In addition, the sample showed continuous and connected polymer (PTB7) pathways, as seen in the bright yellow color in Figure 4.6f. Interestingly, although the regions corresponding to PTB7 and ICBA are comparable with PFM and MSAFM for the ternary solvent mixture as seen in Figure 4.6e and 4.6f, this is not the case for the images obtained on the blend resulting from the binary solvent mixture (Figure 4.6 b and c). For future studies, one should note that the sensitivity of MSAFM offer a new avenue to differentiate the nanoscale morphology of the multi-components blend of the active layer, which was not possible using other traditional AFM methods. Adhesion measurements can be hampered by the level of water absorption on the sample, hence adhesion measurements only constitute a superficial comparison of the surface properties of the two blends. Nevertheless, the PFM results suggest that the interfacial properties between the active layer of PTB7:ICBA and adjacent layers (PEDOT:PSS and C_{60}) will likely change depending on the solvent conditions. Using MSAFM, although only with limited

qualitative comparison (quantitative measurements are beyond the scope of this study), a clear difference in structure and behavior of the active layers could be confirmed. It is noted that in this study, the properties and structure of the ternary sample lead to enhanced performances of the device, suggesting that purer phases and better defined separations will contribute to better performance. To confirm this hypothesis, additional measurements on a hybrid nanoscale-infrared imaging platform are underway.

According to these observations, exciton dissociation efficiency seems to be favored in blends for which the nanometer-scale phase separated polymer phase is continuous and the fullerene phase is pure and homogeneous. Meanwhile, rough interfaces will enhance interfacial area which will contribute to exciton dissociation efficiency as well.[58] As a result, PTB7:ICBA blend film in the ternary solvent exhibits a higher J_{sc} and FF.

4.5.2 Conductive AFM studies

Current density is an important factor to determine the performance of PSCs. From Table 4.1, it is clear that the main factor contributing to the difference of PCEs between the active layers obtained from binary and ternary solvents mixtures is the current density. As charge separation and charge transport determine the J_{sc}, c-AFM is used to study the local J_{sc} variations across the sample. C-AFM consists of two electrodes on each side of the active material, which is similar to electrode configuration in the device of the solar cell architecture: the ITO layer is used to apply the DC bias to the active layer, while the cantilever tip is used as the ground. In this configuration, it is possible to measure the regions of current flowing between the sample and the conductive tip. Sensitivity in the pA range is necessary to detect a current while performing the measurements. In order to reduce the oxidation of the samples, the microscope is placed in a glove bag, which is first purged and then filled with nitrogen gas prior to imaging. In

addition to applying a bias onto the sample, an optical module for side-illumination of the sample in the vicinity of the tip is designed. A 100mA/cm^2 light intensity is used for the measurement. The current levels are recorded with light off (black curves) and light on (gray and red curves) in Figure 4.7 to compare the response of binary and ternary materials to illumination in the visible range.[59-62]

In Figure 4.7a and 4.7b, a direct comparison of the sample response for lights on/off for binary (Figure 4.7a) and ternary (Figure 4.7b) is presented in the form of histograms representing the level of currents measured across a 10□m × 10□m area. The nanoscale current measurements of the PTB7:ICBA layer obtained with the binary (Figure 4.7a,c) and ternary (Figure 4.7b,d) solvents confirm the trend measured in the real devices. An increase in the mean current value (c,d) and of the overall current distribution (a,b) across the layers can be clearly seen for both systems. Interestingly, with the light on, largest currents could be observed at the PTB7:ICBA interface in both cases. The large increase of current measured in the ternary solvent with the lights on can be explained by the better defined regions, as determined in the MSAFM measurements, with the electron transport distance from polymer to fullerene that likely reduce the possibility of charge recombination to further improve J_{sc}.

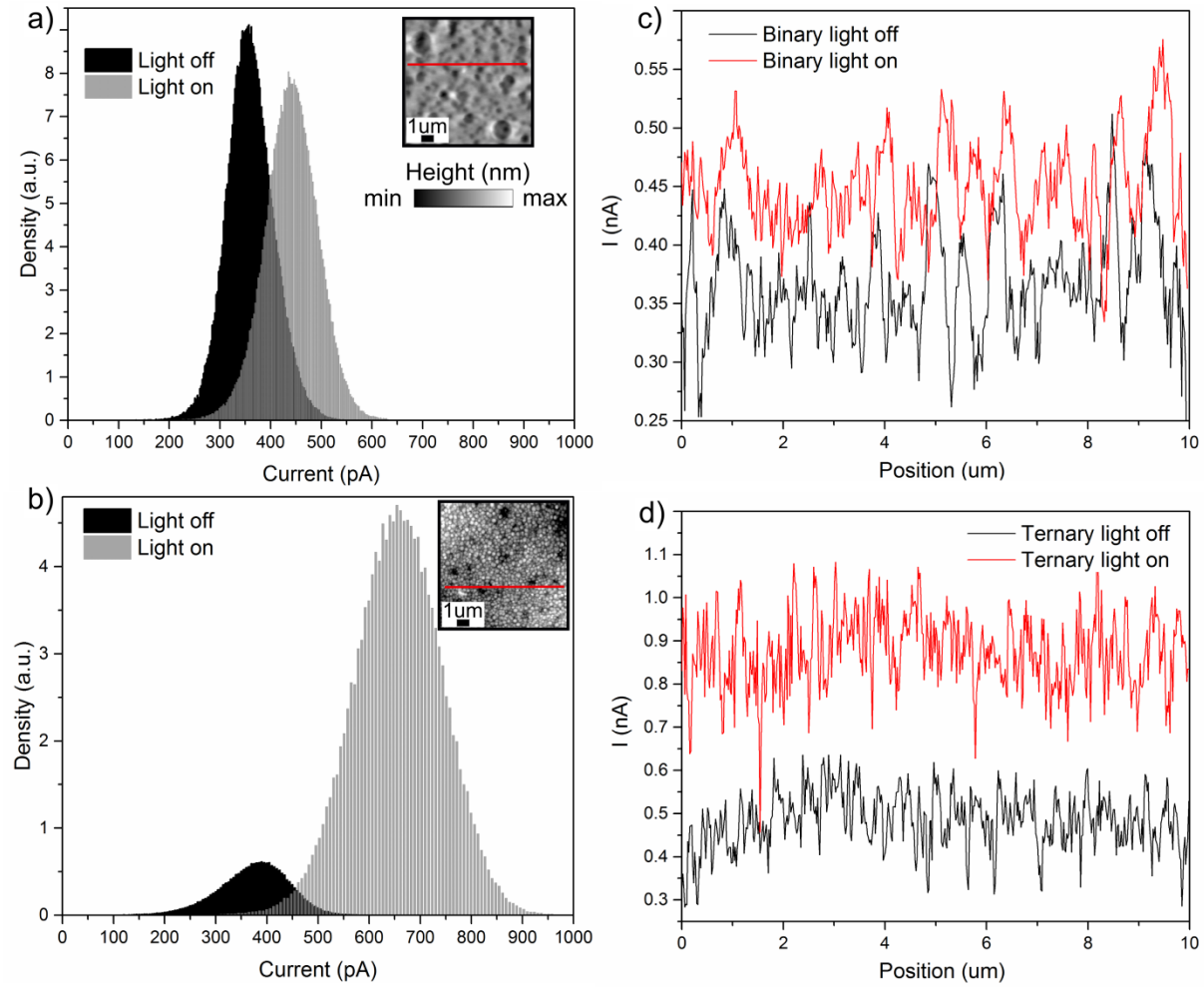

Figure 4.7 Comparison of the current levels measured by cAFM with and without illumination. The active layers of the PSCs prepared with binary mixture of solvents-CB/DIO (97:3, v/v) (a,c) and a ternary mixture of solvents-CB/CF/DIO (78:19:3, v/v/v) (b,d). Respective histograms of current values (a,b) are presented, together with a line profile of the variation in current across the sample as a result of white light illumination (c,d). All measurements are acquired using a DC bias of -4V on the sample.

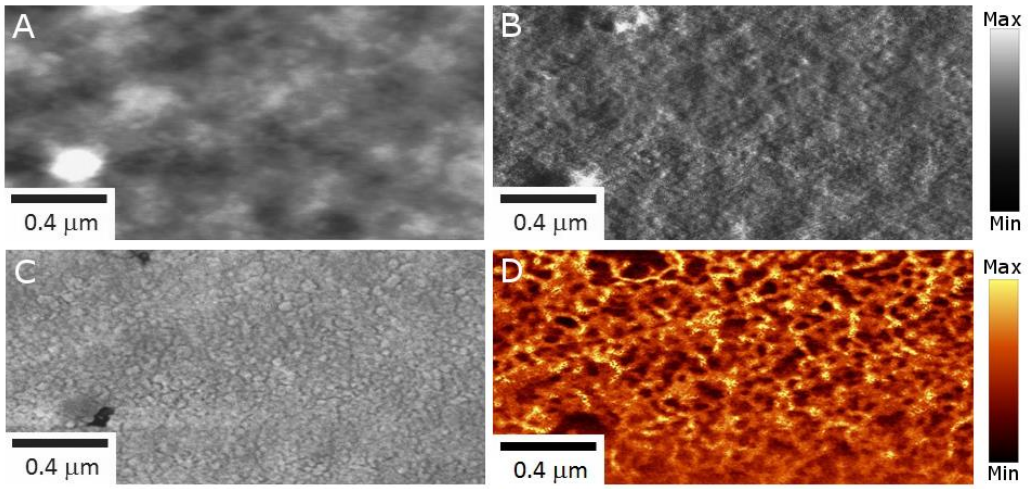

Figure 4.8 (A) Topography (B) Amplitude (C) Phase images obtained by tapping mode imaging. (D) MSAFM Amplitude map of the same region.

In order to demonstrate the benefit of these high V_{oc} devices, we connected four devices in series to efficiently power a green-light emission diode. (Figure S1 and Video S1). Compared with those low V_{oc} solar cells, high V_{oc} PSCs require fewer devices to illuminate light emission diode.

Figure 4.9 A green-light emission diode was lightened up by the PSC (four in series).

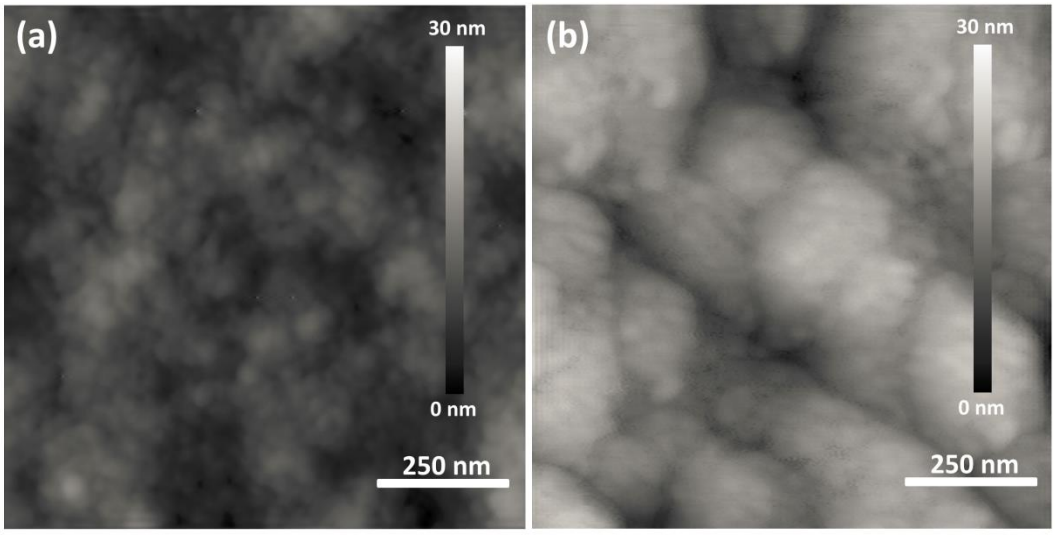

Figure 4.10 Topography AFM images of PTB7: ICBA films prepared by binary solvent (a) without C_{60} buffer layer and (b) with 10 nm C_{60} buffer layer.

To better understand the affection of the grain size and distribution to the whole film, reflectance and absorption of the whole devices for binary solvents (CB/DIO) and ternary solvents (CB/CF/DIO) are introduced in Figure 4.11 and 4.12, respectively. From the figures, we can conclude that the ternary solvent (CB/CF/DIO) give us lower reflectance and higher absorption, which means more light is absorbed by the film fabricated from the ternary solvent. These is the reason why the sample prepared with ternary solvent (CB/CF/DIO) shows better power conversion efficiency.

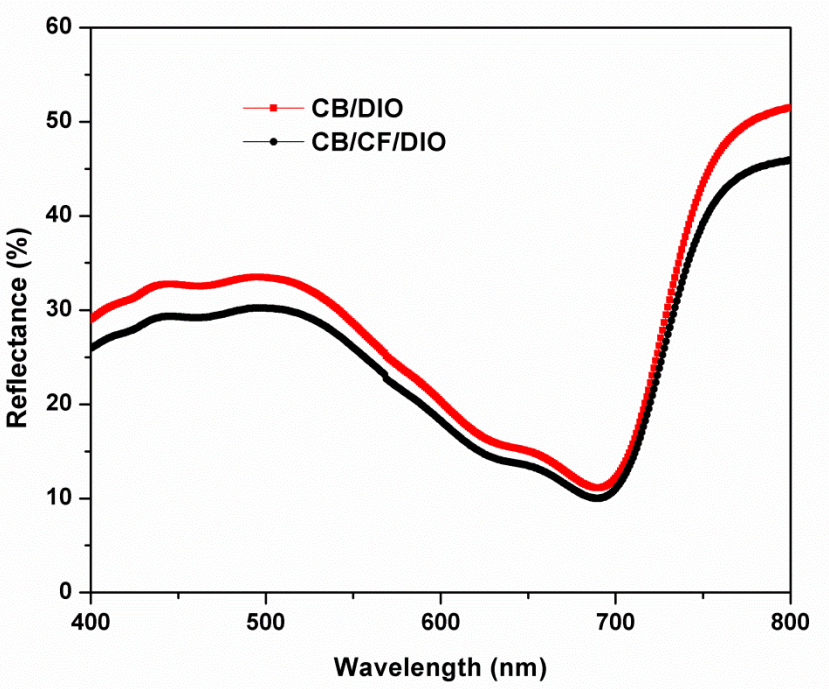

Figure 4.11 Reflectance of the whole devices for binary solvents (CB/DIO) and ternary solvents (CB/CF/DIO).

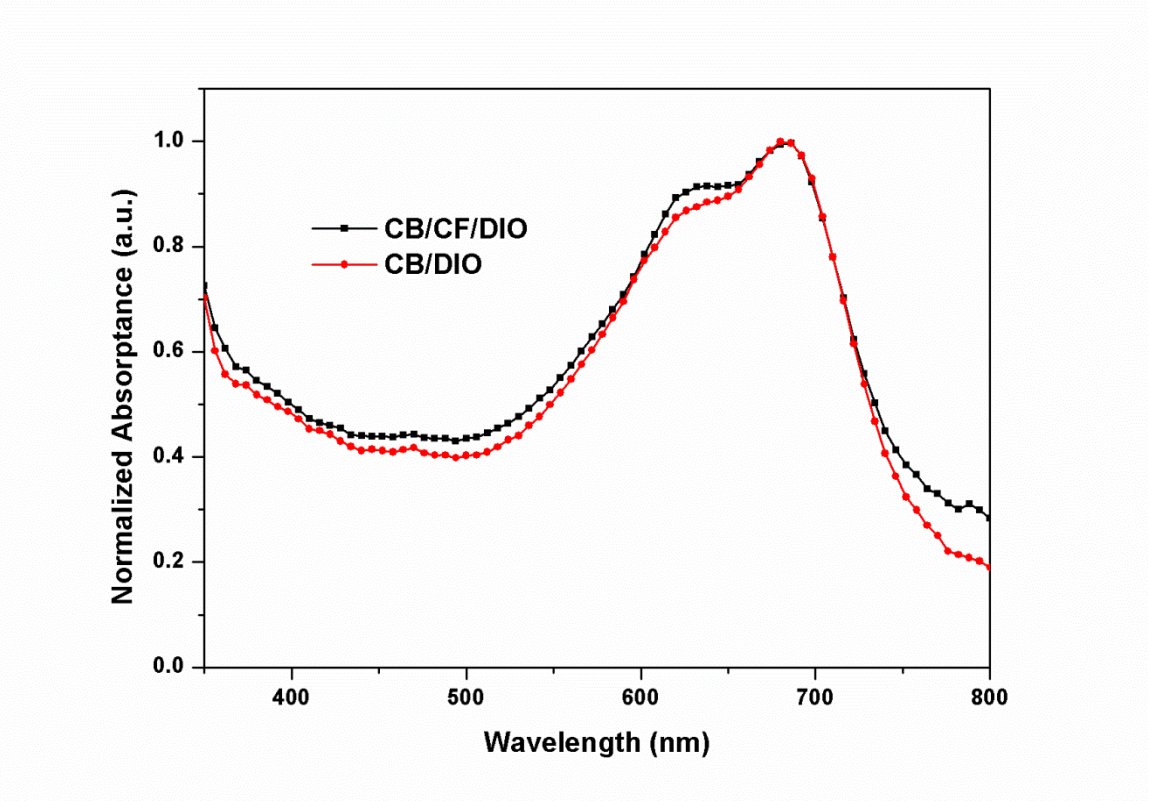

Figure 4.12 Normalized absorption spectra of the PTB7: ICBA thin film processed by binary solvent (CB/DIO) and ternary solvent (CB/CF/DIO).

4.6 Conclusion

In summary, our study demonstrates the influence of solvents used in the preparation of the polymer blend for the active layer on the subsequent performance of the devices. Furthermore, here two new nanoscale characterization techniques are presented, namely PFM and MSAFM, which offer new insights into the properties of the mixed organic blend at the nanoscale. In particular, MSAFM shows high sensitivity for direct visualization of the donor-acceptor phases in the active layer of the PSCs. Although in their infancy, the results obtained

with the two techniques suggest that fundamental understanding of the mechanisms at play in polymer blends for PSCs can be facilitated with advanced nanoscale tools. This is further confirmed with our c-AFM study, which highlighted higher conductivity at the interface between donor and acceptor phases.

The surface morphology of PTB7:ICBA blend film has been successfully optimized by the introduction of ternary solvent CB/CF/DIO, and provides a path to improve the performance of PSCs. Meanwhile, an additional C_{60} layer is used between PTB7:ICBA blends and LiF to obtain ternary effect at the interface for better J_{sc} and PCE. Due to the lower HOMO energy level of C_{60}, LiF and C_{60} works as hole-blocking layers to effectively reduce the recombination. Compared with ternary blend system, this ternary solvent combined with the additional C_{60} layer provides a promising path for high performance without sacrificing the V_{oc}. Even without additional architecture design (like tandem cells), our champion cell achieved PCE as high as 7.5%, which is one of the highest values for the PSC using PTB7 polymer with high V_{oc} more than 0.9 V. Our results demonstrate that use of ternary solvent and additional C_{60} layer is an effective way towards PCSs with high performance and high V_{oc} for utilizing other applications as well. The details unveiled at the nanoscale initiate a deeper understanding of the mechanisms at play to increase the PCE of PSCs.

4.7 References

1. L.-M. Chen, Z. Hong, G. Li and Y. Yang, *Adv. Mater.*, 2009, **21**, 1434-1449.
2. M. S. Dresselhaus and I. L. Thomas, *Nature*, 2001, **414**, 332-337.
3. D. Mühlbacher, M. Scharber, M. Morana, Z. Zhu, D. Waller, R. Gaudiana and C. Brabec, *Adv. Mater.*, 2006, **18**, 2884-2889.

4. C. J. Brabec, *Sol. Energy Mater. Sol. Cells*, 2004, **83**, 273-292.

5. B. A. Gregg and M. C. Hanna, *J. Appl. Phys.*, 2003, **93**, 3605-3614.

6. K. L. Chopra, P. D. Paulson and V. Dutta, *Prog. Photovoltaics*, 2004, **12**, 69-92.

7. M. A. Green, K. Emery, Y. Hishikawa, W. Warta and E. D. Dunlop, *Prog. Photovoltaics*, 2012, **20**, 12-20.

8. N. Blouin, A. Michaud and M. Leclerc, *Adv. Mater.*, 2007, **19**, 2295-2300.

9. Y. Liang, Z. Xu, J. Xia, S.-T. Tsai, Y. Wu, G. Li, C. Ray and L. Yu, *Adv. Mater.*, 2010, **22**, E135-E138.

10. T. Xu and L. Yu, *Mater. Today*, 2014, **17**, 11-15.

11. L. Ye, S. Zhang, W. Ma, B. Fan, X. Guo, Y. Huang, H. Ade and J. Hou, *Adv. Mater.*, 2012, **24**, 6335-6341.

12. Y. Min Nam, J. Huh and W. Ho Jo, *Sol. Energy Mater. Sol. Cells*, 2010, **94**, 1118-1124.

13. F. Zhang, K. G. Jespersen, C. Björström, M. Svensson, M. R. Andersson, V. Sundström, K. Magnusson, E. Moons, A. Yartsev and O. Inganäs, *Adv. Funct. Mater.*, 2006, **16**, 667-674.

14. S. Guo, B. Cao, W. Wang, J.-F. Moulin and P. Müller-Buschbaum, *ACS Appl. Mater. Interfaces*, 2015, **7**, 4641-4649.

15. J. Jo, J.-R. Pouliot, D. Wynands, S. D. Collins, J. Y. Kim, T. L. Nguyen, H. Y. Woo, Y. Sun, M. Leclerc and A. J. Heeger, *Adv. Mater.*, 2013, **25**, 4783-4788.

16. A. P. Yuen, A.-M. Hor, J. S. Preston, R. Klenkler, N. M. Bamsey and R. O. Loutfy, *Appl. Phys. Lett.*, 2011, **98**, 173301.

17. J. You, L. Dou, K. Yoshimura, T. Kato, K. Ohya, T. Moriarty, K. Emery, C.-C. Chen, J. Gao and G. Li, *Nat. Commun.*, 2013, **4**, 1446.

18. Y. Gu, C. Wang, F. Liu, J. Chen, O. E. Dyck, G. Duscher and T. P. Russell, *Energy Environ Sci.*, 2014, **7**, 3782-3790.

19. R. A. Street, D. Davies, P. P. Khlyabich, B. Burkhart and B. C. Thompson, *J. Am. Chem. Soc.*, 2013, **135**, 986-989.

20. P. P. Khlyabich, A. E. Rudenko, R. A. Street and B. C. Thompson, *ACS Appl. Mater. Interfaces*, 2014, **6**, 9913-9919.

21. Q. An, F. Zhang, L. Li, J. Wang, J. Zhang, L. Zhou and W. Tang, *ACS Appl. Mater. Interfaces*, 2014, **6**, 6537-6544.

22. Q. An, F. Zhang, J. Zhang, W. Tang, Z. Deng and B. Hu, *Energy Environ Sci.*, 2016, DOI: 10.1039/C5EE02641E.

23. Q. An, F. Zhang, Q. Sun, J. Wang, L. Li, J. Zhang, W. Tang and Z. Deng, *J. Mater. Chem. A*, 2015, **3**, 16653-16662.

24. W. Ma, J. R. Tumbleston, L. Ye, C. Wang, J. Hou and H. Ade, *Adv. Mater.*, 2014, **26**, 4234-4241.

25. T. Ameri, P. Khoram, J. Min and C. J. Brabec, *Adv. Mater.*, 2013, **25**, 4245-4266.

26. M. Koppe, H.-J. Egelhaaf, G. Dennler, M. C. Scharber, C. J. Brabec, P. Schilinsky and C. N. Hoth, *Adv. Funct. Mater.*, 2010, **20**, 338-346.

27. H. Li, Z.-G. Zhang, Y. Li and J. Wang, *Appl. Phys. Lett.*, 2012, **101**, 163302.

28. X. Wang, Z.-G. Zhang, W. Tang, S. Shen, G. Liu, D. Chi, Y. Li and J. Wang, *Macromol. Chem. Phys.*, 2013, **214**, 1081-1088.

29. J.-H. Huang, Y.-S. Hsiao, E. Richard, C.-C. Chen, P. Chen, G. Li, C.-W. Chu and Y. Yang, *Appl. Phys. Lett.*, 2013, **103**, 043304.

30. P. Cheng, Y. Li and X. Zhan, *Energy Environ Sci.*, 2014, **7**, 2005-2011.

31. S. Guo, J. Ning, V. Körstgens, Y. Yao, E. M. Herzig, S. V. Roth and P. Müller-Buschbaum, *Adv. Energy Mater.*, 2015, **5**, 1401315

32. C. Gu, Y. Chen, Z. Zhang, S. Xue, S. Sun, C. Zhong, H. Zhang, Y. Lv, F. Li, F. Huang and Y. Ma, *Adv. Energy Mater.*, 2014, **4**, 1301771.

33. G. Wang, T. Jiu, G. Tang, J. Li, P. Li, X. Song, F. Lu and J. Fang, *ACS Sustainable Chem. Eng.*, 2014, **2**, 1331-1337.

34. M. C. Scharber, D. Mühlbacher, M. Koppe, P. Denk, C. Waldauf, A. J. Heeger and C. J. Brabec, *Adv. Mater.*, 2006, **18**, 789-794.

35. Y. He, H.-Y. Chen, J. Hou and Y. Li, *J. Am. Chem. Soc.*, 2010, **132**, 1377-1382.

36. B. Qi, Q. Zhou and J. Wang, *Sci. Rep.*, 2015, **5**, 11363.

37. P. P. Khlyabich, B. Burkhart and B. C. Thompson, *J. Am. Chem. Soc.*, 2011, **133**, 14534-14537.

38. H. Choi, J.-P. Lee, S.-J. Ko, J.-W. Jung, H. Park, S. Yoo, O. Park, J.-R. Jeong, S. Park and J. Y. Kim, *Nano Lett.*, 2013, **13**, 2204-2208.

39. A. K. Ko Kyaw, D. Gehrig, J. Zhang, Y. Huang, G. C. Bazan, F. Laquai and T.-Q. Nguyen, *J. Mater. Chem. A*, 2015, **3**, 1530-1539.

40. E. T. Hoke, K. Vandewal, J. A. Bartelt, W. R. Mateker, J. D. Douglas, R. Noriega, K. R. Graham, J. M. J. Fréchet, A. Salleo and M. D. McGehee, *Adv. Energy Mater.*, 2013, **3**, 220-230.

41. D. Wang, F. Zhang, L. Li, J. Yu, J. Wang, Q. An and W. Tang, *RSC Adv.*, 2014, **4**, 48724-48733.

42. X. Liu, Q. Li, Y. Li, X. Gong, S.-J. Su and Y. Cao, *J. Mater. Chem. A*, 2014, **2**, 4004-4013.

43. R. Dierick, B. Capon, H. Damm, S. Flamee, P. Arickx, E. Bruneel, D. Van Genechten, M. Van Bael, A. Hardy, C. Detavernier and Z. Hens, *J. Mater. Chem. C*, 2014, **2**, 178-183.

44. Q. Sun, F. Zhang, Q. An, L. Li, J. Wang, M. Zhang, W. Wang, F. Teng and J. Zhang, *Org. Electron.*, 2015, **24**, 30-36.

45. S. Cho, K.-D. Kim, J. Heo, J. Y. Lee, G. Cha, B. Y. Seo, Y. D. Kim, Y. S. Kim, S.-y. Choi and D. C. Lim, *Sci. Rep.*, 2014, **4**, 4306-4311.

46. B. Paci, A. Generosi, V. Rossi Albertini, P. Perfetti and R. de Bettignies, *J. Phys. Chem. C*, 2009, **113**, 19740-19747.

47. H. J. Park, H. Kim, J. Y. Lee, T. Lee and L. J. Guo, *Energy Environ Sci.*, 2013, **6**, 2203-2210.

48. K. J. Kwak, H. Kudo and M. Fujihira, *Ultramicroscopy*, 2003, **97**, 249-255.

49. C. A. Rezende, L.-T. Lee and F. Galembeck, *Langmuir*, 2009, **25**, 9938-9946.

50. A. Rosa-Zeiser, E. Weilandt, S. Hild and O. Marti, *Meas. Sci. Technol.*, 1997, **8**, 1333.

51. O. Soppera, M. Feuillade, C. Croutxé-Barghorn and C. Carré, *Prog. Solid State Chem.*, 2005, **33**, 233-242.

52. G. S. Shekhawat and V. P. Dravid, *Science*, 2005, **310**, 89-92.

53. L. Tetard, A. Passian, S. Eslami, N. Jalili, R. H. Farahi and T. Thundat, *Phys. Rev. Lett.*, 2011, **106**, 180801.

54. G. Shekhawat, A. Srivastava, S. Avasthy and V. Dravid, *Appl. Phys. Lett.*, 2009, **95**, 263101.

55. L. Tetard, A. Passian and T. Thundat, *Nat. Nanotechnol.*, 2010, **5**, 105-109.

56. L. Tetard, A. Passian, K. T. Venmar, R. M. Lynch, B. H. Voy, G. Shekhawat, V. P. Dravid and T. Thundat, *Nat. Nanotechnol.*, 2008, **3**, 501-505.

57. P. Vitry, E. Bourillot, C. Plassard, Y. Lacroute, E. Calkins, L. Tetard and E. Lesniewska, *Nano Res.*, 2015, **8**, 2199-2205.

58. J. H. Lee, D. W. Kim, H. Jang, J. K. Choi, J. Geng, J. W. Jung, S. C. Yoon and H. T. Jung, *Small*, 2009, **5**, 2139-2143.

59. A. Alexeev, J. Loos and M. M. Koetse, *Ultramicroscopy*, 2006, **106**, 191-199.

60. L. S. C. Pingree, B. A. MacLeod and D. S. Ginger, *J. Phys. Chem. C*, 2008, **112**, 7922-7927.

61. D. C. Coffey, O. G. Reid, D. B. Rodovsky, G. P. Bartholomew and D. S. Ginger, *Nano Lett.*, 2007, **7**, 738-744.

62. O. G. Reid, K. Munechika and D. S. Ginger, *Nano Lett.*, 2008, **8**, 1602-1609.

5 FABRICATION OF SEMITRANSPARENT SOLAR CELLS WITH SOLVENT ASSISTED METHOD

5.1 Introduction

Organometal trihalide perovskite solar cells (PSCs) have become a promising solar cell technology due to its high efficiency and low fabrication cost.[1, 2] The competitiveness of the perovskite solar cell is attributed to its outstanding opto-electronic properties, such as wide band gap,[3-5] long charge diffusion length,[6-8] and high absorption coefficients.[9-11] Compared with crystalline Si solar cells, the simple and easy solution-based processing of the perovskite solar cell offers considerable promise for the future renewable energy generation. Due to these exceptional characteristics, perovskite solar cells have attracted significant attention over the past few years.[12-15] Despite being an emerging type of solar cells, perovskite solar cells have reached a power conversion efficiency (PCE) of over 20% due to the rapid and continuous progress in research thus making it a competitive alternative to the traditional silicon solar cell.[13, 16, 17] Along with considerable efforts dedicated to pursuing high PCE devices, semitransparent perovskite solar cells also have received a great deal of attention not only because of their high PCE and transmittance but also for its potential applications in tandem solar cells,[18] building integrated photovoltaics[19, 20] and smart glasses.[21] Since these applications require high voltage to operate, semitransparent perovskite solar cells with high output voltage (~1V) are favored: more cells connected in series would be required if low V_{oc} silicon solar cells(~0.5-0.6V) were used.[22]

Recently, considerable effort has been dedicated in developing semitransparent perovskite solar cells with high PCE by inserting an extra buffer layer in addition to an existing electron transport/hole transport layer in between the respective electrodes and the active

perovskite layer. The typical materials used are zinc oxide (ZnO), molybdenum trioxide (MoO_3) or poly(3,4-ethylenedioxythiophene):poly(styrenesulfonate) (PEDOT:PSS) in addition to the existing electron transport layer, phenyl-C61-butyric acid methyl ester (PCBM), and hole transport layer, 2,2',7,7'-Tetrakis-(N,N-di-4-methoxyphenylamino)-9,9'-spirobifluorene (Spiro-OMeTAD). This additional layer is used to enhance the transmittance and contact between the electrode and the buffer layer. With a 170nm thick active layer, Guo et al. reported a PCE of 8.49% for semitransparent mixed halide ($CH_3NH_3PbI_{3-x}Cl_x$) semitransparent solar cell composed of indium tin oxide (ITO)/PEDOT:PSS/$MAPbI_{3-x}Cl_x$/PCBM/ZnO /Ag nanowire.[23] In this work, an additional thin layer of ZnO was introduced for two reasons: (1) to keep good ohmic contact between PCBM and AgNWs, and (2) to protect the perovskite layer from the damage due to the presence of AgNWs. Gaspera et al. also reported semitransparent solar cells comprised of F-doped tin oxide (FTO)/TiO_x/$CH_3NH_3PbI_3$ (150nm)/Spiro-OMeTAD/MoO_3-Au-MoO_3 exhibiting an efficiency of 9.3% with an average visible transmittance (AVT) of 16%.[24] Compared with our architecture ITO/PEDOT:PSS/CH3NH3PbI3/PCBM/Au, it requires high temperature (500^oC) treatment and complicated processing for TiOx layer as well as two additional layers of MoO_3. You et al. reported semitransparent solar cells with a structure: FTO/TiO_x/$CH_3NH_3PbI_3$/Spiro-OMeTAD/PEDOT:PSS/Graphene,[25] in which D-sorbitol doped PEDOT:PSS was used as an adhesion layer to laminate the spiro-OMeTAD and graphene electrode. With this adhesion layer, the PCE of the device with 170nm thick perovskite layer improved from 4% to 7.5%.

All of the above devices require multiple electron or hole transport layers to reach PEDOT:PSS layers, the performance of the device dropped more than 1% from the original value. It is important to note that these additional buffer layers require more steps, longer time

and higher cost to fabricate the semitransparent devices. Recently, Huang et al. reported a conventional fabrication procedure in which a conformal layer of PCBM is formed on the surface of perovskite layer.[26, 27] However, the thermal annealing requires 60 minutes or more for infiltration into any considerable depth of the perovskite layer, and required an additional C_{60} layer to reach maximum PCE of about 12%.

In the present work, we discuss the development of a perovskite-PCBM hybrid material obtained by a simple PCBM-assisted growth technique, which resulted in the production of high performance semitransparent perovskite solar cells. We also show that this method eliminates the need of an extra buffer layer. The novel PCBM-assisted perovskite growth technique involves spin coating of perovskite precursor solution on a substrate, immediately followed by exposing the wet film to chlorobenzene based PCBM solution to induce crystallization. We present evidence that PCBM-assisted growth results in perovskite-PCBM hybrid crystal structure at the grain boundaries by PCBM diffusion while the film grows in size [28]. Moreover, devices fabricated by this method required no additional buffer layer on the electron collector electrode to accomplish high performance. Film consisting of a perovskite-PCBM hybrid solid of about 150nm thickness was successfully built into a semitransparent planar heterojunction solar cell yielding a superior PCE of 9.1%, compared to a PCE of 4.03% for a control cell. The control sample was prepared using a conventional growth method. Overall, we show that this facile method enables the fabrication of highly efficient semitransparent perovskite solar cells with a simpler and shorter fabrication procedure.

5.2 Device Fabrication

The patterned ITO substrates were subsequently cleaned in an ultrasonicator with DI water, acetone and isopropanol for 15 minutes each. On the cleaned ITO substrate, a thin layer of

PEDOT:PSS (Clevios™ P VP AI 4083) was deposited by spin coating and annealed at 120 °C for 30 minutes. Subsequently, the substrates were transferred into glove box for the deposition of perovskite absorber and PCBM layers. Perovskite precursor solution was prepared by mixing CH_3NH_3I and $PbAc_2$ in anhydrous N,N-Dimethylformamide at a 3:1 molar ratio with a final concentration of ~40 wt%. For a layer-by-layer device, the filtered perovskite precursor was spin-casted at 3000 rpm for 45 seconds. The crystallization of the perovskite was performed by annealing the as-deposited film at 100°C for 10 minutes. The thickness of the $CH_3NH_3PbI_3$ layer is approximately 150–200 nm. PCBM solution was then spin-casted onto the $CH_3NH_3PbI_3$ layer at 1000 rpm for 45 seconds. For the PCBM-assisted process, PCBM solution was spin-casted while perovskite precursor was spreading. The resulting film was annealed at 100°C for 15min. Finally, a 10 nm thick Au was deposited on the PCBM through a shadow mask under a vacuum of 10^{-6} torr.

5.3 Characterization methods

For the evaluation of the PSCs performance, a solar simulator with a 300 W Xenon lamp and AM1.5G global filter were used. The light intensity, 100 mW cm^{-2} was calibrated using a silicon photovoltaic reference cell (Newport, 91150V). Current-voltage characteristics were measured with a Keithley 2635A source measurement unit. The EQE spectra were measured using a Newport model QE-PV-SI coupled with a lock-in amplifier and a calibrated silicon photodetector. During device characterization, a shadow mask with an opening of 7.5 mm^2 was used. Cross sections of the samples were prepared using a FIB (FEI 200 TEM) operating at 30 kV accelerating voltage. Surface morphologies were characterized by means of scanning electron microscope (SEM, ZEISS Ultra 55) and transmission electron microscope (TEM, TECNAIF30)

equipped with an energy-dispersive *electron energy loss spectroscopy*. Transmittance of semitransparent devices was measured using an UV-VIS-NIR spectrometer (Cary 300 Bio). PL measurements were performed on a Witec alpha 300 RA confocal Raman system equipped with a Zeiss 20X objective and a 600 lines/mm grating. The samples were excited with 532 nm laser light ($\sim$ 10 μW) in ambient air environment at room temperature. The measurements were collected for an integration time of 0.05 s. A Raman map of 10,000 spectra from each sample was acquired, and the spectra were averaged to present a representative signature. For transient photocurrent measurement, a 532 nm Q-switched, frequency doubled Nd:YAG laser (Minilite I, Continuum) was used to generate 5ns pulse. Light pulses with energy less than 1uJ were used. Photocurrent was measured using a Tektronix MDO3012 Oscilloscope via a Keithley Model SC-9 low noise Coaxial cable connected to the two electrodes.

5.4 Schematic of solvent assisted method

The schematic illustration of the PCBM-assisted growth process and layer-by-layer growth process for perovskite-PCBM layer is shown in Figure 5.1. The PCBM-assisted growth method for preparing the perovskite-PCBM hybrid layer is illustrated in process 2 of Figure 5.1. The substrate consists of a thin layer of PEDOT:PSS on top of ITO glass. A DMF-based perovskite solution was then spin-coated on top of the PEDOT:PSS layer at 3000rpm. After a few seconds, PCBM dissolved in chlorobenzene (CB) was quickly added to the above film. This PCBM-assisted growth improves the performance due to: (1) the CB solvent quickly decreases the solubility of $CH_3NH_3PbI_3$ in the mixed solvent and promotes rapid nucleation and growth of the crystals [29] and (2) at the interface of the perovskite and PCBM, an intimate mixing of perovskite and PCBM takes place to form a hybrid structure, which reduces the recombination loss and

promotes electron extraction [28]. In contrast, for a layer-by-layer method where PCBM layer is spin coated after perovskite growth is completed and heat treated, a less transparent and poorer quality perovskite film is generated. Moreover, compared to Xu et al. who fabricated a heterojunction hybrid perovskite-PCBM layer by mixing perovskite and PCBM solution together with TiOx and Spiro-OMeTAD layer [28], our PCBM-assisted method provides a continuous PCBM layer on top of the hybrid perovskite-PCBM layer, which significantly simplifies the fabrication process. In both methods, the addition of PCBM is followed by annealing at 100^{o}C for 15 min to remove the residual solvent and to promote any further crystallization. Therefore, the new PCBM-assisted method saves one annealing step, compared to that necessary for a layer-by-layer preparation method.

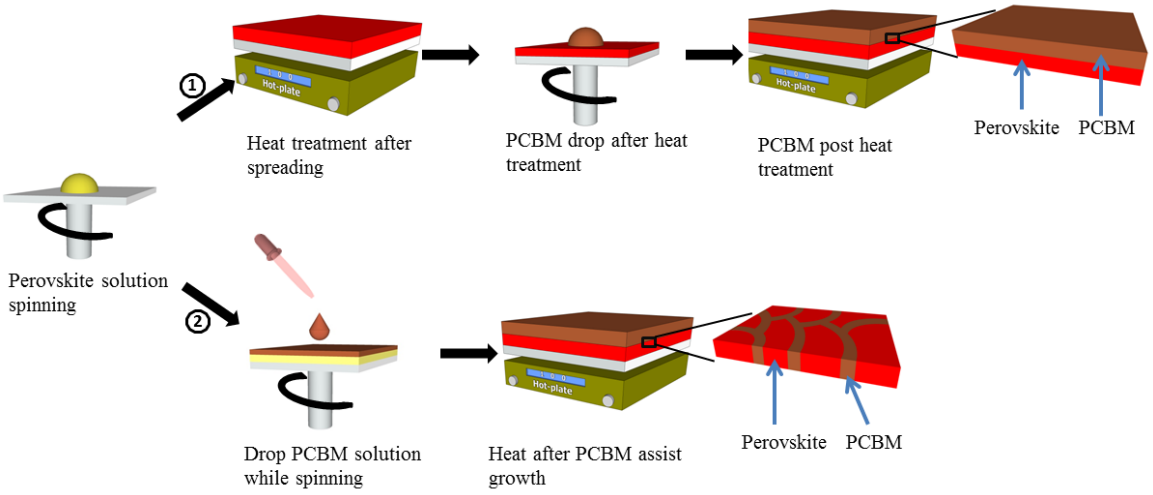

Figure 5.1 Scheme of the process flow for devices (1) layer-by-layer growth resulting in perovskite and PCBM separate layers and (2) PCBM-assisted growth resulting in perovskite-PCBM hybrid structure.

5.5 Photovoltaic properties

Figure 5.2a illustrates the schematic of the device structure fabricated by the PCBM-assisted growth method and Figure 5.2b is its cross-sectional transmission electron microscopy (TEM) image. For fabricating a solar cell, a uniform and continuous $CH_3NH_3PbI_3$ layer (~150 nm thick) was first deposited on top of an ITO/glass substrate pre-coated with a dense and thin p-type PEDOT:PSS film of thickness about 20 nm. A PCBM layer of thickness about 50nm was prepared for hybrid layer formation and for building electron transport layer (ETL). The cell was completed by depositing a thin Au top electrode by thermal evaporation. Using this PCBM-assisted growth process, a perovskite-PCBM hybrid material was formed at the interface between the perovskite and the fullerene layer, as schematically represented in the zoomed-in region of Figure 5.2a. In this hybrid layer, PCBM is diffusing throughout the film at the perovskite grain boundaries, which in turn is an efficient electrically networked structure for electron transport. To monitor the quality of the perovskite films, we recorded the SEM image of an as-grown perovskite film (Figure 5.2c). Since there is always a thin layer of PCBM on top of the perovskite layer in a PCBM-assisted growth process, it is difficult to see the perovskite crystal grains from the top of the film. In order to assess the quality and grain size of the perovskite film formed by PCBM-assisted growth process with respect to that made by a layer-by-layer process, we inspect top view SEM image (Figure 5.3) of the CB assisted growth film prepared under the same experimental conditions since PCBM dissolved CB is always used for this growth. The film obtained by PCBM-assisted method exhibits considerably large crystal grains (~1μm) and almost full coverage on the substrate with absence of pinholes. The X-ray pattern of the as-prepared perovskite film on ITO/PEDOT:PSS is shown in Figure 5.6.

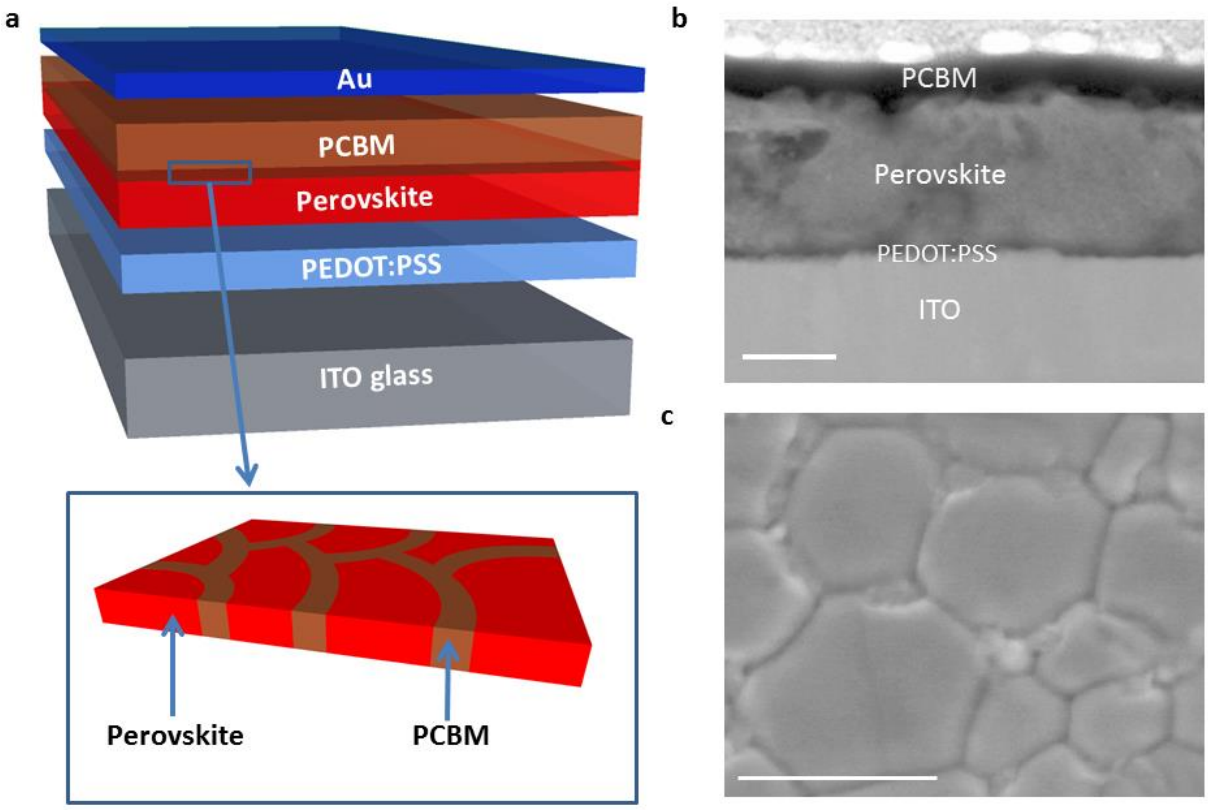

Figure 5.2 Perovskite solar cell structure. (a) Schematic architecture of the perovskite solar cell; the zoomed-in schematic represents the hybrid material formed. (b) TEM cross-section view of the perovskite solar cell by PCBM-assisted growth process. Scale bar: 1um.

Figure 5.4a and 5.4b shows the J-V and external quantum efficiency (EQE) plots of semitransparent perovskite solar cell with PCBM-assisted growth. Devices resulting from the PCBM-assisted growth procedure exhibited substantial improvement of the short circuit current density (J_{sc}) from 10 to 14.33 mA cm^{-2} along with higher fill factor (FF) and V_{oc}. We infer that the superior performances are due to the effective enhancement of charge transport and the reduction of charge recombination by the introduction of hybrid PCBM-perovskite materials. The enhancement of charge transport is due to better conductivity near grain boundaries because

of the hybrid material formation. It provides a continuous network of electron transport medium (PCBM), which extends all the way to the electron collector (top Au) electrode. Figure 5.4a inset shows the evolution of our best PCE as a function of average visible transmittance (AVT) for the PCBM-assisted growth devices and a comparison with other recently reported semitransparent PSCs.[24, 30, 31] In Figure 5.4c, the AVT (calculated between 370nm and 740nm) shows increased transmission for the devices prepared by PCBM-assisted growth compared to one obtained with layer-by-layer growth. Moreover, the devices with PCBM-assisted growth show an average PCE of 8.6 ± 0.5% (AVT = 18%), while the layer-by-layer growth devices exhibit only 4.03± 0.3% average PCE (AVT = 13.3%) for a 150nm thick perovskite active layer. This process is highly repeatable with average efficiencies of 8.6% across 20 devices. Therefore, a better transmittance and power conversion efficiency is obtained by PCBM-assisted growth method. A small hysteresis of PCBM-assisted growth devices is observed in the Figure 5.4d, where there is only a fill factor (FF) difference of 2% between forward and reverse scan. Meanwhile, a large hysteresis of layer-by-layer growth devices was observed , as shown in Figure 5.5.

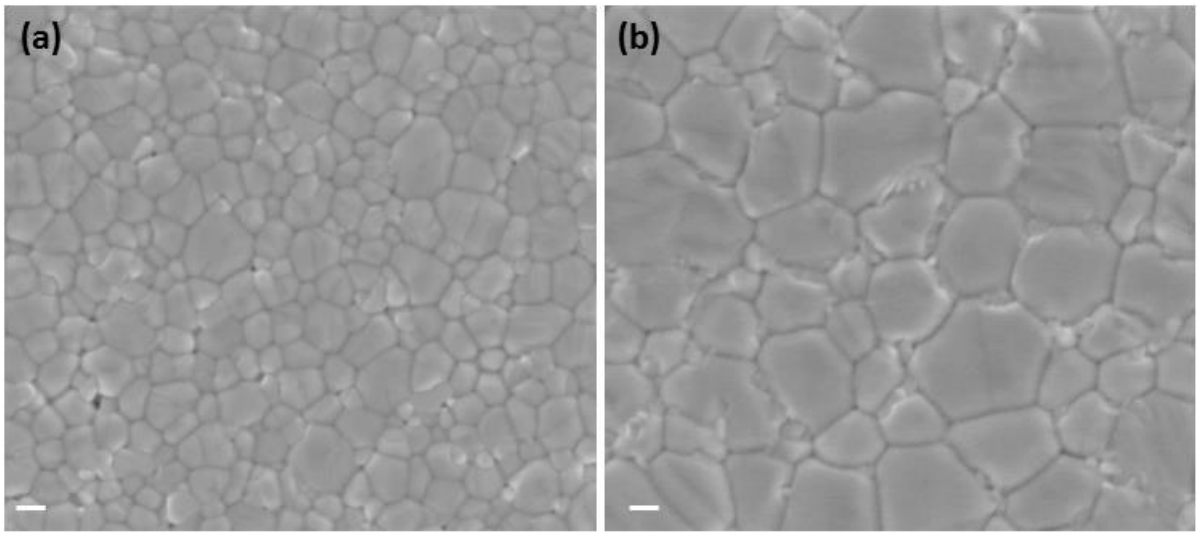

Figure 5.3 SEM images of the surface morphology of the CH3NH3PbI3 films prepared by (a) conventional growth method and (b) CB assisted growth method. Scale bar: 200nm.

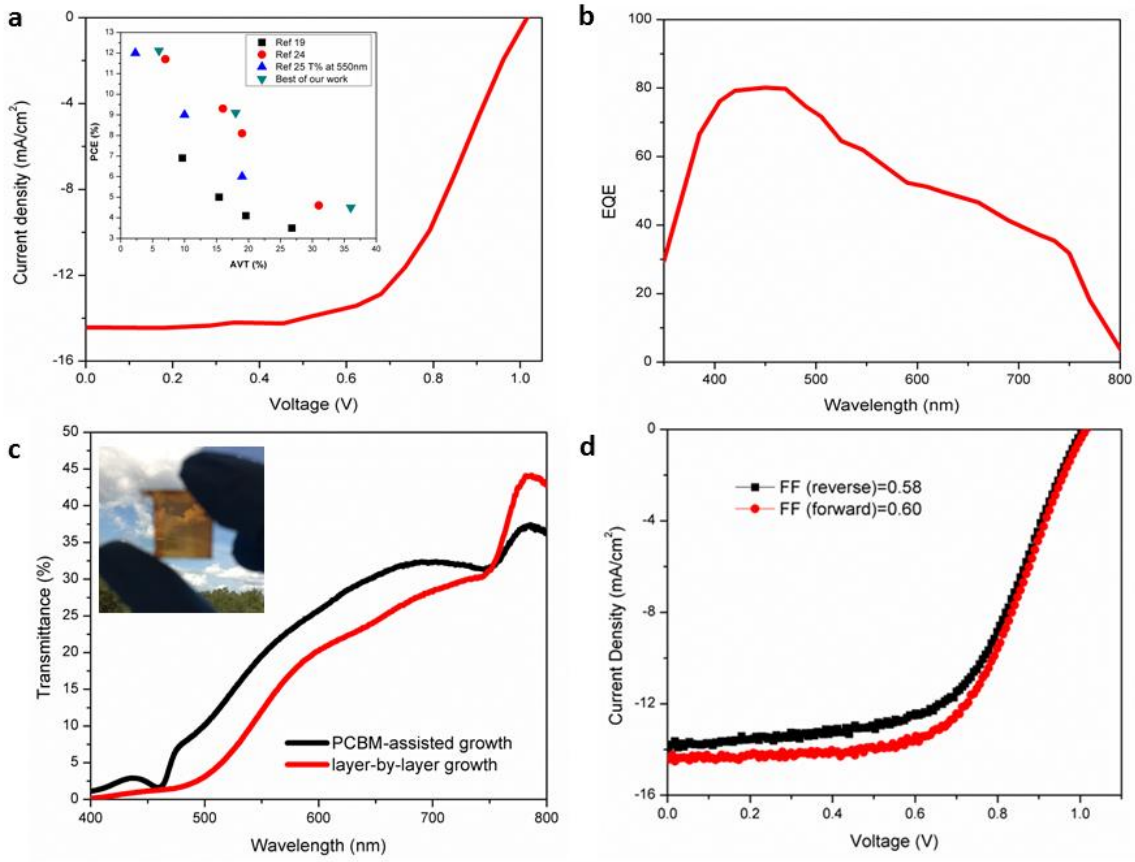

Figure 5.4 Characterization of PSCs. (a) Current-Voltage characteristics; inset is plot of PCE as a function of AVT (370nm-740nm) and comparison with other semitransparent PSCs (b) EQE of PSCs with PCBM-assisted growth (c) transmittance spectra of complete PSCs with PCBM-assisted growth and layer-by-layer growth. (d) J-V curve of PCBM-assisted growth device with small hysteresis.

The photovoltaic parameters of the devices using perovskite films prepared by different methods like layer-by-layer growth semitransparent device, chlorobenzene-assisted growth and PCBM-assisted growth are shown in Table 5.1. If a thin (10nm) Au layer is deposited directly on top of the devices fabricated by layer-by-layer growth method, a very poor performance of 4.03% was obtained. The perovskite crystalline grains with sizes up to 300nm shown are obtained using this method [32].

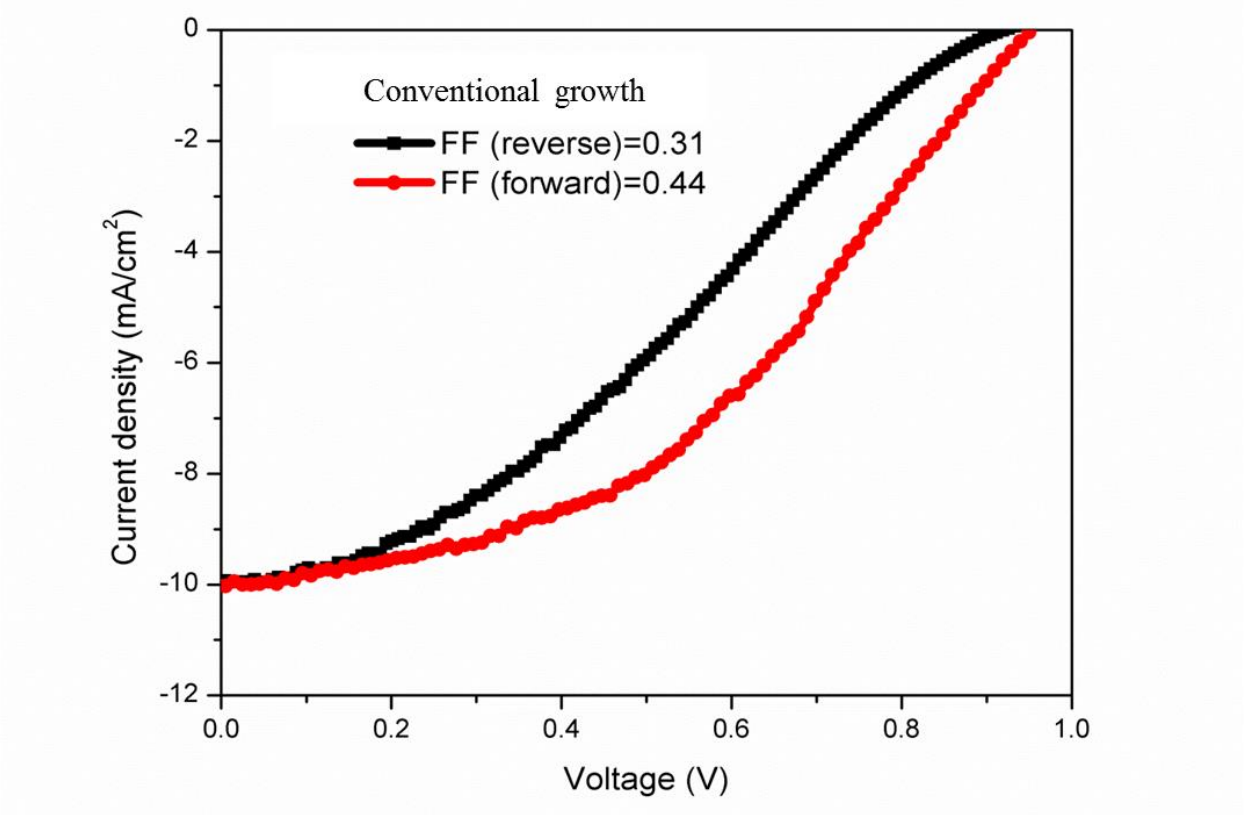

Figure 5.5 J-V curve of conventional growth device with large hysteresis.

Devices with CB-assisted growth exhibited much improved performance, which may result from good perovskite films consisting of large crystalline grains with sizes up to one micron. SEM images of the surface morphology of the $CH_3NH_3PbI_3$ films prepared by both layer-by-layer growth method and CB-assisted growth method are shown. Devices prepared with the CB-assisted growth method showed better charge separation and transport, which resulted in a better PCE of 6.85%. Furthermore, when the PCBM-assisted growth technique was used, further improvement of the performance was accomplished. Devices fabricated by the PCBM-assisted growth method yields the best performance with the help of larger crystal grain and the perovskite-PCBM hybrid structure. However, when a thicker Au layer was coated on top of this

perovskite-PCBM hybrid structure, a higher efficiency was achieved due to the improved conductivity and efficient charge collection by the thick continuous coating. In addition, better light utilization is achieved by the reabsorption of the reflected light from the thicker Au electrode layer. The performance of the devices using a thick, opaque Au cathode (70 nm) exceeds 12%. It is to be noted that the thickness of the perovskite layer for all the devices was about 150nm.

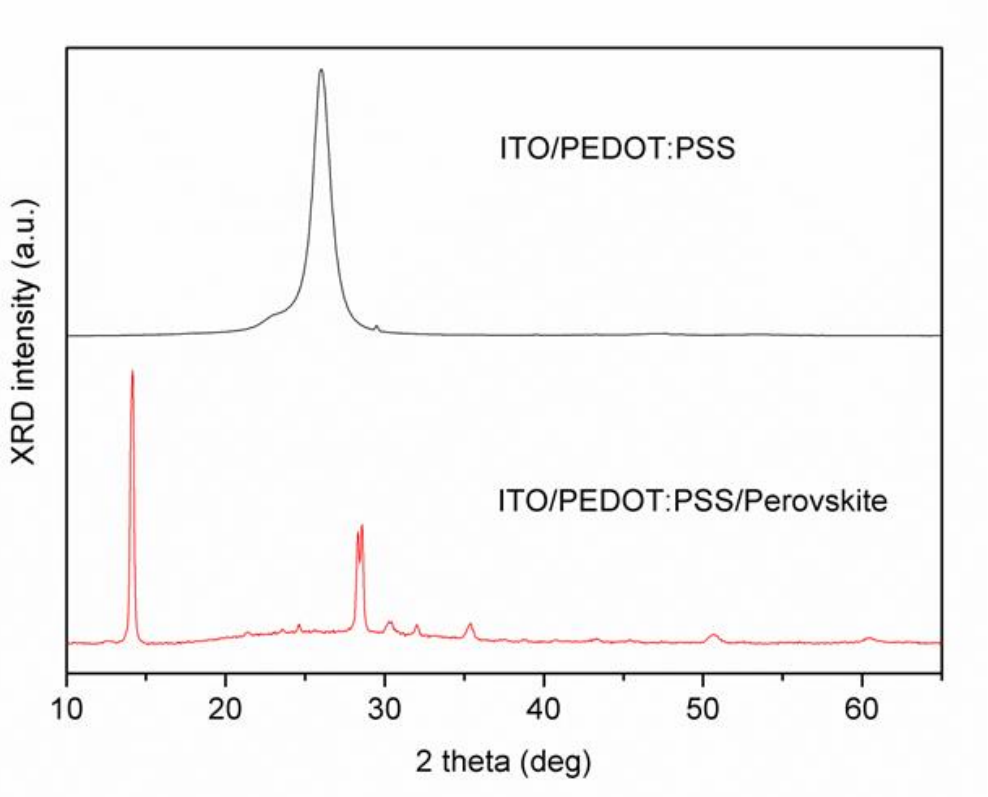

Figure 5.6 XRD pattern of the perovskite crystals grown on PEDOT:PSS/ITO (red line), with blank sample of the PEDOT:PSS coated ITO substrate for comparison (black line).

Table 5.1 Device parameters for solar cells using perovskite films prepared by conventional layer-by-layer growth, chlorobenzene-assisted growth and PCBM-assisted growth.

Cell	V_{oc} (V)	J_{sc} (mA cm-2)	FF (%)	PCE (%)	AVT (%)
Conventional layer-by-layer growth with high AVT	0.929	9.906	43.78	4.03	14
CB-assisted growth with high AVT	0.958	13.43	53.28	6.85	15
PCBM-assisted growth with high AVT	1.017	14.56	61.42	9.10	18
PCBM-assisted growth with low AVT	1.017	17.50	68.10	12.12	3

5.6 Characterization of perovskite-PCBM hybrid structure

To further investigate the film formation process using PCBM-assisted growth, delay times of 2s, 6s and 8s before dropping PCBM in CB solution onto the perovskite precursor solution were tested to study the effect of processing on the resulting device efficiency and transmission. Figure 5.7 shows the J-V and transmittance plots of a semitransparent solar cell using the PCBM-assisted growth for different delay times. The average photovoltaic parameters are shown in Table 5.2.

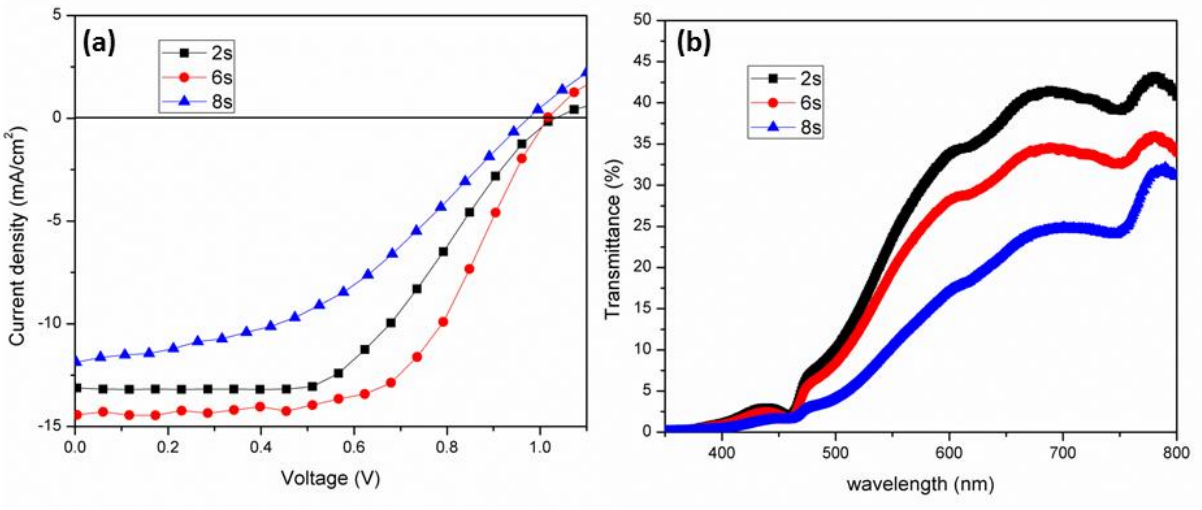

Figure 5.7 (a) Current-Voltage characteristics and (b) Transmittance spectra of complete perovskite solar cells prepared by adding PCBM solution at different delay times (2s, 6s, 8s) from the start of the spin-coating process.

Table 5.2 Device parameters for solar cells using perovskite films prepared by adding PCBM solution at different delay times (2s, 6s, 8s) from the start of the spin-coating process.

Cell	V_{oc} (V)	J_{sc} (mA cm-2)	FF (%)	PCE (%)
PCBM drop at 2s	1.031	12.82	53.94	7.13
PCBM drop at 6s	1.017	14.33	60.44	8.81
PCBM drop at 8s	0.976	11.87	42.64	5.0

The best performance of devices was found to be for 6s delay time between the beginning of spinning perovskite layer. The outstanding performance is obtained by applying the CB

solution of PCBM onto the spinning wet films of perovskite at the time of nucleation and crystal growth. A current density of 12.82 mA/cm^2 and a PCE of 7.13% were obtained when a delay time of 2s was used. This comparatively lower current density and PCE may be explained by the insufficient time to remove the excess precursor solution, which is a dominant process for high nucleation density. Applying PCBM in chlorobenzene at this stage may result in only a partial surface coverage since perovskite solution is not supersaturated.[33] Nonetheless, high open circuit voltage of 1.031 V was obtained since more PCBM was mixed with perovskite during this stage. To demonstrate the application of this high V_{oc} device, the voltage output from two of these devices connected in series (in Fig. 5.8a and 5.8b) were adequate to power a red-light emitting diode (LED).

In order to demonstrate the benefits of high V_{oc} perovskite solar cells, we connected two devices in series to efficiently power a red-light emitting diode (LED; operating voltage-1.7V). Figure 5.8 shows the lighting of LED, before (5.8a) and after (5.8b) connecting the perovskite solar cell. This is to demonstrate that high V_{oc} PSCs require fewer devices compared with low V_{oc} solar cells to illuminate LED.

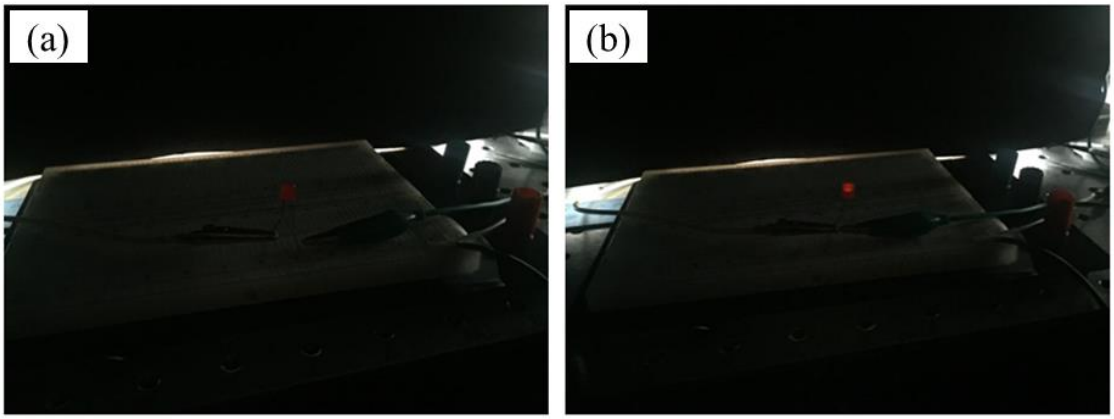

Figure 5.8 It shows the red LED light before (5a) and after (5b) connecting the perovskite solar cell.

Table 5.3 Summary of opaque PSC performances with 100nm thick Au electrode.

Cell	V_{oc} (V)	J_{sc} (mA cm-2)	FF (%)	PCE (%)
Conventional growth	0.930	14.98	55.14	7.68
CB-assisted growth	0.958	16.46	61.86	9.75
PCBM-assisted growth	1.017	17.82	70.12	12.71

With a 6s delay, evaporation of the residual solvent promotes concentration of the perovskite solution and introduction of PCBM results in the formation of a dense and uniform perovskite film and hybrid perovskite-PCBM structure.[29] However, with a 8s delay, the device had considerably lower current density of 11.87 mA/cm^2 and a PCE of 5%, which we attribute to the fact that the perovskite film began to dry and crystallize before the PCBM solution was added. The addition of PCBM in CB at this stage resulted in the formation of perovskite film with grain in the micrometer range, as can be seen in Figure 5.9.

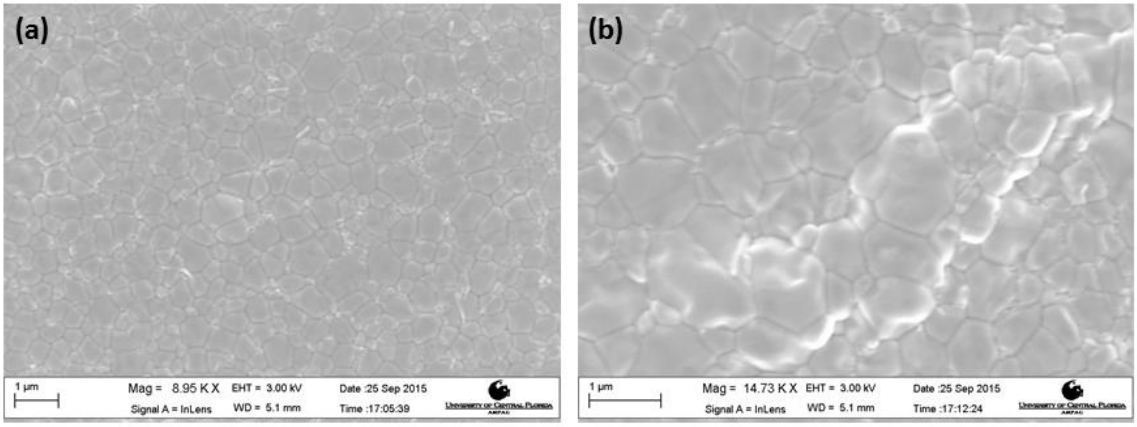

Figure 5.9 SEM images of the surface morphology of the $CH_3NH_3PbI_3$ films prepared by PCBM solution at different delay times from the start of the spin-coating process: (a) 6s; (b) 8s.

To verify the formation of this hybrid structure, we performed TEM in combination with electron energy loss spectroscopy (EELS) on the cross-section of these devices (Figure 5.10). A thin cross-section of the solar cell was prepared by focused ion beam (FIB) for TEM and EELS study. In order to analyze the penetration of PCBM into the perovskite grain boundaries to form the hybrid layer, we selected certain elements which are known to be present in one material, but not in the other. PCBM contains the element oxygen (O) while perovskite does not. Perovskite contains lead (Pb) and iodine (I) elements while PCBM not. For devices fabricated by PCBM-assisted growth method, the elemental mapping in Figure 5.10a shows the presence of O in the perovskite layer. It is to be noted that due to the small thickness of the FIB cut samples, we can see the distribution of O all around instead of just at the grain boundary region. However, the elemental mapping of the PCBM unassisted sample (Figure 5.10b) shows the presence of O only in the top PCBM layer and not in the perovskite layer. The distribution of O in the perovskite layer validates the formation of a hybrid material in perovskite solar cells

fabricated by PCBM-assisted method which is similar to the hybrid material reported by Xu et al.[28]

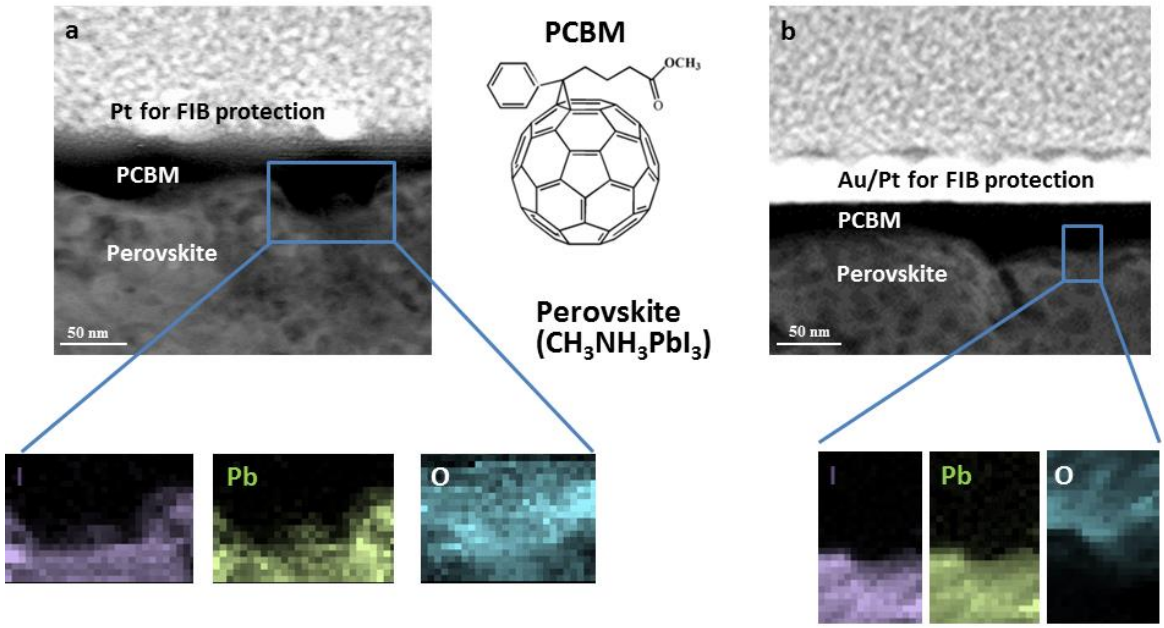

Figure 5.10 TEM cross-sectional image of the device: (a) with PCBM-assisted growth and (b) layer-by-layer growth. EELS mapping clearly shows the elemental distribution of I, Pb, O.

As discussed earlier, while spin-coating the PCBM, the interface between perovskite and PCBM forms the hybrid structure. The additional PCBM layer on top of the perovskite layer eliminates the direct contact between perovskite crystals and top electrode by providing a smooth surface for top electrode deposition (Figure 5.10a). In addition, it helps in filling up the pinholes in perovskite layer. Since bonding of PCBM to defective halides is thermodynamically favoured, it can reduce the possibility of the formation of defects which can act as recombination centres for electrons and holes. However, this hybrid formation may not take place when PCBM is spin coated after annealing in a conventional growth method. To further investigate this hybrid structure formation, we used XPS to compare the carbon and lead content between conventional growth and PCBM-assisted growth films, both post-washed with chlorobenzene solvent to

remove only the top PCBM layer (Figure 5.11c and 5.11d). Therefore, after washing, only PCBM penetrated into perovskite layer (ie. between the perovskite crystals) should be left in the perovskite-PCBM film. A similar approach has been followed by Xu et al. for monitoringcarbon and lead content.[28] Figure 5.11c and 5.11d show C1s and Pb4f XPS spectra of perovskite film by conventional and PCBM-assisted growth respectively. These figures reveal that perovskite-PCBM hybrid film (red) contains more carbon content and less lead content as PCBM exists in between perovskite crystals. Along with small hysteresis in the hybrid perovskite-PCBM device, a significant voltage enhancement (~0.1V) and higher FF were also observed as given in Table 1. Since PCBM can promote electron extraction at the grain boundaries, hybrid perovskite-PCBM forms a continuous network for electron transport, which reduces hysteresis and improve photovoltaic performance.[28] This is further supported by the steady-state photoluminescence (PL) spectra presented in Figure 5.11a. The enhanced PL of the devices fabricated by PCBM-assisted growth indicates that non-radiative decay is significantly suppressed, which should result from the PCBM-perovskite hybrid structure.[34] In order to compare the charge trapping and the role of PCBM in the device, we performed transient photocurrent (TP) measurements where the impulse response of PCBM-assisted growth device and conventional growth devices were recorded. Figure 5.11b shows the TP measurements of two devices. As shown in the plot, the transit time for the electrons is much less for PCBM-assisted growth device. The values of transit time constants are 0.46 μs and 0.26 μs for conventional and PCBM-assisted samples respectively. These results suggest that PCBM-assisted growth device has better charge transfer properties. It is also worth noting that rise time of the photocurrent is slightly slower for PCBM-assisted growth device in contrast to layer by layer growth device. The slower rise time and faster decay time suggests the passivation of deep trap states and introduction of shallow traps due to

introduction of PCBM as discussed by Dr. Xu et al., using density function theory analysis.[28] This confirms the presence of a hybrid Perovskite-PCBM phase which is in tandem with the argument that PCBM penetrates into Perovskite grain boundaries to form a hybrid phase.[26]

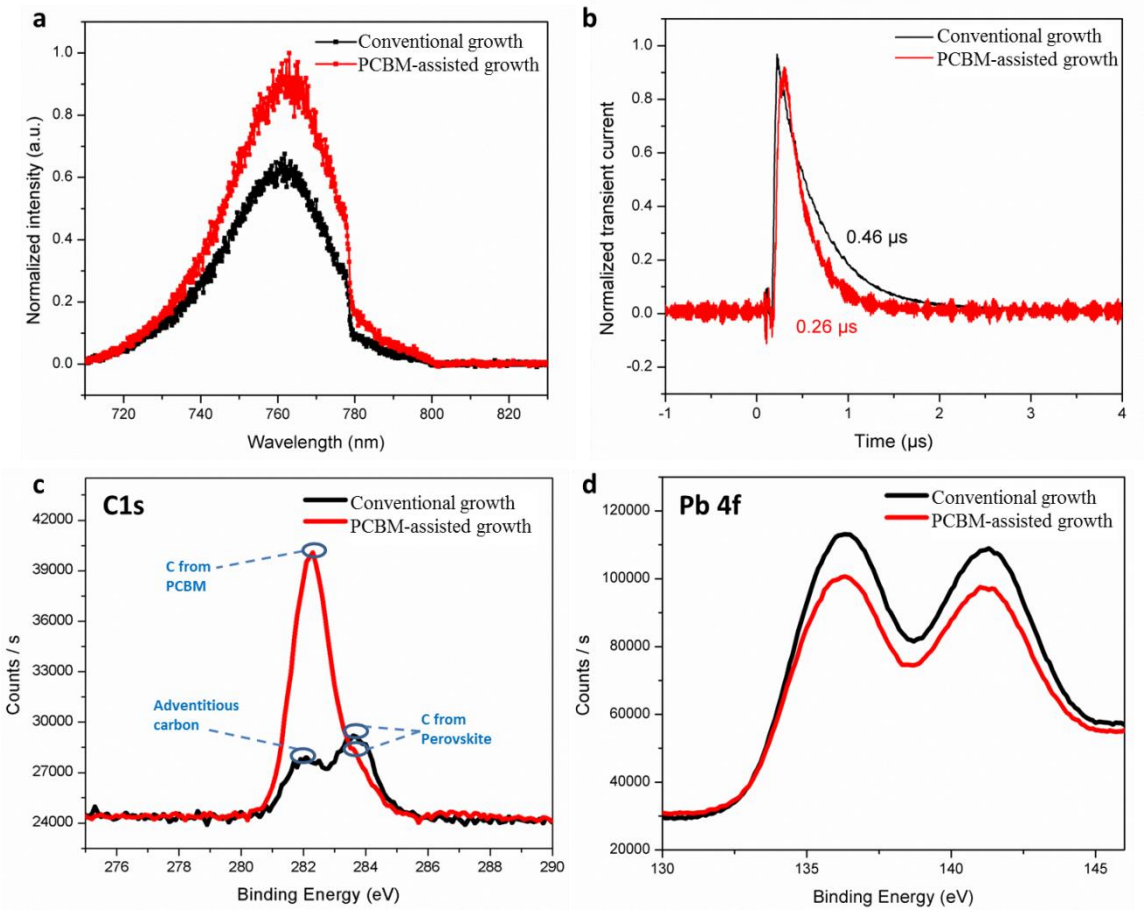

Figure 5.11 (a) Steady-state photoluminescence (PL) spectrum as a function of wavelength showing significantly lower amplitude of the PL peak for the sample prepared by conventional growth. Note that the discontinuity at 780nm results from the limitation of the range of the detector of the system used. (b) Transient photocurrent as function of time for samples prepared by PCBM-assisted growth and conventional growth. (c) A comparison of surface carbon content between conventional growth (black) and PCBM-assisted growth (red) films post-washed with chlorobenzene solvent to remove only the top PCBM layer using XPS. (d) Lead (Pb) element comparison for the same.

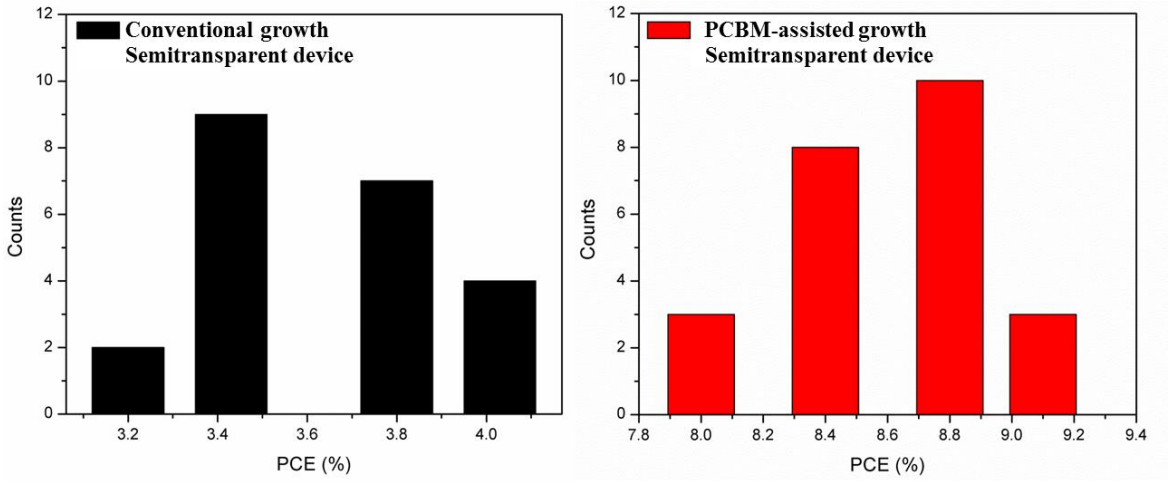

Figure 5.12 Deviation of average power conversion efficiency of more than 20 conventional growth and PCBM assisted growth semitransparent devices

5.7 Conclusion

In conclusion, a fast and low temperature PCBM-assisted growth method has been developed for making high performance semitransparent perovskite solar cells, which allows the penetration of PCBM into perovskite grain boundaries, and provides a hybrid perovskite-PCBM material. This hybrid material enables a continuous network for the electron transport to the overlying PCBM layer and then to the electron collector electrode. EELS elemental mapping reveals the formation of perovskite-PCBM hybrid at the interface of perovskite and PCBM layers. This is confirmed by steady-state photoluminescence (PL) spectra and transient photocurrent (TP) measurements. This method leads to a high PCE of 9.1% and a good AVT of 18%. These results represent a simple method to fabricate high efficiency and high transparency solar cells for building–integrated photovoltaics and other opto-electronic applications.

5.8 References

1. S. Shi, Y. Li, X. Li and H. Wang, *Mater. Horiz.*, 2015, **2**, 378-405.

2. H. J. Snaith, *J. Phys. Chem. Lett.*, 2013, **4**, 3623-3630.

3. F. C. Hanusch, E. Wiesenmayer, E. Mankel, A. Binek, P. Angloher, C. Fraunhofer, N. Giesbrecht, J. M. Feckl, W. Jaegermann, D. Johrendt, T. Bein and P. Docampo, *J. Phys. Chem. Lett.*, 2014, **5**, 2791-2795.

4. G. E. Eperon, S. D. Stranks, C. Menelaou, M. B. Johnston, L. M. Herz and H. J. Snaith, *Energy Environ. Sci.*, 2014, **7**, 982-988.

5. C. Bi, Y. Yuan, Y. Fang and J. Huang, *Adv. Energy Mater.*, 2015, **5**, 1401616.

6. S. D. Stranks, G. E. Eperon, G. Grancini, C. Menelaou, M. J. Alcocer, T. Leijtens, L. M. Herz, A. Petrozza and H. J. Snaith, *Science*, 2013, **342**, 341-344.

7. G. Xing, N. Mathews, S. Sun, S. S. Lim, Y. M. Lam, M. Grätzel, S. Mhaisalkar and T. C. Sum, *Science*, 2013, **342**, 344-347.

8. Q. Dong, Y. Fang, Y. Shao, P. Mulligan, J. Qiu, L. Cao and J. Huang, *Science*, 2015, **347**, 967-970.

9. H.-S. Kim, C.-R. Lee, J.-H. Im, K.-B. Lee, T. Moehl, A. Marchioro, S.-J. Moon, R. Humphry-Baker, J.-H. Yum and J. E. Moser, *Sci. Rep.*, 2012, **2**.

10. G. E. Eperon, V. M. Burlakov, P. Docampo, A. Goriely and H. J. Snaith, *Adv. Funct. Mater.*, 2014, **24**, 151-157.

11. H.-S. Kim, J.-W. Lee, N. Yantara, P. P. Boix, S. A. Kulkarni, S. Mhaisalkar, M. Grätzel and N.-G. Park, *Nano Lett.*, 2013, **13**, 2412-2417.

12. N.-G. Park, *J. Phys. Chem. Lett.*, 2013, **4**, 2423-2429.

13. M. A. Green, K. Emery, Y. Hishikawa, W. Warta and E. D. Dunlop, *Prog. Photovoltaics*, 2015, **23**, 1-9.

14. H. S. Jung and N. G. Park, *Small*, 2015, **11**, 10-25.

15. W. Nie, H. Tsai, R. Asadpour, J.-C. Blancon, A. J. Neukirch, G. Gupta, J. J. Crochet, M. Chhowalla, S. Tretiak, M. A. Alam, H.-L. Wang and A. D. Mohite, *Science*, 2015, **347**, 522-525.

16. C. M. Hsu, C. Battaglia, C. Pahud, Z. Ruan, F. J. Haug, S. Fan, C. Ballif and Y. Cui, *Adv. Energy Mater.*, 2012, **2**, 628-633.

17. S. Zhong, B. Liu, Y. Xia, J. Liu, J. Liu, Z. Shen, Z. Xu and C. Li, *Sol. Energy Mater. Sol. Cells*, 2013, **108**, 200-204.

18. C. D. Bailie, M. G. Christoforo, J. P. Mailoa, A. R. Bowring, E. L. Unger, W. H. Nguyen, J. Burschka, N. Pellet, J. Z. Lee, M. Gratzel, R. Noufi, T. Buonassisi, A. Salleo and M. D. McGehee, *Energy Environ. Sci.*, 2015, **8**, 956-963.

19. G. E. Eperon, V. M. Burlakov, A. Goriely and H. J. Snaith, *ACS nano*, 2013, **8**, 591-598.

20. M. A. Green, A. Ho-Baillie and H. J. Snaith, *Nature Photon.*, 2014, **8**, 506-514.

21. L.-M. Huang, C.-W. Hu, H.-C. Liu, C.-Y. Hsu, C.-H. Chen and K.-C. Ho, *Sol. Energy Mater. Sol. Cells*, 2012, **99**, 154-159.

22. X. Fang, Y. Li, X. Wang, J. Ding and N. Yuan, *Sol. Energy*, 2015, **116**, 100-107.

23. F. Guo, H. Azimi, Y. Hou, T. Przybilla, M. Hu, C. Bronnbauer, S. Langner, E. Spiecker, K. Forberich and C. J. Brabec, *Nanoscale*, 2015, **7**, 1642-1649.

24. E. Della Gaspera, Y. Peng, Q. Hou, L. Spiccia, U. Bach, J. J. Jasieniak and Y.-B. Cheng, *Nano Energy*, 2015, **13**, 249-257.

25. P. You, Z. Liu, Q. Tai, S. Liu and F. Yan, *Adv. Mater.*, 2015, **27**, 3632-3638.

26. Y. Shao, Z. Xiao, C. Bi, Y. Yuan and J. Huang, *Nat. Commun.*, 2014, **5**, 5784.

27. Q. Wang, Y. Shao, Q. Dong, Z. Xiao, Y. Yuan and J. Huang, *Energy Environ. Sci.*, 2014, **7**, 2359-2365.

28. J. Xu, A. Buin, A. H. Ip, W. Li, O. Voznyy, R. Comin, M. Yuan, S. Jeon, Z. Ning and J. J. McDowell, *Nat. Commun.*, 2015, **6**, 7081.

29. M. Xiao, F. Huang, W. Huang, Y. Dkhissi, Y. Zhu, J. Etheridge, A. Gray-Weale, U. Bach, Y. B. Cheng and L. Spiccia, *Angew. Chem.*, 2014, **126**, 10056-10061.

30. G. E. Eperon, D. Bryant, J. Troughton, S. D. Stranks, M. B. Johnston, T. Watson, D. A. Worsley and H. J. Snaith, *J. Phys. Chem. Lett.*, 2014, **6**, 129-138.

31. J. Krantz, T. Stubhan, M. Richter, S. Spallek, I. Litzov, G. J. Matt, E. Spiecker and C. J. Brabec, *Adv. Funct. Mater.*, 2013, **23**, 1711-1717.

32. W. Zhang, M. Saliba, D. T. Moore, S. K. Pathak, M. T. Hörantner, T. Stergiopoulos, S. D. Stranks, G. E. Eperon, J. A. Alexander-Webber, A. Abate, A. Sadhanala, S. Yao, Y. Chen, R. H. Friend, L. A. Estroff, U. Wiesner and H. J. Snaith, *Nat. Commun.*, 2015, **6**, 6142.

33. H. J. Snaith, R. Humphry-Baker, P. Chen, I. Cesar, S. M. Zakeeruddin and M. Grätzel, *Nanotechnology*, 2008, **19**, 424003.

34. M.-F. Xu, H. Zhang, S. Zhang, H. L. Zhu, H.-M. Su, J. Liu, K. S. Wong, L.-S. Liao and W. C. Choy, *J. Mater. Chem. A*, 2015, **3**, 14424-14430.

6 ENERGY-SMART WEAVABLE RIBBONS FOR SIMULTANEOUS ENERGY HARVEST AND STORAGE

6.1 Introduction

In December of 2015, the world leaders from around 200 countries met in Paris to discuss climate change and global warming[1,2], and find strategies to minimize the greenhouse effect mainly caused by excessive use of fossil fuels as an energy source[3-5]. However, energy is a basic necessity for the growth and development of human civilization[6]. Therefore to reduce fossil fuel consumption, it is very necessary to make green energy harvest and storage easy and portable. For example, in many instances, cars parked directly under the sun fail to utilize the abundant energy from sunlight[7]. If a flexible matrix made of filaments capable of harvesting and storing energy were to be integrated into the roof of a car, the stored solar energy could be used to operate the car whenever needed. In addition, if these filaments are incorporated into jackets, they could be used to charge wearable electronics[8-10]. Thus a single filament which can simultaneously harvest and store electric energy is a ‘‘Holy Grail’’ for achieving this goal.

Additional efforts to produce integrated devices have already been pursued by combining photoelectrodes and wet storage devices, but these methods are not suitable for wearables or other similar applications due to its device architecture[11]. Attempts to power wearables using two independent energy harvesting and storing devices have already been pursued[12-14], but a single device which can perform both the functions is still lacking.

In this study, we report an all solid state, energy harvesting and storing (ENHANS) filament which integrates perovskite solar cell (PSC) on top of a symmetric supercapacitor (SSC)

via a copper filament which works as a shared electrode for direct charge transfer. We developed a highly flexible, thin, sandwich PSC with more than 10% conversion efficiency by a solvent-assisted perovskite growth technique[15]. The sandwich-type device configuration provides better protection for the solar cell against environmental effects due to an unexposed perovskite layer to the atmosphere. Copper ribbon not only serves as an electron collecting electrode for the solar cell but also as a substrate for generating copper hydroxide nanotubes (CuOHNT) for developing the supercapacitor. A SSC is developed by gluing a second CuOHNT based copper ribbon with polyvinyl alcohol (PVA) containing potassium hydroxide (KOH) gel electrolyte onto the CuOHNT grown side of the copper ribbon electrode of the solar cell. Making use of the shared electrode, the charges generated by the flexible thin film perovskite solar cell are directly transferred and stored in the CuOHNT of the supercapacitor. Developing ENHANS on a copper filament provides a low-cost solution for flexible self-sufficient energy systems for wearables and other portable devices. For example, a jacket made of this textile can harvest solar energy and directly store it in itself eliminating the need of a separate storage battery. We demonstrate that ENHANS filaments can be made into a matrix/textile which can be very useful for powering devices, buildings or vehicles[16,17].

6.2 Working principle of ENHANS

The schematic of the ENHANS filament architecture and charge transfer mechanism is shown in Figure 6.1 to illustrate its working principle. The supercapacitor is prepared with CuOHNT electrodeposited with MnO_2 on a Cu tape. This offers the opportunity to integrate high performance solar harvesting perovskite materials on the other side of the Cu electrode to transform it into a single bi-functional energy device (detailed fabrication approach is presented

in Figure 6.2). Figure 6.1a represents the schematic of the integrated device. As shown in Figure 6.1b, ENHANS filament consists of three electrodes: 1- negative electrode used as a shared electrode between perovskite solar cell (PSC) and supercapacitor, 2- positive electrode of perovskite solar cell and 3- positive electrode of the supercapacitor. To generate charges in the perovskite solar cell and successfully transfer the harvested charges to the supercapacitor for storage, the copper tape (electrode 1) of the supercapacitor is used as the shared electrode. One end of the positive electrode (electrode 2; top electrode) of the solar cell is directly connected to the cathode (electrode 3; bottom electrode) of the supercapacitor through a switch. Figure 6.1b demonstrates the proposed electron transfer mechanism of ENHANS. During photo-charging (switch S1 closed), the photoactive perovskite materials generate electrons (e^-) as well as holes (h^+), and electrons move to the electron transport layer Phenyl-C61-butyric acid methyl ester (PCBM) and then to the electron collecting electrode (copper ribbon) of the solar cell from where it is directly transferred to the anode of the supercapacitor. At the same time holes move to the hole collector electrode, indium tin oxide (ITO) of the solar cell. The electrons reached at the anode of the supercapacitor are stored by the pseudocapacitive reaction, $MnO_2 + K^+ + e^- \rightarrow MnOOK$. Simultaneously, the reverse reaction at the cathode of the supercapacitor releases the electron which travels to the hole-collector electrode of the solar cell to combine with the holes since they are in contact with each other. During the discharging process (S1 is open and S2 is closed), the stored charge in the supercapacitor discharges and provides power to the connected device. The steps involved in the fabrication of ENHANS filament with dual functionality is presented. A photograph showing a military uniform incorporating a light weight fabric woven with ENHANS filaments and cotton threads.

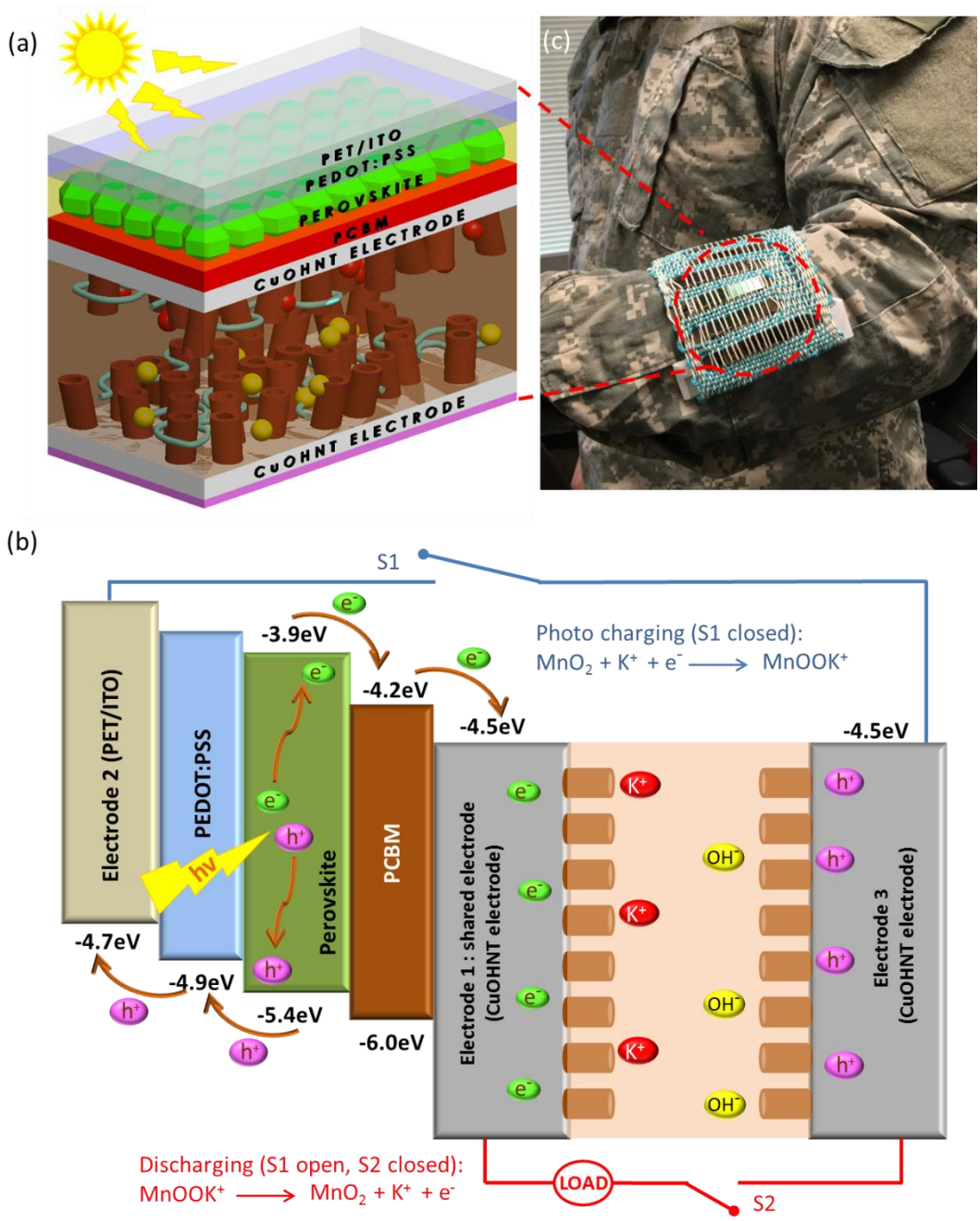

Figure 6.1 Schematic illustrating the architecture and charge transfer mechanism of ENHANS filaments. (a) Schematic showing ENHANS filament consisting of the top PSCs and bottom SSC with shared copper electrode. This "bi-functional energy ribbon" has been realized based on the copper filament as an anode (Electrode 1) for both PSCs and SSCs, while ITO/PET and another thin copper ribbon act as cathodes (Electrodes 2 and 3) for PSCs and SSC, respectively. (b) Charge transfer mechanism of the combination device: As ITO/PET and copper tape are connected to form close circuit (S1 closed), the photogenerated holes and electrons from PSCs flow into the cathode and anode of SSC respectively. This current flow leads to the charging of SSC. The energy stored through the charging process can be discharged to do

external work (S1 open & S2 closed). (c) A photograph showing a military uniform incorporating a light weight fabric woven with ENHANS filaments and cotton threads.

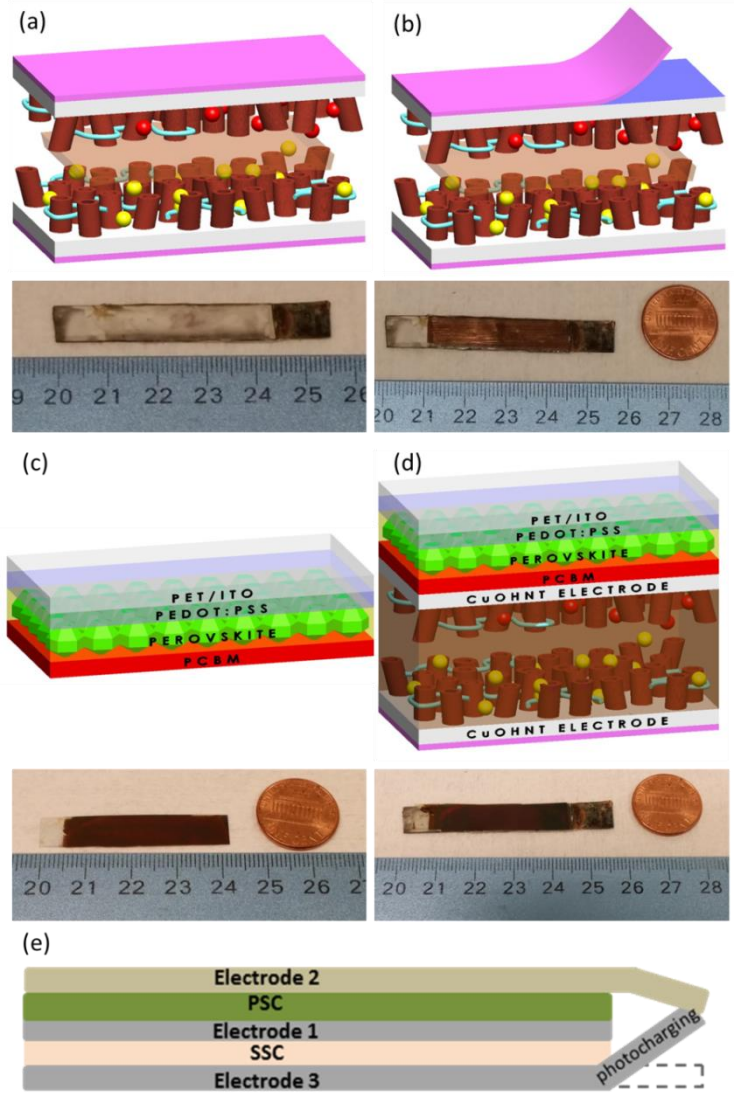

Figure 6.2 Procedure for fabricating ENHANS filament. (a) All solid state symmetric supercapacitor, (b) supercapacitor after peeling off the paper cover from one of the copper tape electrode side to expose the sticky nature of the charge storage device, (c) multilayer energy harvesting solar active perovskite materials partly coated on transparent ITO/PET and (d) integrated the solar active part on top of the supercapacitor sticky part side to share the copper tape as a single electrode, (e) one end of the positive electrode (electrode 2; top electrode) of the solar cell is directly connected to the cathode (electrode 3; bottom electrode) of the supercapacitor through a switch.

6.3 Fabrication and performance of supercapacitor

We developed a binder-free nanostructured ribbon supercapacitor which can be easily integrated with future energy generation technologies. This was accomplished by growing CuOHNT of about 200 nm diameter and about 10 μm in length, on a commercially available copper ribbon (Figure 6.3).

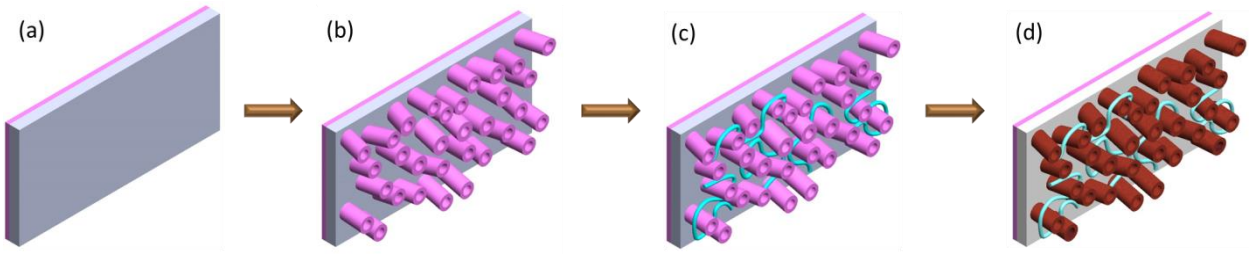

Figure 6.3 Schematic illustration of the MnO_2 deposited $Cu(OH)_2$ nanotubular architecture. (a) Commercial copper tape, (b) $Cu(OH)_2$ nanotubes grown on Cu tape at room temperature by a solution method, (c) $Cu(OH)_2$ nanotubes on Cu tape after deposition of Ag-nanowires and (d) final electrode of Cu-tape obtained after MnO_2 electro-deposition on tubular $Cu(OH)_2$ structure.

Briefly, CuOHNT are grown by a 20 minute room temperature wet chemical process[18-20]. The Scanning Electron Microscope (SEM) images in Figure 6.4a,b represent the hollow tubular structure of the grown CuOHNT. The low and high resolution Transmission Electron Microscope (TEM) images also serve as a clear evidence of the hollow nature of the nanotubes (Figure 6.5).

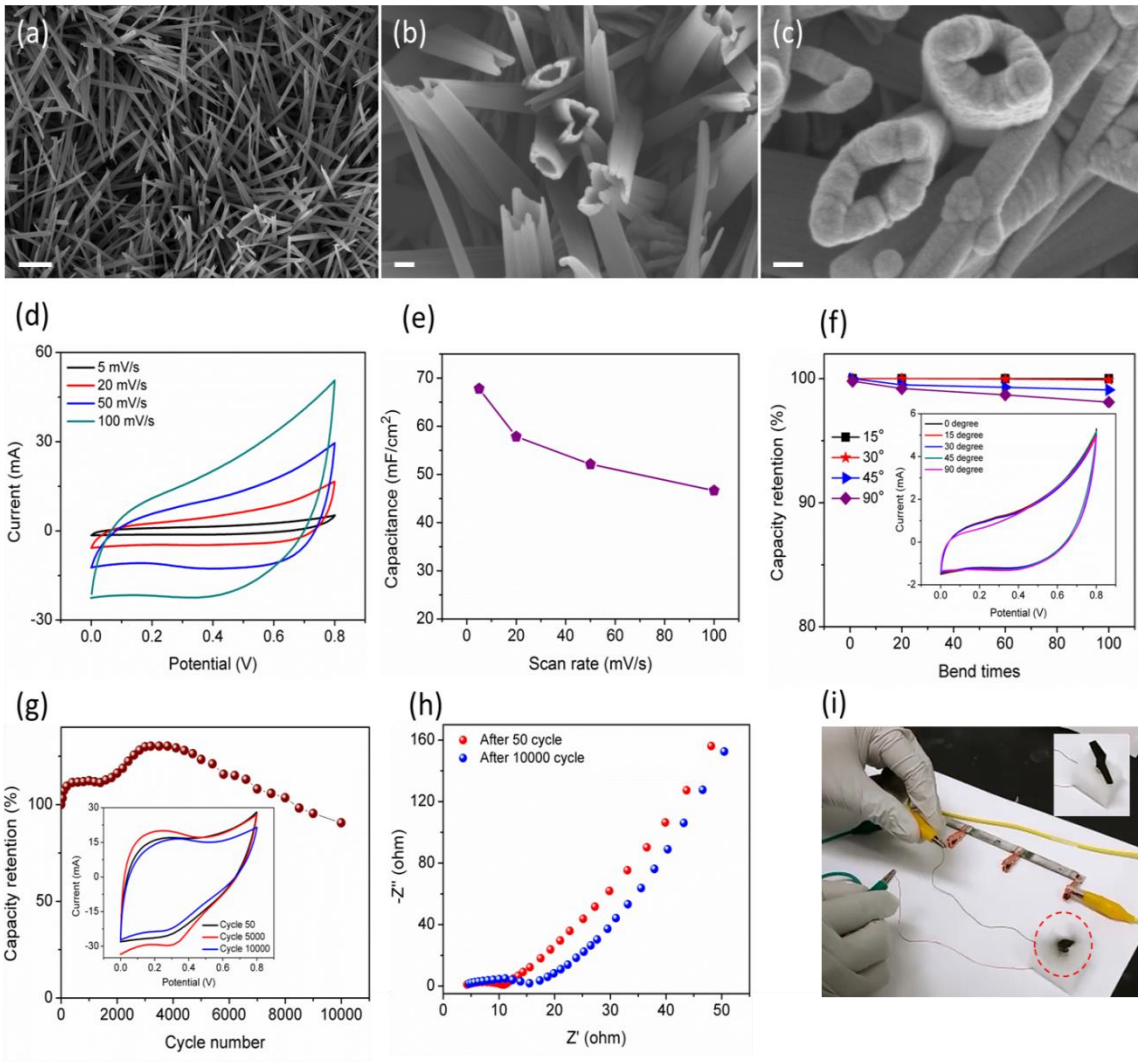

Figure 6.4 Nanoarchitecture of the electrode material and electrical analysis of the assembled symmetric supercapacitor device. (a) Low (Scale: 2 µm) and (b) high (Scale: 200 nm) magnification FE-SEM images of CuOHNT represents the length (~8 µm) as well as diameter (~200 nm) of the room temperature grown CuOHNT, (c) high magnification FE-SEM image of MnO2 deposited tubular nanoarchitecture (Scale: 80 nm), (d) CV profile of the device at different scan rates, (f) cell capacitance calculated from the CV curves, (e) capacitance of the device at different bending angles (inset shows the CV curves at various bending angle), (g) cycle life study to explore the continuous electrochemical effect on the stability of the MnO_2 deposited nanotubes (inset represents the CV curve of the device at certain cycle numbers), (h) Nyquist plot obtained from the EIS study of the as-prepared device and (i) rotating a propeller of toy drone with three charged supercapacitors in series. Inset is the picture of the propeller before connecting to the supercapacitor.

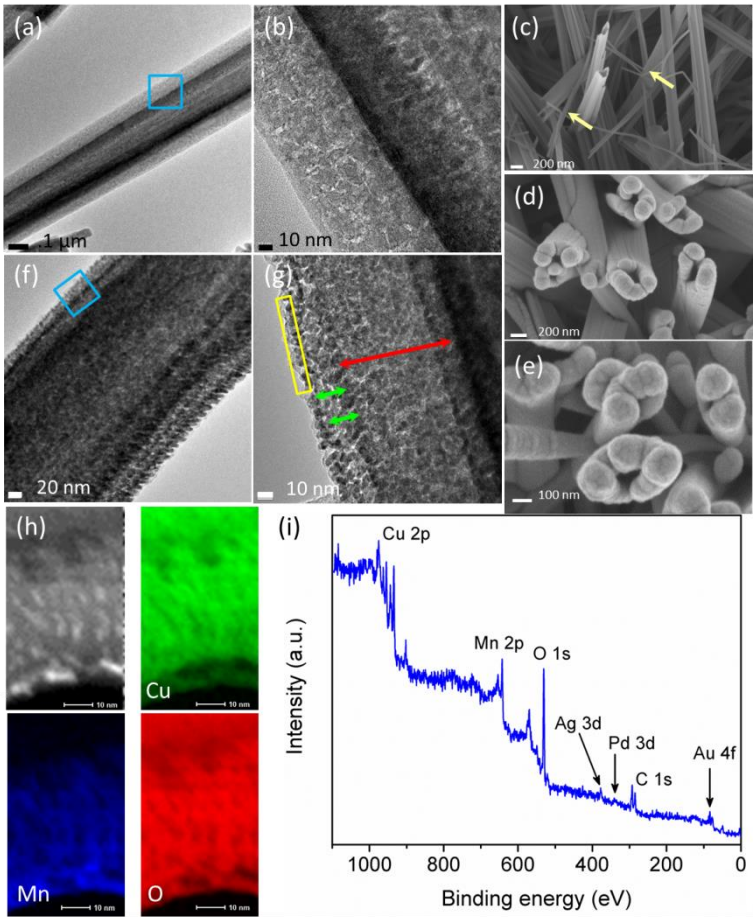

Figure 6.5 Structural and compositional analysis of nanofabricated MnO_2 deposited interconnected CuOHNT. (a) Low and (b) high resolution TEM images of CuOHNT reveals the internal hollow architecture of as prepared nanotubes, (c) high resolution SEM images after AgNW (marked with arrows) deposition, (d) high resolution FESEM of nanotubes after AuPd coating, (e) high resolution SEM images of MnO_2 deposited nanotubes, (f) low and (g) high resolution TEM images of MnO_2 deposited nanotubes (red arrow shows the thickness of the CuOHNT walls, green arrow represents the AuPd layer on nanotube as well as yellow box is used to indicate the electrodeposited MnO_2 layer on the nanotubes. ELS mapping image of selected area of nanotubes (h) to reveal the elemental (Cu, Mn and O) distribution on the nanotubes surface and (i) XPS survey analysis of the electro material.

To characterize the capacitive behavior of the electrode, we have performed cyclic voltammetry (CV) studies using a three electrode system. The electrochemical response presents a substantial enhancement of the area for MnO_2 deposited electrodes compared to bare CuOHNT electrodes in Figure 6.6a. This signifies the pseudocapacitive energy storage capability to store large amounts of charge in the nanotubes of the electrodes. A similar trend of charge storage

with longer charging/discharging time has been observed for the electrodes during galvanostatic charge discharge (GCD) at a constant current density (Figure 6.6b). The fabrication effect of the MnO_2 deposited CuOHNT and interconnected network of AgNW boosts the capacitance of the final electrodes to 145.15 mF cm^{-2}. This is almost 10 times greater than that of a bare CuOHNT electrode. This outstanding capacitive behavior has also been observed at constant current density charge/discharge processes (89.25 mF cm^{-2} at 1 mA cm^{-2}). The tubular nano-architecture of the electrode materials prepared from CuOHNTs provides highly capacitive nano-layer of MnO_2 to store a large amount of charges in the nanotubes. Moreover, the interconnected highly conductive network of AgNW created among the nanotubes facilitates the charges to transport throughout the electrode instantly. Including this synergistic effect, the highly interactive area of the electrode encounters exceptional interfacial contact at the electrode-electrolyte surface which prompts the ion transfer ability of the system and plays a key role in providing an excellent charge capacitive behavior[21-23]. The hollow nanotube structure also exhibits good rate capability and nearly ideal CV curves (Figure 6.6c) at different scan rates (5 to 100 mV s^{-1}) resulting in capacitance of 149.15 mF cm^{-2} to 96.46 mF cm^{-2} (Figure 6.6d). At different current densities (1 mA cm^{-2} to 8 mA cm^{-2}), the electrodes reveal nearly symmetrical charge/discharge profiles which represent highly reversible behavior of the electrode materials (Figure 6.6e) and promising capacitance values of 89.25 mF cm^{-2} to 67.15 mF cm^{-2}(Figure 6.6f). The electrochemical response of the tubular nanostructure is superior to the previously reported supercapacitor electrode materials prepared by MnO_2[24-29].

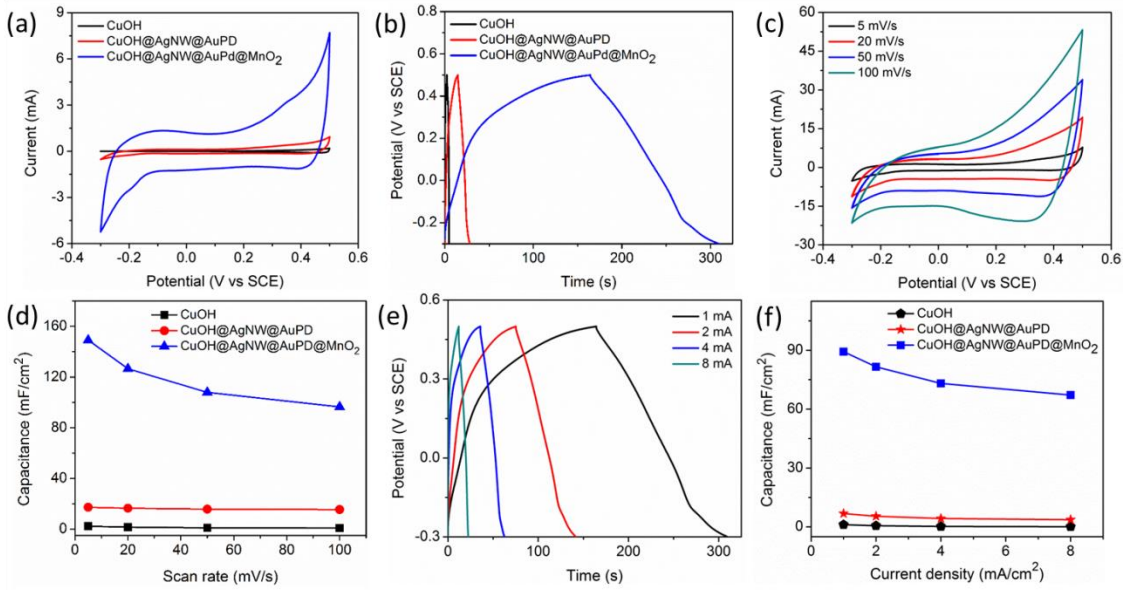

Figure 6.6 Electrochemical analysis of the single electrode in a three electrode system. (a) CV study of the electrodes as an effect of different materials nanofabricated on $Cu(OH)_2$ nanotubes, (b) GCD study support the similar trend of materials fabrication for charge storage, (c) CV of the electrode after 12 min MnO_2 electrodeposition at different scan rates, (d) specific capacitance calculated from CV study, (e) GCD of the electrode after 12 min MnO_2 electrodeposition at different scan rates and (f) specific capacitance calculated from CV study.

To make an ENHANS filament, we have developed a symmetric all solid-state supercapacitor device from this CuOHNT based electrodes. A schematic of electrode fabrication, materials characterization and electrochemical analysis of the fabricated supercapacitor are provided. A concise discussion about the fabrication procedure of the supercapacitor filament is given in the Methods section. Electrochemical evaluation of the supercapacitor filament developed is given. The CV study of the supercapacitor filament reveals nearly-ideal oxidation-reduction behavior of the nanoarchitecture (Figure 6.4d). The synchronization effect of the MnO_2 coated tubular nanostructure enables the assembled supercapacitor to deliver a capacitance of 67.78 mF cm^{-2} at 5 mV s^{-1}. The areal specific capacitance obtained from the assembled

supercapacitor is comparable or better than the previously reported charge storage devices with similar nanostructured electrodes [10,27,28,30-36]. Upon performing different scan rates, the CV of the device represents rate capability of 68.8% and results in capacitances of 67.78 mF cm^{-2} (5 mV s^{-1}), 57.83 mF cm^{-2} (20 mV s^{-1}), 52.12 mF cm^{-2} (50 mV s^{-1}), and 46.64 mF cm^{-2} (100 mV s^{-1}) as shown in Figure 6.2e. The supercapacitor is also able to withstand a very high capacitive performance at a low current density of 1 mA cm^{-2} as well as a high current density of 8 mA cm^{-2} (Figure 6.7a). The capacitance values calculated from the discharge part of the GCD profile ranging from 48.03 mF cm^{-2} (1 mA cm^{-2}) to 26.99 mF cm^{-2} (8 mA cm^{-2}) (Figure 6.7b). Moreover, the supercapacitor results in an almost symmetric GCD profile which indicates higher coulombic efficiency of the electrode materials as well as devices at various current densities.

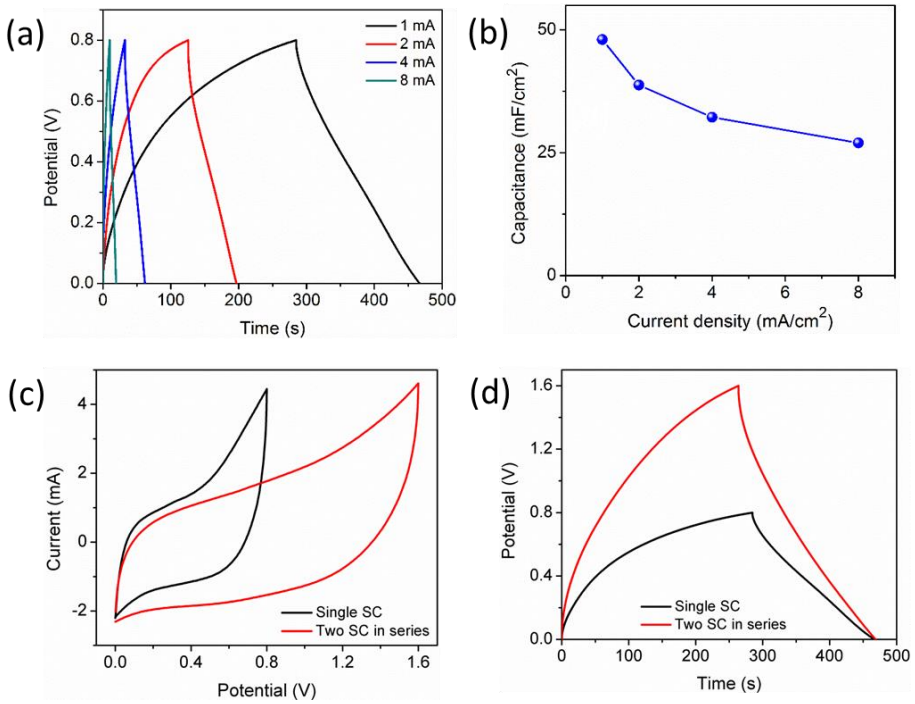

Figure 6.7 Electrochemical analysis of the symmetric supercapacitor study. (a) Charge-discharge study of the device at different current densities, (b) cell capacitance calculated from the GCD study, (c) CV of a single supercapacitor compared to the CV of two supercapacitor in series and (d) GCD of a single supercapacitor compare to the GCD of two supercapacitor in series.

The interconnected tubular nanostructures not only provide high capacitance but also exhibit negligible degradation in performance upon mechanical deformation. The PVA gel electrolyte protects the device from mechanical stresses. The strong interaction between the current collector and the chemically grown CuOHNT coated with MnO_2 results in similar electrochemical behavior upon bending at different angles as shown in Figure 6.4f. The capacitive performance of the device is highly stable even after a significant amount of repeated bending (98% of initial capacitance retention at 5 mV s^{-1} after 100 bending cycles at 90°). The continuous electrochemical charge-discharge ability of the device has also been studied; CV at 50 mV s^{-1} for 10,000 cycles. A capacitance retention of about 91% even after 10,000 cycles indicates that CuOHNT approach is very attractive for high performance supercapacitors. An increase of capacitance of about 30% from the initial value is associated with the tubular nature of the nanostructure where the electrolyte ions continues to penetrate even after the initial electrochemical cycling and expose the full electroactive surface of the hollow nanotubes (Figure 6.4g). The materials stability, interconnected nanotubular structure and ionic interaction on electrode-electrolyte surface and high cycle life makes this device one of the best reported metal oxide based long lasting energy storage systems[23,27,31,32,34]. The Nyquist plot in Figure 6.4h shows that an electron impedance spectrum (EIS) after 10,000 cycles is similar to that after 50 cycles. The continuous cycling can only affect the internal cell resistance resulting from long shuttling of electrolyte ions and inefficient electrical contact between the nanoarchitecture and the copper ribbon surface[37]. The as-prepared supercapacitor can provide a wider potential window and higher charge storage ability when they are connected in series (Figure 6.7c,d). To demonstrate the working of the supercapacitor, three devices connected in series are charged by

an electrochemical workstation and used the stored charge to rotating a propeller of a toy drone (Figure 6.4i).

6.4 Fabrication and performance of perovskite solar cells

To build perovskite solar cell part for the ENHANS filament, we first fabricated a photo-harvesting layer of methylammonium lead iodide ($CH_3NH_3PbI_3$) on a flexible Indium Tin Oxide (ITO)/polyethylene terephthalate (PET) substrate with a layer of hole transport layer of poly(3,4-ethylenedioxythiophene) polystyrene sulfonate (PEDOT:PSS) on one side and PCBM on the other side as an electron transport layer. The device architecture before attaching to the shared electrode is: ITO/PEDOT:PSS/$CH_3NH_3PbI_3$/PCBM. All the post-treatment requires only low annealing temperature, which makes this device architecture a promising candidate for large scale fabrication[38]. Solar cell fabrication and characterization details can be found in the methods part. The $CH_3NH_3PbI_3$ perovskite layer was prepared by a chlorobenzene (CB) assisted method to grow large perovskite crystals with grain sizes more than 1 μm for achieving a high performance [15]. To assess the quality and grain size of the perovskite film formed by CB-assisted growth process with respect to that of the control sample (non-assisted growth), we inspected top view SEM image of the CB assisted growth film and control sample. The film obtained by CB-assisted method exhibits considerably large crystal grains (~1 μm) and almost full coverage on the substrate without any pinholes, while the control sample shows small crystal grains (300 nm) with pinholes. After coating PCBM on top of a perovskite layer, copper ribbon with the conductive adhesive side of the supercapacitor was pressed on top of the PCBM layer to complete the ENHANS filament. It is to be noted that the adhesive on the reverse side of the copper ribbon is highly conductive and the assembled filament is mechanically stable as a single

integrated device as evidenced by the bending tests of the device discussed in the following section.

An independent copper filament PSC provides a short-circuit current density (J_{sc}) of 16.44 mA cm^{-2}, open-circuit voltage (V_{oc}) of 0.96 V, fill factor of 0.66 and a power conversion efficiency of 10.41% for reverse scan as shown in Figure 6.8b. The J_{sc} matched well with the current density of 16.6 mA cm^{-2} calculated from external quantum efficiency (EQE) measurement (Figure 6.8c). The inset of Figure 6.8c shows our PCE using CB-assisted growth and a comparison with other reported inverted flexible PSC using different thermal evaporated negative electrodes: Gold (Au) and Aluminum (Al). Carmona et al.[39] reported inverted flexible perovskite solar cells comprised of Ag/PEDOT:PSS/PolyTPD/$CH_3NH_3PbI_3$/PCBM/Au exhibiting an efficiency of 7%. In this work, an additional electron block layer-PolyTPD has been inserted in between PEDOT:PSS and perovskite layer. You et al.[40] reported a PCE of 9.2% for a mixed halide ($CH_3NH_3PbI_{3-x}Cl_x$) solar cell composed of ITO/PEDOT:PSS/$MAPbI_{3-x}Cl_x$/PCBM/Al. Compared with the above thermal evaporation processes for making Au and Al negative electrode, our copper ribbon electrode is less expensive and require shorter processing time. By using flexible copper ribbon as an anode, a high performance of 10.41% was achieved along with a much improved environmental stability which is very important for commercial applications. The copper ribbon as the top electrode plays an important role for enhancing the stability of perovskite solar cells because it effectively blocks the permeation of moisture and oxygen into the perovskite layer and our device delivers one of the best performances of sandwich-type PSC. In Figure 6.8d, the laminated perovskite solar cells have superior lifetimes than devices with 100 nm thermally-evaporated Cu electrodes. After exposing it to air for 10 days, the normalized PCE of devices with Cu tape electrodes still shows 90% of their initial

efficiencies, while devices with evaporated Cu electrode degrades significantly from 100% to 20%. It is to be noted that further improvement in stability can be achieved by sealing the edges of our filaments which is not presently sealed and protected. Also, our current results represent one of the best performances with respect to the environmental stability of flexible perovskite solar cells[41,42]. Another advantage of this design is that the device exhibits good mechanical flexibility. The PCE of the flexible perovskite solar cells is measured after being bent repeatedly at 120° angle. The PCE shows minimal deterioration even after bending 100 times, retaining 90% of its initial PCE value (Figure 6.8e) due to high flexibility and adhesive property of copper tape/filament. The XRD measurement was used to investigate the crystallinity of the perovskite film (Figure 6.9c). Two peaks can be identified at 14.100 and 28.470 which are assigned to be 110 and 220 diffraction peaks for the $CH_3NH_3PbI_3$ material with a tetragonal crystal structure[43]. The UV-vis absorption measurement was performed (Figure 6.9d)to demonstrate the promising absorption property of perovskite layer.

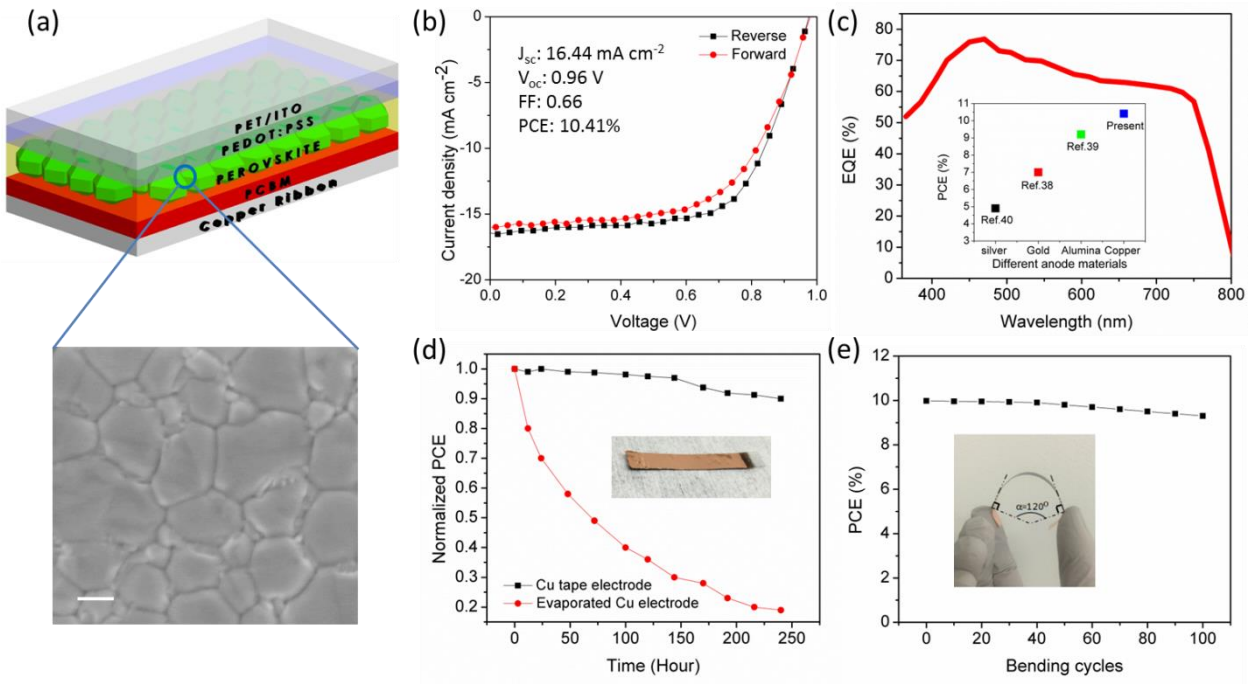

Figure 6.8 Device performance of perovskite solar cell with corresponding device structure. (a) The schematic of a flexible perovskite solar cell with Cu tape anode. Zoomed-in region of the perovskite layer represents SEM image of perovskite grain crystal with 1 μm crystal grain size. Scale : 500 nm. (b) *J-V* curve of the best device under one sun conditions (100 mW cm^{-2}, AM 1.5G). (c) EQE versus wavelength for the device; inset shows a comparison of the present PCE with other reported inverted flexible PSC using different thermal evaporated negative electrodes. (d) Normalized PCE of PSC made with Cu tape electrode and thermally-evaporated Cu electrodes after being stored in air for 240 hours. (e) PCE stability based on the bending cycles for PSCs with a 120° angle; inset shows the photograph of the bending process and angle determination.

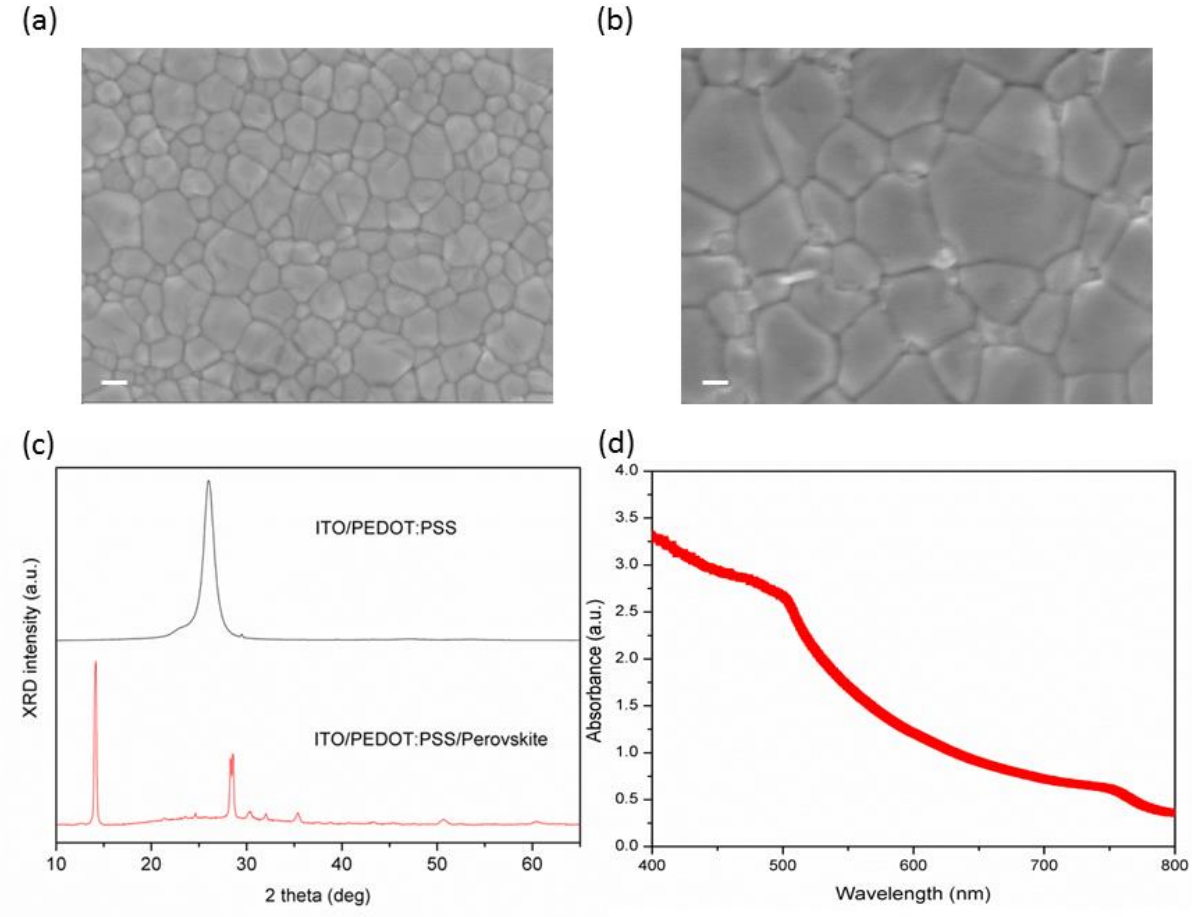

Figure 6.9 Material characterization of $CH_3NH_3PbI_3$ perovskite films. (a) SEM image of control sample grown perovskite film by traditional method. (b) SEM image of sample grown perovskite film by CB-assisted growth method. Scale: 200 nm. (c) XRD pattern of the perovskite crystals grown on PEDOT:PSS/ITO (red line), with blank sample of the PEDOT:PSS coated ITO substrate for comparison (black line). (d) UV-vis absorbance of $CH_3NH_3PbI_3$ perovskite films on PET substrate.

6.5 Performance and weaving of the ENHANS filaments

After testing the performance of the independent devices, the synergistic effect of the integrated device is verified. In the integrated ENHANS filament, the solar cell part is able to generate ~4 mA current with photo-charging process. The charges generated at the perovskite solar cell are directly delivered to charge the supercapacitor through the shared electrode

according to our proposed mechanism in Figure 6.1b. The constant charge transfer at 4 mA from solar cell to supercapacitor can make the supercapacitor fully charged to a potential of 0.8 V within 1 minute of illumination. For ENHANS filament performance analysis, we have photo-charged the filament for 1 minute and discharged with electrochemical workstation at various current densities (1 mA cm^{-2} to 8 mA cm^{-2}) after waiting for 10 seconds after the seizure of photo-charging (Figure 6.10a). This indicates that the harvested energy by the solar cell stored in the supercapacitor part of the device is available when necessary. By using the discharge time in Figure 6.10a, we have calculated and plotted the energy density 1.82 mWh cm^{-3} and power density 36.19 mW cm^{-3} at 1 mA cm^{-2} current density of the ENHANS filament and compared the performances with the independent supercapacitor (Figure 6.10b and Table 6.1). The Ragone plot in Figure 6.10b shows that the performance of the supercapacitor in the ENHANS filament is similar to a solo supercapacitor. By photo-charging with 4 mA cm^{-2} current density, the ENHANS experience an energy density of 1.15 mWh cm^{-3} at a power density of 125.25 mW cm^{-3} which is very comparable with the previously reported independent supercapacitor and other similar devices[23,27,28,31,32,36,44,45]. The energy and power density of the ENHANS filaments are slightly inferior at lower current density discharge rate (1 mA cm^{-2} and 2 mA cm^{-2}) compared to a solo supercapacitor when it is charged/discharged with electrochemical work station at similar current density. During photo-charging the supercapacitor part is charged with higher current density (4 mA cm^{-2}) for 1 min through the PSC. Apparently, the amount of charge stored is lower compared to the solo supercapacitor when it is charged with the electrochemical workstation at 1 or 2 mA cm^{-2} and the ENHANS filaments discharge quicker compared to the single SSC and experience lower energy as well as power densities. However, at a higher current density discharge rate, the energy and power density of the ENHANS filament is similar to the

supercapacitor itself as it is photo-charged at 4 mA cm^{-2} which is close to the charging current for the SSC by the electrochemical workstation (Figure 6.10b).

Table 6.1 Comparative energy density and power density of the as-prepared symmetric supercapacitor and the performance of the ENHANS filament under photo charging and discharging with a potentiostat.

Current density(mA cm^{-2})	Energy density (mWh cm^{-3})		Power density (mW cm^{-3})	
	SSC	ENHANS	SSC	ENHANS
1	1.825	1.419	36.193	32.05
2	1.442	1.334	74.011	70.561
4	1.114	1.152	134.483	125.254
8	0.799	0.843	261.021	243.467

With our low temperature, simple fabrication method, the lightweight ENHANS filament exhibits high flexibility. To demonstrate this, we have carried out a bending test on our filaments by bending the device at 90^0 for a certain number of times [20, 50, 100 at 90° angle] (Figure 6.10c,d) and subject the device to photo-charging and discharging at 1 mA cm^{-2} current density. The flexible nature of the electrodes provides the ENHANS filament the ability to withstand external mechanical deformation. In Figure 6.10e, the discharge curve of the device after a certain number of bending cycles is almost identical to the electrochemical response of a device without bending.

The interlacement of filaments with ENHANS filaments into a textile provides added mechanical strength. This type of woven structure enables the introduction of various types of

filaments to meet the requirements of a given application in which the device is being used. A plurality of filaments can be woven into a single fabric structure. Figure 6.10f is a schematic showing the ENHANS filaments woven into a textile form with supporting cotton yarns (green line). To demonstrate the working of ENHANS filaments as a fabric for simultaneous energy generation and storage, the matrix was exposed to a solar simulator (1 sun, AM 1.5G) to photo-charge for 1 min and used the stored charge to light an LED after ceasing the photo-charging (Figure 6.10g).

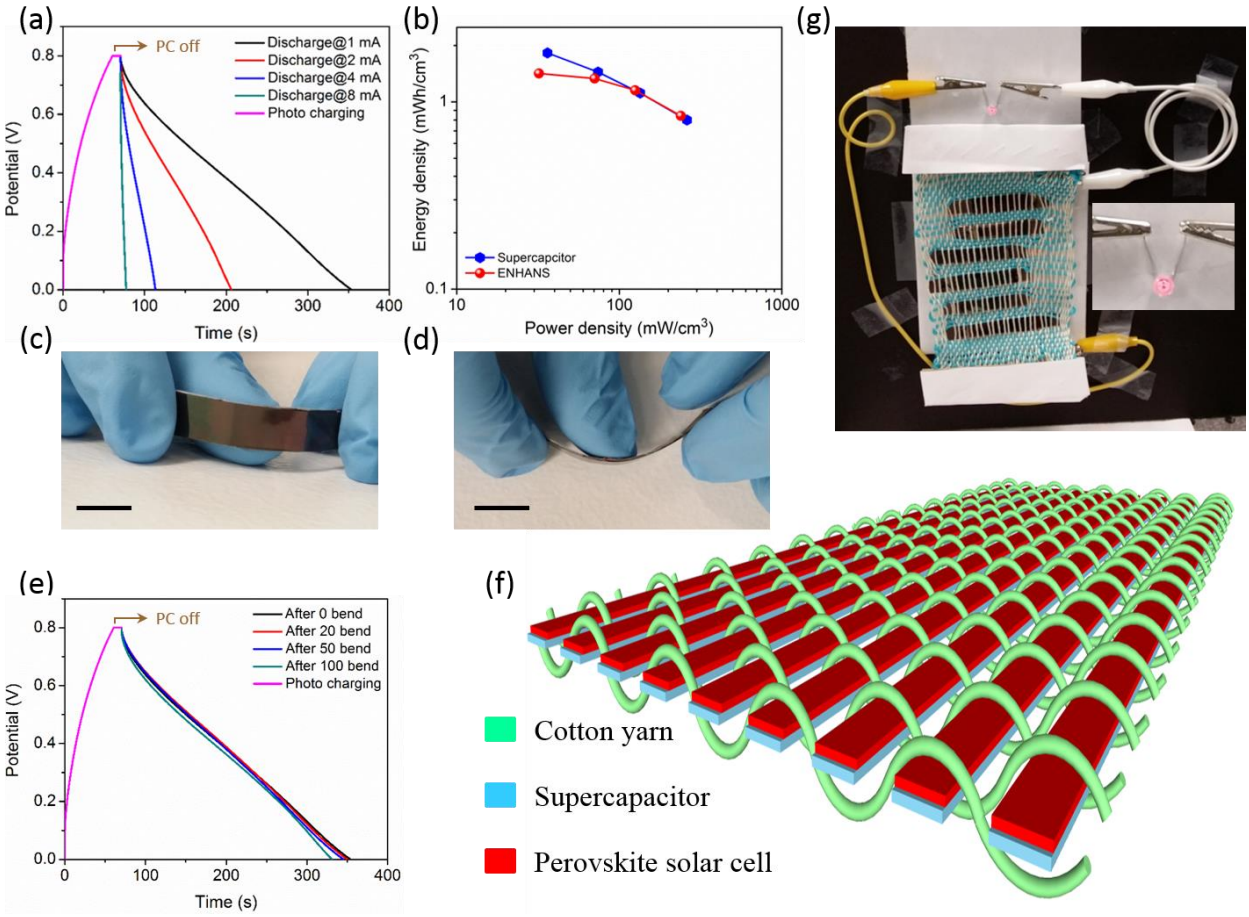

Figure 6.10 Simultaneous energy harvesting and storing analysis of the ENHANS filament. (a) Charge-discharge profile of the ENHANS filament. The solar side of ENHANS filament has been charged with the solar simulator for 1 min and discharged with electrochemical workstation at different current densities after 10 sec photo-charging (PC) off; (b) Ragone plots of an independent supercapacitor and an ENHANS filament to compare the energy density and power density at different charging-discharging rate (1, 2, 4 and 8 mA cm^{-2} current

density); (c) and (d) photograph of the ENHANS filament being bent at different angles; (e) charge-discharge profile of the ENHANS filament after a different bending cycles (the ENHANS filament has been photo-charged for 1 min, and then removed from light 10 seconds prior to discharge); (f) schematic illustration of the ENHANS filament after weaving with the cotton yarn to make a portable light weight cloth and (g) ENHANS filaments weaved with cotton thread to demonstrate the working of the light weight fabric. The photograph shows the charge deliverability of weaved matrix as a result of one minute photo-charging.

6.6 Device fabrication

6.6.1 Supercapacitor part

$Cu(OH)_2$ nanotube (CuOHNT) arrays are grown directly on a copper-tape (copper ribbon) substrate via a simple one-step reaction reported elsewhere[18-20]. The copper-tape with adhesive side masked is introduced into a chemical bath consisting of 3 g of NaOH, 0.684g of $(NH_4)_2S_2O_8$ and 30 mL of de-ionized water. After approximately 20 minutes submersion, the color of the copper samples began to turn into a light shade of blue indicating the growth of $Cu(OH)_2$ nanotubes. In order to improve charge transport between the tubes, Ag nanowires (Blue Nano^{TM}) dispersed in isopropyl alcohol at a concentration of 1 mg/mL are drop cast (6 µL) onto the $Cu(OH)_2$ electrodes and left to dry for 6 hours at 45 °C in an oven[46]. Addition of AgNW between CuOHNT provides an interconnected conductive network among the nanotube architecture. To make the charge transport more efficient, we deposited a thin layer of copper or gold-palladium (AuPd) by sputter coating at a constant current of 40 mA for 6 min on top of the CuOHNT and AgNW. AuPd coating provides a better conductivity compared to Cu[30,47]. This highly conductive matrix constitutes a favorable surface for MnO_2 electrodeposition[30] on/into the tubular nanoarchitecture. MnO_2 is deposited for 12 minutes onto the nanostructures via an anodic electrodeposition method at a constant current density of 0.5 mA cm^{-2}. The electrolyte for electrodeposition was prepared by dissolving 0.01M manganese acetate and 0.02 M ammonium

acetate into a solvent containing 10 v/v% of dimethyl sulfoxide and 90 v/v% of de-ionized (DI) water. The electron loss spectroscopy (ELS) in TEM is explored to monitor the MnO_2 morphology on the nanotubes surface. The XPS survey spectrum reveals the presence of Au (84 eV), Pd (336 eV), Ag (378 eV), Cu (934 eV), and Mn (643 eV) in the final composition of the MnO2 deposited nanotubes[47,48]. This indicates that the deposition of target materials such as MnO_2 provides a smooth nanostructure on the CuOHNT and two peaks of MnO_2 represent the Mn^{4+} oxidation state to experience excellent electrochemical response. Moreover, the tubular nature of the high aspect ratio nanostructures on the electrode surface provides highly enhanced surface area and high ion mobility at the electrode-electrolyte interface in contact with electrolyte ions[22,49,50].

The finalized supercapacitor device is then fabricated by wetting the electrode surface with 1M KOH/PVA gel electrolyte and allowing it to partially dry. Two symmetric electrodes are then pressed together with a pressure of 1 Mpa for 1 hour.

6.6.2 Solar cell part

The patterned ITO/PET substrate in the same shape (filament form) and size as the Cu tape is subsequently cleaned in an ultra-sonicator with DI water, acetone and isopropanol for 15 minutes each. On the cleaned ITO substrate, a thin layer of PEDOT:PSS (Clevios™ P VP AI 4083) is deposited by spin coating and annealed at 120 °C for 30 minutes. Subsequently, the substrate is transferred into a glove box for the deposition of perovskite absorber and PCBM layers. Perovskite precursor solution is prepared by mixing CH_3NH_3I and $PbAc_2$ in anhydrous N,N-Dimethylformamide at a 3:1 molar ratio with a final concentration of ~40 wt%. The filtered perovskite precursor is spin-casted at 3000 rpm for 45 seconds and after 6s anhydrous

chlorobenzene (150 µL) is quickly dropped onto the center of the sample. The role of chlorobenzene is to rapidly reduce the solubility of $CH_3NH_3PbI_3$ in the mixed dimethylformamide (solvent for perovskite precursor) and CB. This procedure promotes fast nucleation and growth of the crystal. The color of the film is turned from colorless to light brown instantly. The resulting film was annealed at 100 $^{\circ}$C for 10 minutes to achieve large grain size for perovskite films. The thickness of the $CH_3NH_3PbI_3$ layer is approximately 350 nm. PCBM solution is then spin-casted onto the $CH_3NH_3PbI_3$ layer at 1000 rpm for 45 seconds. For solar cell I-V measurement, copper ribbon is used as anode for performing I-V and EQE of the device.

6.6.3 Fabrication of the ENHANS

After assembling this all solid state supercapacitor in symmetric configuration, the mask on the reverse side was removed from the copper tape to expose its conducting adhesive. This is followed by pressing the PCBM layer of perovskite solar part fabricated on top of flexible ITO/PET onto the adhesive side of the copper tape. This integrates the solar part on top of the supercapacitor part to share the copper ribbon as a single electrode (negative electrode). To transfer the harvested charge from solar cell to the supercapacitor for storage, one end of the top copper electrode of supercapacitor is directly connected to the positive electrode (PET/ITO) of solar cell through a switch (Figure 6.1e).

6.6.4 Weaving of the energy smart textile

Weaving is a versatile well established technique to interlace continuous longitudinal (warp) filaments with horizontal filaments. The horizontal filaments can be either continuous; that is, a single filament that is repeatedly inserted across the width of the fabric or segments that

can be interlaced in Figure 6.11. The technology lends itself to mass production as well as development of small scale prototypes. The flexible ENHANS device is introduced as horizontal (weft) filament that is interlaced by the wrap filament to provide mechanical stability and structural integrity to the fabric. This enables the ENHANS device to protrude from the edge of the fabric and can be interconnected to complete the circuit. A subset of filaments maybe used to provide mechanical strength, form and packaging to the electrically active filament component. Furthermore, the fabric developed can be easily folded which is essential for portable energy applications in Figure 6.11d. The textile supporting structure allows the device to be gently compressed and folded while ensuring that contacts critical to the completeness of the circuit are not damaged. Due to its appealing features like high flexibility, light-weight and low-cost, the woven matrix is very attractive for various applications, including military clothing, roof tops of cars/buses/trains/houses, and drone wings.

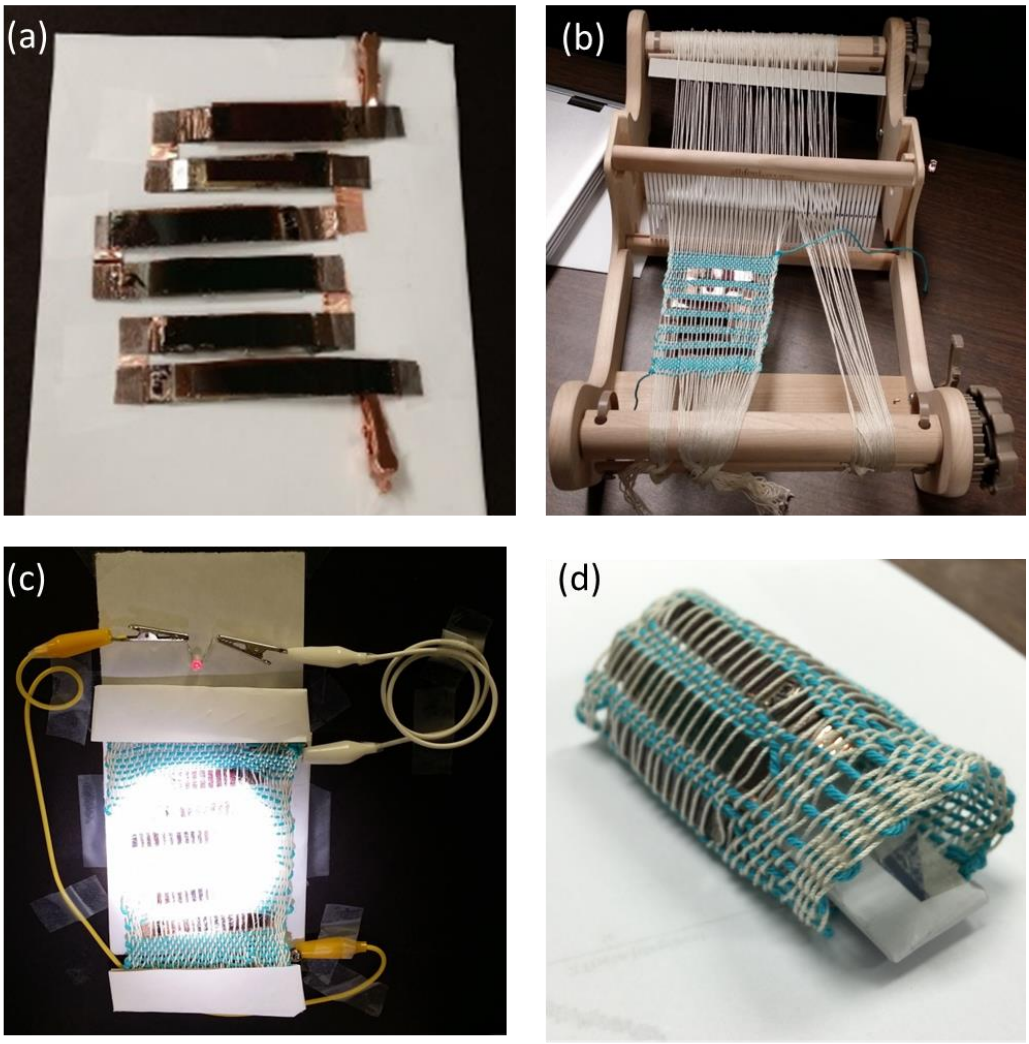

Figure 6.11 (a) Photographs represent six single combination devices in series, (b) loom weaving technique to prepare the bi-functional smart energy textile, (c) as-prepared smart textile is used to light up an LED during photo charging with a simulator and (d) the fabric developed can be easily folded which is essential for portable energy applications.

A simple plain woven structure was used to fabricate the prototype on a hobbyist hand loom. The loom supports standard textile weaving process as found in high production machines. The weft (horizontal filling) is inserted manually. The device is interspersed with spacer cotton filaments to provide separation between devices and the flexibility to bend the fabric. The interlacement of the cotton weft filing with the longitudinal cotton warp that is drawn through

the heddle provides the fabric structure with the mechanical stability needed to support the devices. The devices are inserted as a horizontal weft insert and protrude at each end. The protruding ends are used to interconnect the devices and ensure the continuity of charge flow between each segment (weft insert) of the device. The separately inserted devices are interconnected at the protruding ends. This process was done by hand, for the prototype, however a simple mechanism can be developed to automate the interconnections. The simplicity and scalability of the weaving process and the vast number of filament types that can be woven make this demonstration significant from a mass manufacture perspective.

6.7 Characterization of ENHANS

For the evaluation of the PSCs performance, a solar simulator with a 300 W Xenon lamp and AM 1.5G global filter were used. The light intensity, 100 $mWcm^2$ was calibrated using a silicon photovoltaic reference cell (Newport, 91150V). Current-voltage characteristics were measured with a Keithley 2635A source measurement unit. Devices were masked with a black metal aperture to define an active area of 0.075 cm^2. The EQE spectra were measured using a Newport model QE-PV-SI coupled with a lock-in amplifier and a calibrated silicon photodetector. Histogram of PCEs measured for 48 solar cells prepared by CB assisted growth technique is given in Figure 6.12. Surface morphologies were characterized by means of SEM (ZEISS Ultra 55) and transmission electron microscopy (TEM, TECNAI F30) equipped with an energy-dispersive X-ray spectroscopy (EDS). To investigate the chemical compositions of sample surface, X-ray photoelectron spectroscopy (XPS, PHI 5400) was performed. To compare the electrochemical performance of different materials, a three-electrode system consisting of a

working electrode (based on the materials prepared), a platinum counter electrode and a saturated calomel electrode (SCE) as reference electrode are used. Cyclic voltammetry (CV) and galvanostatic charge-discharge (GCD) measurements were performed using this three-electrode configuration in 1M KOH solution on an electrochemical workstation (Bio-Logic, SP-150). The characterization experiments of the devices using solid electrolyte were conducted by a two electrode system in air at a voltage range of 0–0.8 V. Electrochemical impedance spectroscopy (EIS) measurements were performed by applying an AC voltage with 5 mV amplitude in a frequency range from 10 mHz to 100 kHz. All calculations including specific capacitance as well as energy density and power densities are discussed.

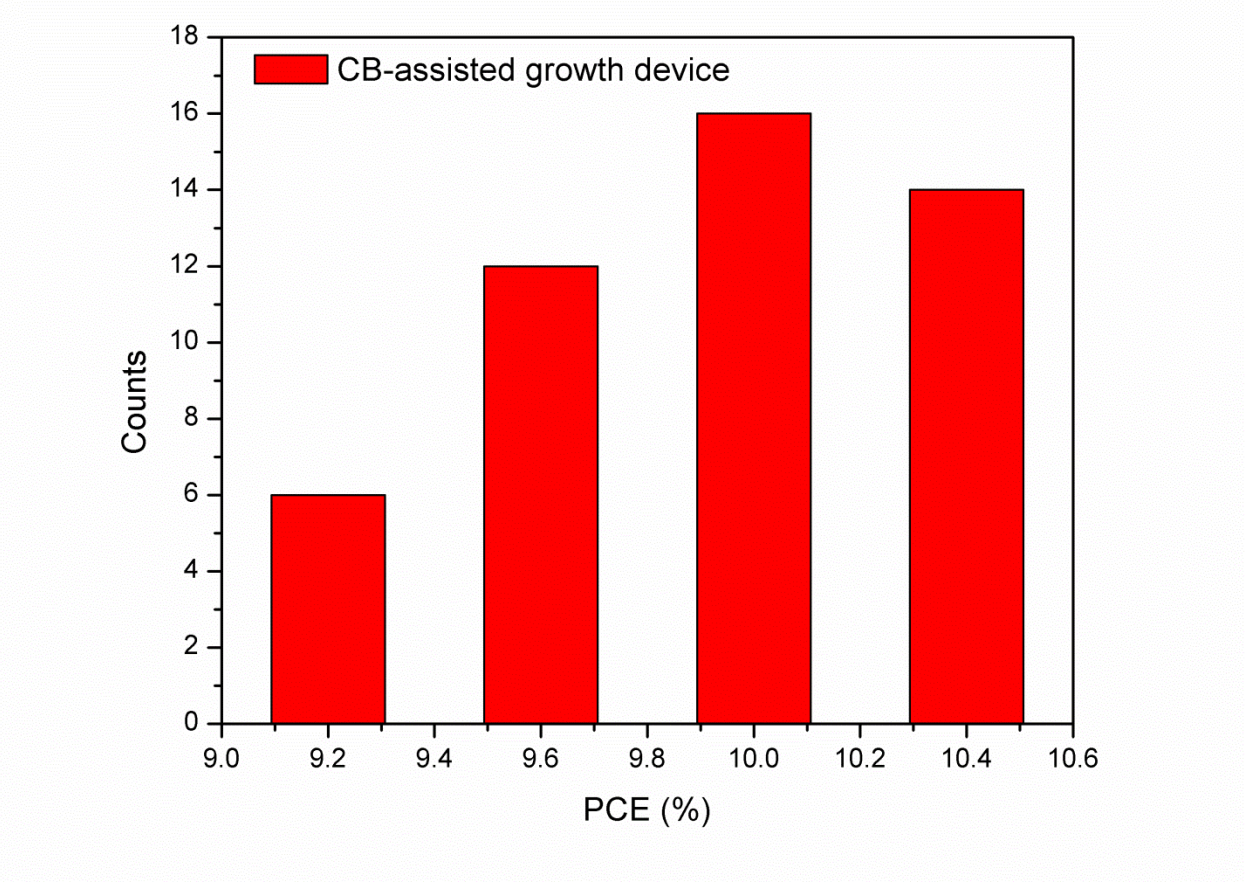

Figure 6.12 Histogram of PCEs measured for 48 solar cell devices prepared by CB assisted process. All the J-V curves were measured under 100 mW cm^{-2} simulated AM 1.5G sunlight by reverse voltage scan (scan rate: 0.05 V s^{-1}).

The electrochemical performacne of the devices have been calculated by using the following equations from the previously reported literatures:

Single electrode: Specific Capacitance (C_s) of the electrode is the capacitance per unit area of one electrode. The areal specific capacitance is calculated as: Equation 1

$$C_S = \frac{C_{electrode}}{A}$$

Where A (cm^2) is the total area of the electrode.

In CV measurements, $C_{electrode}$ is calculated from: Equation 2

$$\mathrm{C_{electrode}} = \frac{1}{(2 * \Delta V * v_0)} \int_a^b \left(\left|\mathrm{I_{Cu(OH)_2@AuPD@MnO_2}}\right|\right) dV$$

Where I is the current, V is the voltage, ΔV is the voltage window, v_0 is the scan rate, and a and b are voltage window boundries.

In GCD measurements, capacitance can be computed as shown: Equation 3

$$\mathrm{C_{electrode}} = \frac{\mathrm{I} * (\Delta \mathrm{t_{Cu(OH)_2@AuPD@MnO_2}})}{\Delta \mathrm{V}}$$

Where I is the discharge current, Δt is the discharge time, and ΔV is the voltage difference of discharge (obtained from the discharge curve excluding the voltage drop).

Symmetric supercapacitor device: Cell capacitance (C_{cell}) is calculated from the discharge curve of GCD measurement using the following equation: Equation 4

$$\mathrm{C_{cell}} = \frac{\mathrm{I} * \Delta \mathrm{t}}{\Delta \mathrm{V}}$$

Where I is the discharge current, Δt is the discharge time, and ΔV is the voltage difference of discharge (obtained from the discharge curve excluding the voltage drop).

Areal specific capacitance (C_{asc}) of the device can be calculated as: Equation S5

$$\mathrm{C_{asc}} = \frac{\mathrm{C_{cell}}}{\mathrm{A}}$$

Where A (cm^2) is the total area of the device.

Energy density and power density calculation: The energy density (E) and power density (P) can be calculated as follows:

$$E = \frac{1}{2 * 3600} * C_{asc} * \Delta V^2$$

$$P = \frac{E}{\Delta t}$$

Where C is the areal specific capacitance of the device, ΔV is the voltage difference of discharge and Δt is the discharge time.

6.8 Conclusion

In summary, we have developed a single ribbon which simultaneously harvests and stores energy. The energy generated on one side of the ribbon can be stored on the other side through a shared electrode. The perovskite solar cell developed provides a high energy conversion efficiency of more than 10% with high environmental stability. A simple wet processing technique is used to fabricate CuOHNT on the supercapacitor electrodes which considerably enhance the storage capability of the ENHANS filaments. High flexibility and all solid state device architecture of the ENHANS filaments provides the ability to weave them into a textile form which may find numerous applications including wearable electronics.

6.9 References

1. A. Dai, *Sci. Rep.*, 2016, **6**, 19110.
2. T. Wigley, *Nature*, 1991, **349**, 503-506.
3. J. H. Mercer, *Nature*, 1978, **271**, 321-325.

4. H. Rodhe, *Science*, 1990, **248**, 1217.

5. M. Hoel and S. Kverndokk, *Resour. Energy Econ.*, 1996, **18**, 115-136.

6. M. Asif and T. Muneer, *Renew. Sustainable Energy Rev.*, 2007, **11**, 1388-1413.

7. J. Tollefson, *Nature news*, 2008, **456**, 436-440.

8. B. Liu, J. Zhang, X. Wang, G. Chen, D. Chen, C. Zhou and G. Shen, *Nano Lett.*, 2012, **12**, 3005-3011.

9. X. Pu, L. Li, H. Song, C. Du, Z. Zhao, C. Jiang, G. Cao, W. Hu and Z. L. Wang, *Adv. Mater.*, 2015, **27**, 2472-2478.

10. T. Chen and L. Dai, *Energy Storage Mater.*, 2016, **2**, 21-26.

11. J. Xu, Y. Chen and L. Dai, *Nat. Commun.*, 2015, **6**.

12. K. Jost, D. P. Durkin, L. M. Haverhals, E. K. Brown, M. Langenstein, H. C. De Long, P. C. Trulove, Y. Gogotsi and G. Dion, *Adv. Energy Mater.*, 2015, **5**, 4.

13. K. Jost, C. R. Perez, J. K. McDonough, V. Presser, M. Heon, G. Dion and Y. Gogotsi, *Energy Environ. Sci.*, 2011, **4**, 5060-5067.

14. S. Pan, Z. Yang, P. Chen, J. Deng, H. Li and H. Peng, *Angew. Chem. Int. Ed.*, 2014, **53**, 6110-6114.

15. M. Xiao, F. Huang, W. Huang, Y. Dkhissi, Y. Zhu, J. Etheridge, A. Gray-Weale, U. Bach, Y. B. Cheng and L. Spiccia, *Angew. Chem.*, 2014, **126**, 10056-10061.

16. E. Akhavan-Rezai, M. Shaaban, E. El-Saadany and F. Karray, *Power & Energy Society General Meeting. IEEE*, 2015, **14**, 1-5.

17. R. A. Agathokleous and S. A. Kalogirou, *Renew. Energy*, 2016, **89**, 743-756.

18. K. Gurav, U. Patil, S. Shin, G. Agawane, M. Suryawanshi, S. Pawar, P. Patil, C. Lokhande and J. Kim, *J. Alloys Compd.*, 2013, **573**, 27-31.

19. S. Zhou, X. Feng, H. Shi, J. Chen, F. Zhang and W. Song, *Sensors Actuators B: Chem.*, 2013, **177**, 445-452.

20. V. V. Jadhav, D. V. Shinde, S. A. Patil, M. K. Zate, S. Pawar, A. Al-Osta, R. S. Mane, K. Hui, K. Hui and S.-H. Han, *Journal of Nanoeng. and Nanomanuf.*, 2014, **4**, 168-172.

21. P. Simon and Y. Gogotsi, *Nat. Mater.*, 2008, **7**, 845-854.

22. Z. Yu, L. Tetard, L. Zhai and J. Thomas, *Energy Environ. Sci.*, 2015, **8**, 702-730.

23. M. F. El-Kady, M. Ihns, M. Li, J. Y. Hwang, M. F. Mousavi, L. Chaney, A. T. Lech and R. B. Kaner, *Proc. Natl. Acad. Sci.*, 2015, **112**, 4233-4238.

24. J. Yan, E. Khoo, A. Sumboja and P. S. Lee, *ACS nano*, 2010, **4**, 4247-4255.

25. Z. Yu, B. Duong, D. Abbitt and J. Thomas, *Adv. Mater.*, 2013, **25**, 3302-3306.

26. X. Lu, T. Zhai, X. Zhang, Y. Shen, L. Yuan, B. Hu, L. Gong, J. Chen, Y. Gao and J. Zhou, *Adv. Mater.*, 2012, **24**, 938-944.

27. X. Lu, G. Wang, T. Zhai, M. Yu, S. Xie, Y. Ling, C. Liang, Y. Tong and Y. Li, *Nano Lett.*, 2012, **12**, 5376-5381.

28. L. Yuan, X.-H. Lu, X. Xiao, T. Zhai, J. Dai, F. Zhang, B. Hu, X. Wang, L. Gong and J. Chen, *ACS nano*, 2011, **6**, 656-661.

29. L. Bao, J. Zang and X. Li, *Nano Lett.*, 2011, **11**, 1215-1220.

30. Z. Yu and J. Thomas, *Adv. Mater.*, 2014, **26**, 4279-4285.

31. P. Yang, X. Xiao, Y. Li, Y. Ding, P. Qiang, X. Tan, W. Mai, Z. Lin, W. Wu and T. Li, *ACS nano*, 2013, **7**, 2617-2626.

32. Y. Huang, H. Hu, Y. Huang, M. Zhu, W. Meng, C. Liu, Z. Pei, C. Hao, Z. Wang and C. Zhi, *ACS nano*, 2015, **9**, 4766-4775.

33. X. Wang, B. D. Myers, J. Yan, G. Shekhawat, V. Dravid and P. S. Lee, *Nanoscale*, 2013, **5**, 4119-4122.

34. M. Huang, Y. Zhang, F. Li, L. Zhang, R. S. Ruoff, Z. Wen and Q. Liu, *Sci. Rep.*, 2014, **4**.

35. W. Li, K. Xu, B. Li, J. Sun, F. Jiang, Z. Yu, R. Zou, Z. Chen and J. Hu, *ChemElectroChem*, 2014, **1**, 1003-1008.

36. Z. Zhang, X. Chen, P. Chen, G. Guan, L. Qiu, H. Lin, Z. Yang, W. Bai, Y. Luo and H. Peng, *Adv. Mater.*, 2014, **26**, 466-470.

37. M. D. Stoller, S. Park, Y. Zhu, J. An and R. S. Ruoff, *Nano Lett.*, 2008, **8**, 3498-3502.

38. W. Nie, H. Tsai, R. Asadpour, J.-C. Blancon, A. J. Neukirch, G. Gupta, J. J. Crochet, M. Chhowalla, S. Tretiak and M. A. Alam, *Science*, 2015, **347**, 522-525.

39. C. Roldán-Carmona, O. Malinkiewicz, A. Soriano, G. M. Espallargas, A. Garcia, P. Reinecke, T. Kroyer, M. I. Dar, M. K. Nazeeruddin and H. J. Bolink, *Energy Environ. Sci.*, 2014, **7**, 994-997.

40. J. You, Z. Hong, Y. M. Yang, Q. Chen, M. Cai, T.-B. Song, C.-C. Chen, S. Lu, Y. Liu and H. Zhou, *ACS NANO*, 2014, **8**, 1674-1680.

41. T. Leijtens, G. E. Eperon, S. Pathak, A. Abate, M. M. Lee and H. J. Snaith, *Nat. Commun.*, 2013, **4**.

42. J.-H. Im, C.-R. Lee, J.-W. Lee, S.-W. Park and N.-G. Park, *Nanoscale*, 2011, **3**, 4088-4093.

43. M. Liu, M. B. Johnston and H. J. Snaith, *Nature*, 2013, **501**, 395-398.

44. X. Xiao, T. Li, P. Yang, Y. Gao, H. Jin, W. Ni, W. Zhan, X. Zhang, Y. Cao and J. Zhong, *Acs Nano*, 2012, **6**, 9200-9206.

45. Z. Yang, J. Deng, H. Sun, J. Ren, S. Pan and H. Peng, *Adv. Mater.*, 2014, **26**, 7038-7042.

46. Z. Yu, C. Li, D. Abbitt and J. Thomas, *J. Mater. Chem. A*, 2014, **2**, 10923-10929.

47. Z. Yu, J. Moore, J. Calderon, L. Zhai and J. Thomas, *Small*, 2015, **11**, 5289-5295.

48. C. Zhou, H. Wang, F. Peng, J. Liang, H. Yu and J. Yang, *Langmuir*, 2009, **25**, 7711-7717.

49. A. S. Arico, P. Bruce, B. Scrosati, J.-M. Tarascon and W. Van Schalkwijk, *Nat. Mater.*, 2005, **4**, 366-377.

50. G. Wang, L. Zhang and J. Zhang, *Chem. Soc. Rev.*, 2012, **41**, 797-828.

7 CONCLUSION

7.1 Summary

In this dissertation, different approaches to fabricate high performance organic and perovskite soalr cell are discussed. Chapter 1 and 2 provided an overview of the basic concepts and benefits of organic & perovskite solar cell.

In Chapter 3, I demonstrated an efficient method to produce well-ordered nanostructure with reusable template. The as-prepared nanostructured ZnO-AgNW-ZnO was employed as transparent electrode to build semitransparent organic solar cells. P3HT:PCBM organic solar cell based on these printed nanostructured electrodes showed considerable PCE enhancement (~17%) compared to those prepared based on non-nanostructured ones.

In Chapter 4, the influence of ternary solvents used in the preparation of active material (PTB7:ICBA) has been discussed. PTB7:ICBA organic solar cells fabricated by this ternary solvent method shows a significant PCE enhancement compared with binary solvent method. Two new nanoscale characterization techniques, PFM and MSAFM, have been introduced to exploit the properties of the mixed organic blend at the nanoscale.

In Chapter 5, PCBM-assisted growth method has been presented for allowing the penetration of PCBM into perovskite grain boundaries. This leads to develop hybrid perovskite-PCBM structure. Semitransparent perovskite solar cell fabricated by this structure shows a high PCE of 9.1% and a good AVT of 18%.

In Chapter 6, the ENHANS which simultaneously harvest and stores energy has been developed. The energy generated on one side of the ribbon can be stored on the other side through a shared electrode. The perovskite solar cell developed provides a high energy

conversion efficiency of more than 10% with high environmental stability. A simple wet processing technique is used to fabricate CuOHNT on the supercapacitor electrodes which considerably enhance the storage capability of the ENHANS filaments. High flexibility and all solid state device architecture of the ENHANS filaments provides the ability to weave them into a textile form which may find numerous applications including wearable electronics.

7.2 Future Directions

Nanostructured electrode and solvent engineering methods are very promising and feasible for obtaining the high performance organic and perovskite solar cells. Especially, solvent engineering attracts researcher attention for growing large size crystal grains for better performance. However, the stability is still a major issue for the commercialization of this new generation solar cells.

To solve this problem, carbon or other water resistant electrodes show much better stability for preventing the diffusion of humidity. To further improve the performance and stability, doping other materials like PMMA with perovskite or buffer layer may offer a new direction for perovskite solar cells research.

APPENDIX A:

COPYRIGHT PERMISSION LETTER FOR FIGURE 2.6a

Science AAAS

Title: Electron-Hole Diffusion Lengths Exceeding 1 Micrometer in an Organometal Trihalide Perovskite Absorber

Author: Samuel D. Stranks,Giles E. Eperon,Giulia Grancini,Christopher Menelaou,Marcelo J. P. Alcocer,Tomas Leijtens,Laura M. Herz,Annamaria Petrozza,Henry J. Snaith

Publication: Science

Publisher: The American Association for the Advancement of Science

Date: Oct 18, 2013

Order Completed

Thank you very much for your order.

This is a License Agreement between chao li ("You") and The American Association for the Advancement of Science ("The American Association for the Advancement of Science"). The license consists of your order details, the terms and conditions provided by The American Association for the Advancement of Science, and the payment terms and conditions.

Get the printable license.

License Number	3873330115860
License date	May 20, 2016
Licensed content publisher	The American Association for the Advancement of Science
Licensed content publication	Science
Licensed content title	Electron-Hole Diffusion Lengths Exceeding 1 Micrometer in an Organometal Trihalide Perovskite Absorber
Licensed content author	Samuel D. Stranks,Giles E. Eperon,Giulia Grancini,Christopher Menelaou,Marcelo J. P. Alcocer,Tomas Leijtens,Laura M. Herz,Annamaria Petrozza,Henry J. Snaith
Licensed content date	Oct 18, 2013
Volume number	342
Issue number	6156
Type of Use	Thesis / Dissertation
Requestor type	Scientist/individual at a research institution
Format	Electronic
Portion	Text Excerpt
Number of pages requested	1
Order reference number	None
Title of your thesis / dissertation	INTEGRATED SOLVENT ENGINEERING ENERGY HARVESTING DEVICES AND ENERGY STORAGE DEVICES
Expected completion date	Jun 2016
Estimated size(pages)	130
Total	0.00 USD

ORDER MORE... CLOSE WINDOW

APPENDIX B:

COPYRIGHT PERMISSION LETTER FOR FIGURE 2.6b

Science
AAAS

Title: Electron-Hole Diffusion Lengths Exceeding 1 Micrometer in an Organometal Trihalide Perovskite Absorber

Author: Samuel D. Stranks,Giles E. Eperon,Giulia Grancini,Christopher Menelaou,Marcelo J. P. Alcocer,Tomas Leijtens,Laura M. Herz,Annamaria Petrozza,Henry J. Snaith

Publication: Science

Publisher: The American Association for the Advancement of Science

Date: Oct 18, 2013

Order Completed

Thank you very much for your order.

This is a License Agreement between chao li ("You") and The American Association for the Advancement of Science ("The American Association for the Advancement of Science"). The license consists of your order details, the terms and conditions provided by The American Association for the Advancement of Science, and the payment terms and conditions.

Get the printable license.

License Number	3873330236091
License date	May 20, 2016
Licensed content publisher	The American Association for the Advancement of Science
Licensed content publication	Science
Licensed content title	Electron-Hole Diffusion Lengths Exceeding 1 Micrometer in an Organometal Trihalide Perovskite Absorber
Licensed content author	Samuel D. Stranks,Giles E. Eperon,Giulia Grancini,Christopher Menelaou,Marcelo J. P. Alcocer,Tomas Leijtens,Laura M. Herz,Annamaria Petrozza,Henry J. Snaith
Licensed content date	Oct 18, 2013
Volume number	342
Issue number	6156
Type of Use	Thesis / Dissertation
Requestor type	Scientist/individual at a research institution
Format	Electronic
Portion	Text Excerpt
Number of pages requested	1
Order reference number	None
Title of your thesis / dissertation	INTEGRATED SOLVENT ENGINEERING ENERGY HARVESTING DEVICES AND ENERGY STORAGE DEVICES
Expected completion date	Jun 2016
Estimated size(pages)	130
Total	0.00 USD

ORDER MORE... CLOSE WINDOW

APPENDIX C:

COPYRIGHT PERMISSION LETTER FOR FIGURE 2.7

APPENDIX D:
COPYRIGHT PERMISSION LETTERS FOR RELEVANT PUBLICATIONS UPON WHICH THIS DISSERTATION IS BASED ON IN PART

APPENDIX E:
LIST OF RELEVANT PUBLICATIONS

This dissertation is based in part on the following publications:

1. Chao Li, Joseph Sleppy, Nitesh Dhasmana, Mikhael Soliman, Laurene Tetard and Jayan Thomas, "A PCBM-assisted perovskite growth process to fabricate high efficiency semitransparent solar cells" *J. Mater. Chem. A* Accepted.
2. Chao Li, Md. Monirul Islam, Julian Moore, Joseph Sleppy, Caleb Morrison, Konstantin Konstantinov, Shi Xue Dou, Chait Renduchintala and Jayan Thomas, "Energy-smart weavable ribbons for simultaneous energy harvest and storage" *Nat. Energy* Submitted.
3. *Chao Li, Yi Ding, Mikhael Soliman, Josie Lorenzo, Nitesh Dhasmana, Panit Chantharasupawong, Anton V. Ievlev, Andre J. Gesquiere, Laurene Tetard, Jayan Thomas,* "Probing ternary solvent effect in high V_{oc} polymer solar cells using advanced AFM techniques" *ACS Appl. Mater. Interfaces* 2016, *8*, 4730–4738